Université de Montréal

Optimisation des paramètres de carbone de sol dans le modèle CLASSIC à l'aide d'optimisation bayésienne et d'observations

par

Charles Gauthier

Département de géographie
Faculté des arts et des sciences

Mémoire présenté en vue de l'obtention du grade de
Maître ès sciences (M.Sc.)
en Géographie

28 avril 2023

Université de Montréal

Faculté des arts et des sciences

Ce mémoire intitulé

Optimisation des paramètres de carbone de sol dans le modèle CLASSIC à l'aide d'optimisation bayésienne et d'observations

présenté par

Charles Gauthier

a été évalué par un jury composé des personnes suivantes :

Alexis Berg
(président-rapporteur)

Oliver Sonnentag
(directeur de recherche)

Joe Melton
(codirecteur)

Christian Seiler
(membre du jury)

Résumé

Le réservoir de carbone de sol est un élément clé du cycle global du carbone et donc du système climatique. Les sols et le carbone organique qu'ils contiennent constituent le plus grand réservoir de carbone des écosystèmes terrestres. Ce réservoir est également responsable du stockage d'une grande quantité de carbone prélevé de l'atmosphère par les plantes par la photosynthèse. C'est pourquoi les sols sont considérés comme une stratégie de mitigation viable pour réduire la concentration atmosphérique de CO_2 dûe aux émissions globales de CO_2 d'origine fossile. Malgré son importance, des incertitudes subsistent quant à la taille du réservoir global de carbone organique de sol et à ses dynamiques. Les modèles de biosphère terrestre sont des outils essentiels pour quantifier et étudier la dynamique du carbone organique de sol. Ces modèles simulent les processus biophysiques et biogéochimiques au sein des écosystèmes et peuvent également simuler le comportement futur du réservoir de carbone organique de sol en utilisant des forçages météorologiques appropriés. Cependant, de grandes incertitudes dans les projections faite par les modèles de biosphère terrestre sur les dynamiques du carbone organique de sol ont été observées, en partie dues au problème de l'équifinalité. Afin d'améliorer notre compréhension de la dynamique du carbone organique de sol, cette recherche visait à optimiser les paramètres du schéma de carbone de sol contenu dans le modèle de schéma canadien de surface terrestre incluant les cycles biogéochimiques (CLASSIC), afin de parvenir à une meilleure représentation de la dynamique du carbone organique de sol. Une analyse de sensibilité globale a été réalisée pour identifier lesquels parmis les 16 paramètres du schéma de carbone de sol, n'affectaient pas la simulation du carbone organique de sol et de la respiration du sol. L'analyse de sensibilité a utilisé trois sites de covariance des turbulences afin de représenter différentes conditions climatiques simulées par le schéma de carbone de sol et d'économiser le coût calculatoire de l'analyse. L'analyse de sensibilité a démontré que certains paramètres du schéma de carbone de sol ne contribuent pas à la variance des simulations du carbone organique de sol et de la respiration du sol. Ce résultat a permis de réduire la dimensionnalité du problème d'optimisation. Ensuite, quatre scénarios d'optimisation ont été élaborés sur la base de l'analyse de sensibilité, chacun utilisant un ensemble de paramètres. Deux fonctions coûts ont été utilisées pour l'optimisation de chacun des scénarios. L'optimisation a également démontré que la fonction coût utilisée avait un impact sur les ensembles de paramètres optimisés. Les ensembles de paramètres obtenus à partir des différents scénarios et fonctions coûts ont été comparés à des ensembles de données indépendants et à des estimations globales du carbone organique de sol à l'aide de métrique tel la racine de l'erreur quadratique moyenne et le bias, afin d'évaluer l'effet des ensembles de paramètres sur les simulations effectuées par le schéma de carbone de sol. Un ensemble de paramètres a surpassé les autres ensembles de paramètres optimisés ainsi que le paramétrage par défaut du modèle. Ce résultat a indiqué que la structure d'optimisation était en mesure de produire un ensemble de paramètres qui simulait des valeurs de carbone organique de sol et de respiration du sol qui étaient plus près des valeurs observées que le modèle CLASSIC par défaut, améliorant la représentation de la dynamique du carbone du sol. Cet ensemble de paramètres optimisés a ensuite été utilisé pour effectuer des simulations futures (2015-2100) de la dynamique du carbone organique de sol afin d'évaluer son impact sur les projections de CLASSIC. Les simulations futures ont montré que l'ensemble de paramètres optimisés simulait une quantité de carbone organique de sol 62 % plus élevée que l'ensemble de paramètres par défaut tout en simulant des flux de respiration du sol similaires. Les simulations futures ont également montré que les ensembles de paramètres optimisés et par défaut prévoyaient que le réservoir de carbone organique de sol demeurerait un puits de carbone net d'ici 2100 avec des sources nettes régionales. Cette étude a amélioré globalement la représentation de la dynamique du carbone organique de sol dans le schéma de carbone de sol de CLASSIC en fournissant un ensemble de paramètres optimisés. Cet ensemble de paramètres devrait permettre d'améliorer notre compréhension de la dynamique du carbone du sol.

Mots-Clés : Carbone de sol, modélisation des écosystèmes terrestres, optimisation bayésienne, analyse de sensibilité, respiration des sols, changement climatique

Abstract

The soil carbon pool is a vital component of the global carbon cycle and, therefore, the climate system. Soil organic carbon (SOC) is the largest carbon pool in terrestrial ecosystems. This pool stores a large quantity of carbon that plants have removed from the atmosphere through photosynthesis. Because of this, soils are considered a viable climate change mitigation strategy to lower the global atmospheric CO_2 concentration that is presently being driven higher by anthropogenic fossil CO_2 emissions. Despite its importance, there are still considerable uncertainties around the size of the global SOC pool and its response to changing climate. Terrestrial biosphere models (TBM) simulate the biogeochemical processes within ecosystems and are critical tools to quantify and study SOC dynamics. These models can also simulate the future behavior of SOC if carefully applied and given the proper meteorological forcings. However, TBM predictions of SOC dynamics have high uncertainties due in part to equifinality. To improve our understanding of SOC dynamics, this research optimized the parameters of the soil carbon scheme contained within the Canadian Land Surface Scheme Including Biogeochemical Cycles (CLASSIC), to better represent SOC dynamics. A global sensitivity analysis was performed to identify which of the 16 parameters of the soil carbon scheme did not affect simulated SOC stocks and soil respiration (R_{soil}). The sensitivity analysis used observations from three eddy covariance sites for computational efficiency and to encapsulate the climate represented by the global soil carbon scheme. The sensitivity analysis revealed that some parameters of the soil carbon scheme did not contribute to the variance of simulated SOC and R_{soil}. These parameters were excluded from the optimization which helped reduce the dimensionality of the optimization problem. Then, four optimization scenarios were created based on the sensitivity analysis, each using a different set of parameters to assess the impact the number of parameters included had on the optimization. Two different loss functions were used in the optimization to assess the impact of accounting for observational error. Comparing the optimal parameters between the optimizations performed using the different loss functions showed that the loss functions impacted the optimized parameter sets. To determine which optimized parameter set obtained by each loss function was most skillful, they were compared to independent data sets and global estimates of SOC, which were not used in the optimization using comparison metrics based on root-mean-square-deviation and bias. This study generated an optimal parameter set that outperformed the default parameterization of the model. This optimal parameter set was then applied in future simulations of SOC dynamics to assess its impact upon CLASSIC's future projections. These future simulations showed that the optimal parameter set simulated future global SOC content 62 % higher than the default parameter set while simulating similar R_{soil} fluxes. The future simulations also showed that both the optimized and default parameter sets projected that the SOC pool would be a net sink by 2100 with regional net sources, notably tropical regions.

Keywords : Soil organic carbon, terrestrial ecosystem modeling, Bayesian optimization, sensitivity analysis, soil respiration, climate change

Table des matières

Liste des tableaux

Liste des figures

Liste des sigles et des abréviations

CH_4	Méthane
CMIP6	Projet d'intercomparaison de modèles couplés, de l'anglais *Coupled Model Intercomparison Project*
CO_2	Dioxyde de carbone
ESM	Modèles du système terrestre, de l'anglais *Earth System Model*
GIEC	Groupe d'experts intergouvernemental sur l'évolution du climat
ppmv	parties par million en volume
RCP	Trajectoires représentatives de concentration, de l'anglais *Representative Concentration Pathway*
R_{hetr}	respiration hétérotrophe
R_{sol}	respiration des sols

TBM	Modèles de biosphère terrestre, de l'anglais *Terrestrial Biosphere Models*

Remerciements

J'aimerais tout d'abord mentionner que la majorité de ce projet de recherche a été complété lors de la pandémie mondiale de COVID-19, ce qui représentait pour moi un espace de travail à même ma chambre dans un demi-sous-sol du quartier Côte-des-Neiges.

Je tiens premièrement à remercier mes directeurs de recherche Oliver et Joe. Merci pour votre confiance et votre support tout au long de ce projet. Votre expertise m'a aidé à devenir un meilleur scientifique et j'en garde une expérience qui, j'en suis convaincu, me servira longuement. Je tiens également à vous remercier pour les opportunités que vous avez su m'offrir, de la campagne de terrain aux Territoires du Nord-Ouest, aux séjours de recherche et aux nombreuses conférences auxquelles j'ai pu assister. Grâce à vous, j'ai pu lors de ce projet de recherche ajouter plusieurs cordes à mon arc. Vous avez été d'excellents guides dans mon parcours et je n'aurais pas souhaité un autre duo pour m'épauler au cours des dernières années.

Je tiens à remercier PermafrostNet CRSNG pour le support financier de ce projet qui m'a permis de me concentrer sur ma recherche sans avoir à me trouver une autre source de revenu.

La réalisation de ce projet n'aurait également pas été possible sans le support de plusieurs collègues et ami.es. Je tiens donc à remercier les membres du laboratoire AtmosBios. Un merci particulier à Vincent, Nia et Katie pour vos conseils, votre temps et votre écoute, les études graduées sont une aventure qu'on ne surmonte pas seul. J'espère que nos parcours se recroiseront à l'avenir. Je tiens également à remercier les membres du groupe de recherche d'environnement et changement climatique Canada à Victoria qui m'ont aidé dans ce projet. Tout d'abord, un merci particulier à Gesa pour avoir accepté de générer tous les fichiers dont j'avais besoin et pour avoir répondu à toutes mes questions. J'ai été heureux de travailler avec une scientifique de ton calibre et j'espère que nous aurons l'occasion de retravailler ensemble. Merci également à Raj pour les discussions (sérieuses et autres) et pour les réponses à mes questions.

J'aimerais remercier Eugène et Jonathan de m'avoir maintes fois rappelé de contribuer à l'entropie de l'univers. Camille, je te remercie d'être l'amie que tu es, merci pour les nombreux appels en confinement qui m'ont permis de me sortir la tête de mon demi-sous-sol, merci d'être inconditionnelle dans ton support, je nous souhaite le meilleur pour la suite de nos vies académiques et plus encore. Merci à Charles, Ève, Joseph, David et Vincent d'avoir partagé la fin de cette aventure avec moi, ça a fait du bien de savoir que je n'étais pas seul dans mon bateau.

Merci à Charles Tisseyre pour votre travail de vulgarisation scientifique. Vous avez su susciter en moi un intérêt pour la science très tôt dans ma vie et vous êtes ma réponse éternelle à la question *avec quelle personnalité publique voudriez-vous prendre un café?* Si jamais vous lisez ces lignes, n'hésitez pas à me contacter, on s'arrangera quelque chose.

Eliane, merci de m'avoir mainte fois ramené sur terre. Une grande partie de ce travail te revient et j'aspire à avoir un jour ces qualités humaines qui font de toi la personne magnifique que tu es. Je te suis reconnaissant pour tout ce que tu as fait pour m'aider dans ce projet et dans la vie. Je suis fier de nous et des choses que nous sommes capables d'accomplir ensemble.

Enfin, à mes parents qui se demande comment ils ont réussi à m'inculquer un amour pour les sciences à leur insu; vous m'avez doté d'une curiosité, d'une rigueur et d'une écoute qui m'ont suivi tant dans mon parcours scolaire et universitaire que dans ma vie personnelle. J'avance dans ce monde en réalisant un peu plus chaque jour la chance que j'ai de vous avoir, merci.

> Many people seem to think it foolish, even superstitious, to believe that the world could still change for the better. And it is true that in winter it is sometimes so bitingly cold that one is tempted to say, 'What do I care if there is a summer; its warmth is no help to me now.' Yes, evil often seems to surpass good. But then, in spite of us, and without our permission, there comes at last an end to the bitter frosts. One morning the wind turns, and there is a thaw. And so I must still have hope.
>
> *Vincent Van Gogh*

Chapitre 1

Contexte et objectifs de recherche

Ce premier chapitre a pour but de servir d'introduction au projet de recherche. Il s'attarde d'abord au cycle du carbone global pour ensuite dresser un portrait qu'y occupe le carbone contenu dans les sols. Ensuite, les dynamiques du carbone de sol et plus précisément l'impact que pourraient avoir ces dynamiques sur le cycle global dans un contexte de changements climatiques est abordé. Par la suite, une revue de littérature est effectuée sur les différents efforts de recherche ayant été faits sur la prédiction des dynamiques du carbone de sol fait par les modèles de biosphère terrestre, ainsi que sur les lacunes dans les connaissances scientifiques de ces modèles entravant la compréhension de ces dynamiques. À partir de ces lacunes se dresse la problématique du projet de recherche présenté dans ce mémoire.

1.1. Le cycle du carbone

Le cycle du carbone global est un cycle biogéochimique qui représente l'échange de carbone entre différents réservoirs. Les principaux réservoirs qui constituent le cycle du carbone sont le réservoir océanique, le réservoir atmosphérique et le réservoir terrestre qui comprend le carbone contenu dans la végétation, la faune et les sols (Fig. 1.1). Le réservoir terrestre inclut également le carbone organique dissout présent dans les réservoir d'eau douce. Le carbone circule d'un réservoir de carbone à un autre par des flux qui changent la taille des réservoirs. Cette dynamique du carbone à l'échelle planétaire est présente depuis des millions d'années et se divise en deux parties; le cycle du carbone lent et le cycle du carbone rapide. Le cycle du carbone lent opère sur une échelle temporelle de l'ordre de millions d'années (Berner, 2003). Le carbone du cycle du carbone lent concerne généralement le carbone inorganique contenu dans les roches, mais également les dépôts de carbone organique ayant formé les carburants fossiles. Le cycle du carbone rapide concerne les interactions entre les écosystèmes, l'atmosphère et les océans. Il agit sur des échelles de temps beaucoup plus courtes, de l'ordre de quelques heures à quelques milliers d'années. Le cycle du carbone global subit des perturbations majeures depuis l'anthropocène (Raupach and Canadell, 2010; Crutzen, 2016; Steffen et al., 2018). L'anthropocène est considérée comme la période depuis laquelle l'activité humaine entraîne des changements dans le système climatique (Waters et al., 2016), elle est définie comme débutant à la fin du 18^{e} siècle et se poursuit jusqu'à aujourd'hui (Crutzen, 2016). L'utilisation d'énergies fossiles depuis la révolution industrielle a comme conséquence de transférer du carbone appartenant au cycle lent vers le réservoir atmosphérique du cycle rapide. La concentration de carbone dans l'atmosphère sous forme de CO_2 est ainsi passée de près de 277 ppmv en 1750 à une concentration de 412 ppmv en 2020 (Friedlingstein et al., 2022), la plus haute concentration des derniers deux millions d'années (Canadell et al., 2021). Comme le cycle du carbone est intimement lié au système climatique global, cet ajout de carbone au réservoir atmosphérique affecte les dynamiques des réservoirs terrestres et du réservoir océanique. Tout d'abord, comme le CO_2 est un gaz à effet de serre, l'augmentation de sa concentration dans l'atmosphère contribue au réchauffement planétaire. Il est estimé que l'augmentation de la concentration en carbone de l'atmosphère CO_2 anthropologique et les autres gaz à effet de serre émis depuis la révolution industrielle auraient causé jusqu'à présent une augmentation globale de la température de surface terrestre moyenne de 1.59 °C depuis 1850 (Gulev et al., 2021). L'augmentation de la température a également comme effet d'augmenter la concentration atmosphérique en vapeur d'eau, un autre gaz à effet de serre (Held and Soden, 2000).

De l'excès de carbone qui est ajouté dans l'atmosphère, une partie est absorbée par les réservoirs terrestres et le réservoir océanique (Sellers et al., 2018). Par exemple, le réservoir océanique absorbe annuellement environ 2.8 Pg C du réservoir atmosphérique, soit plus d'un quart des 10.6 Pg C émis par l'humain par l'utilisation d'énergies fossiles et le changement d'affectation des terres (Fig. 1.1, Friedlingstein et al. (2022)). Le réchauffement des océans, une conséquence du réchauffement climatique pourrait également réduire la productivité du phytoplancton, des micro-organismes responsables de la photosynthèse dans les océans, ce qui pourrait réduire la capacité du réservoir océanique à retirer du carbone de l'atmosphère (Behrenfeld et al., 2006).

Les écosystèmes terrestres subissent également des changements causés par l'ajout de carbone anthropogénique et par le changement de couverture du sol et d'utilisation des sols (Canadell et al., 2021). La couverture du sol désigne la surface sur le sol, par exemple, la végétation, les infrastructures ou encore l'eau. L'utilisation des sols, elle, désigne l'usage qu'est fait du sol, par exemple l'habitat de la faune ou encore l'agriculture. Le changement de couverture du sol décrit donc le processus par lequel l'activité humaine transforme les

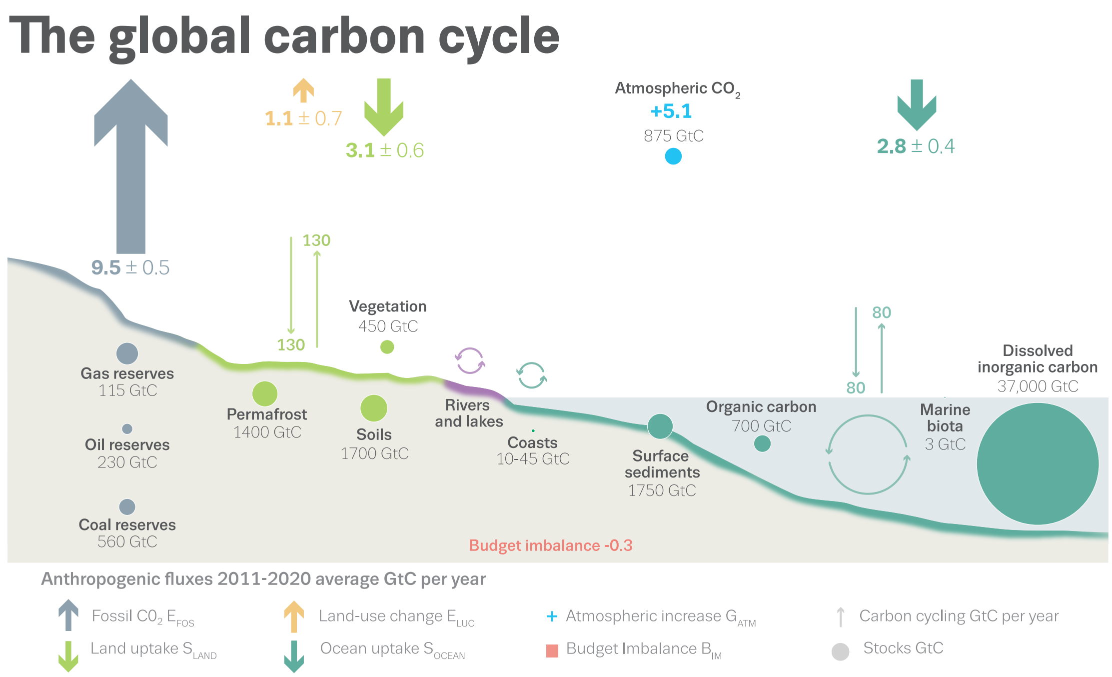

Fig. 1.1. Schéma des différentes composantes du cycle du carbone global. Les cerclent et le nombre qui leur est associé représente les différents réservoirs du cycle du carbone global. Les flèches sur la figure indiquent les flux entre les réservoirs de carbone. Le réservoir terrestre et ses flux correspondant sont indiqués en vert, le réservoir atmosphérique est indiqué en bleu et le réservoir océanique est indiqué en turquoise. Les perturbations anthropologiques apportées au cycle global du carbone par l'utilisation d'énergies fossiles (en gris) et par le changement de couverture du sol et d'utilisation du sol (en jaune) sont indiquées. Toutes les quantités sont en GtC, où 1 GtC = 1 Pg C. L'imbalance du budget (B_{IM}), indiqué en rouge au bas de la figure, correspond à la différence entre les émissions totales estimées et la quantité totale de carbone estimée contenue dans tous les réservoirs du cycle du carbone global. B_{IM} est une mesure de l'incertitude sur les données utilisées et sur la compréhension du cycle du carbone global. Figure tirée de Friedlingstein et al. (2022)

paysages naturels. Il décrit également le changement de l'utilité du territoire et prend en compte l'impact environnemental de ce changement. À cause des changements climatiques, les écosystèmes terrestres subissent l'effet fertilisant du CO_2. Cet effet survient lorsque l'augmentation de la concentration en CO_2 atmosphérique, combinée à un apport suffisant en eau et nutriments, augmente la productivité des plantes qui, par la photosynthèse, retire plus de CO_2 de l'atmosphère pour le stocker dans les organismes et dans le sol (Gulev et al., 2021). Bien que les plantes retirent du carbone de l'atmosphère, plusieurs perturbations viennent limiter leur capacité à séquestrer du carbone provenant de l'atmosphère dans les sols. En effet, le changement de couverture du sol vient changer la dynamique du réservoir des écosystèmes terrestres. Par exemple, la conversion de forêts capables de séquestrer une grande quantité de carbone en terres agricoles n'ayant pas la même capacité entraîne le relâchement additionnel de carbone par la coupe des arbres et diminue la capacité de l'écosystème à retirer du carbone de l'atmosphère (Guo and Gifford, 2002; Bonan, 2008). Il est estimé que le changement de couverture du sol sera responsable de l'émission de 350 Pg C additionnelle d'ici 2100 (Mahowald et al., 2017), soit environ 40 % de la quantité actuelle de carbone contenue dans l'atmosphère.

1.2. Le carbone de sol

Les sols sont un des réservoirs clés du cycle global du carbone. Ils contiennent plus de deux fois la quantité de carbone contenue dans l'atmosphère (Fig. 1.1, Canadell et al. (2021)). La dynamique du carbone dans les sols est régie par plusieurs processus biogéochimiques. Le carbone organique contenu dans les sols provient du carbone séquestré par les plantes par le processus de la photosynthèse. Les plantes capturent du carbone atmosphérique sous forme de CO_2 et l'entreposent sous forme de biomasse. Le carbone contenu dans la biomasse entre ensuite dans les sols par la litière (branche, feuilles, racines, etc.). Le sol relâche également du carbone vers l'atmosphère par l'effet combiné de la respiration autotrophe et de la R_{hetr}. La respiration autotrophe provient des feuilles et tiges des plantes à la surface et de leur racine sous la surface (Tang et al., 2020). La respiration hétérotrophe survient lorsque la matière organique contenue dans les sols est décomposée par les micro-organismes qui relâchent ensuite du carbone sous forme gazeuse. Il en résulte un flux de carbone vers l'atmosphère (Kutsch et al., 2009). Plusieurs facteurs environnementaux influencent la R_{hetr}. Elle est tout d'abord influencée par le type d'écosystème. La profondeur des racines, le type de biomasse qui entre dans les sols et la vitesse à laquelle celle-ci se décompose sont des facteurs des écosystèmes qui influencent la R_{hetr}. À titre d'exemple, la diversité des écosystèmes fait en sorte que la quantité de carbone reçue par les sols peut varier de 0.2 g C m^{-2} par année dans des déserts polaires à 12 g C m^{-2} par année pour une forêt de conifères, bien que la quantité moyenne globale soit de 2.4 g C m^{-2} par année (Fry et al., 2018). L'humidité des sols influence également la R_{hetr}. Elle peut fournir de meilleures conditions aux micro-organismes pour décomposer la matière organique. Par contre, un sol trop humide peut nuir à la R_{hetr}. C'est le cas par exemple des milieu humides, où l'humidité des sol est telle qu'il y a peu de R_{hetr} et donc une plus grande accumulation de matière organique dans les sols. Ainsi, il existe un taux d'humidité des sols qui est optimial à la R_{hetr}. Une augmentation entrainé par les changements climatiques de la précipitation et donc de l'humidité des sols augmente la productivité des plantes qui à leur tour font entrer plus de carbone dans les sols (Lajtha et al., 2018). La respiration hétérotrophe augmente également avec la température. Cette corrélation est particulièrement importante dans un contexte de changement climatique puisqu'elle implique que le flux de carbone provenant des sols vers l'atmosphère pourrait augmenter avec l'augmentation des températures (García-Palacios et al. (2021), Fig. 1.2). Ces relations entre la R_{hetr}, la température et l'humidité des sols trouvent leurs racines dans les interactions entre la matière organique du sol et les micro-organismes responsables de la décomposition de cette matière. Ces interactions sont diverses et bien souvent complexes. À cause de cette complexité et aux lacunes dans nos connaissances des interactions entre les communautés microbiennes et la matière organique des sols, des représentations simplifiées sont souvent implémentées dans les modèles climatiques afin de les prendre en compte.

De plus, les sols retirent annuellement 3.5 Pg de carbone de l'atmosphère (Keenan and Williams, 2018). Ils ont donc un rôle crucial dans la mitigation des changements climatiques (García-Palacios et al., 2021; Amelung et al., 2020; Bossio et al., 2020). Cependant, les perturbations du cycle global du carbone entraînent des changements dans la taille et les dynamiques du réservoir de carbone des sols. Il est estimé que les sols pourraient subir une réduction de 6 % de leur contenu en carbone organique sous le présent réchauffement planétaire de 1°C (Wang et al. (2022), Fig. 1.2). En plus de la réduction de la taille du réservoir, la réduction de la capacité du réservoir à absorber du carbone provenant de l'atmosphère a diminué. Il a été observé que l'effet fertilisant du CO_2 global est passé d'une absorption 21 % par 100 ppm de CO_2 atmosphérique à 12 % de 1982 à 2015 (Wang et al., 2020), indiquant que les écosystèmes semblent absorber moins de CO_2 atmosphérique lorsque sa concentration augmente. Il est prévu que la diminution de la capacité des sols à absorber du carbone provenant de l'atmosphère se poursuivra avec l'augmentation de la concentration en CO_2 atmosphérique (Canadell et al., 2021). L'effet combiné de la réduction de la taille du réservoir et de sa capacité à séquestrer du carbone pourrait mener à ce que les sols deviennent une source de carbone. Ce changement pourrait être accéléré en partie par le dégel du pergélisol (Schuur et al., 2022).

Le pergélisol est un sol qui est demeuré sous une température de 0°C pendant plus de deux années consécutives (Van Everdingen et al., 1998). Il couvre environ 25 % de la surface terrestre de l'hémisphère nord (Gruber, 2012). Il est estimé que le pergélisol contient jusqu'à 1600 Pg C (Schuur et al., 2018). Au sommet du pergélisol, près de la surface se trouve la couche active; la couche de sol qui subit un dégel saisonnier. Alors que le carbone contenu dans la couche active du pergélisol fait partie du cycle du carbone global, celui contenu dans le pergélisol est gelé, ce qui le rend inaccessible aux micro-organismes responsables de la décomposition. Comme les hautes latitudes se réchauffent à un rythme près de quatre fois plus rapide que la moyenne globale (Rantanen et al., 2022), une quantité grandissante de pergélisol dégèle et la profondeur de la couche active augmente. Lors de ce dégel, le carbone auparavant inaccessible aux micro-organismes devient disponible pour la décomposition, entraînant un flux de CO_2 vers l'atmosphère lors de la décomposition

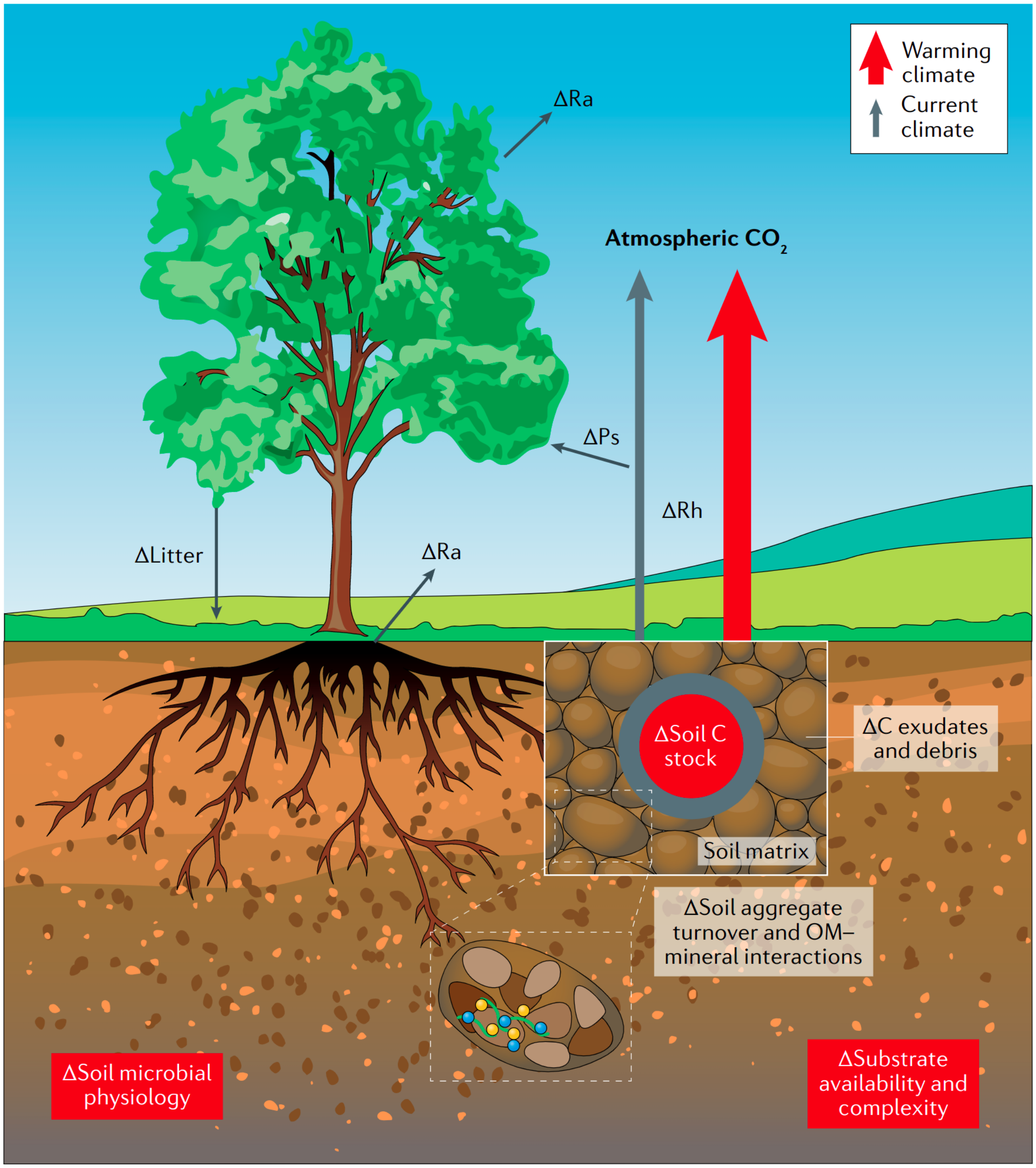

Fig. 1.2. Schématisation du changement de la dynamique de la respiration hétérotrophe dans un contexte de réchauffement climatique. Figure tirée de García-Palacios et al. (2021)

oxique et de CH_4 lors de la décomposition anoxique. Cette émission de CO_2 et de CH_4 par le dégèle du pergélisol contribue à l'augmentation des températures globales qui à son tour accélère le dégel du pergélisol, déclenchant ainsi une boucle de rétroaction positive. La boucle de rétroaction positive du pergélisol pourrait à elle seule relâcher plus de 200 Pg C supplémentaires dans l'atmosphère d'ici 2100 (Schuur et al., 2022). Les mécanismes qui influencent les dynamiques du carbone de sol se produisent généralement à l'échelle locale, rendant difficile leur généralisation à l'échelle globale. Or, comprendre les dynamiques du carbone de sol à l'échelle globale est crucial afin de comprendre comment les sols se comporteront dans un contexte de changement climatique.

1.3. Modèles de biosphère terrestre

Les prédictions quant aux changements des dynamiques de carbone de sol peuvent être simulées par des TBMs. Ces modèles sont des modèles numériques qui calculent les flux d'énergie et de matière émis de la surface terrestre vers l'atmosphère et peuvent parfois considérer les forçages anthropologiques. Les TBMs sont capables de simuler plusieurs variables clés du système terrestre. Ils peuvent par exemple simuler l'albédo de la surface, le flux d'énergie radiative provenant des sols et les dynamiques de la canopée des écosystèmes (Bonan et al., 2019). Ils peuvent également simuler la taille et la dynamique des réservoirs de carbone de sol. Lorsque certains TBMs sont couplés à des ESMs, les variables qu'ils simulent permettent de faire des prédictions sur l'évolution du système climatique. Par exemple, les TBMs couplés aux ESMs du regroupement CMIP6 (Eyring et al., 2016) sont utilisés pour simuler les dynamiques du cycle du carbone global sous les différents RCP établis par le GIEC.

Certains TBMs ont été originalement développés en tant que composante terrestre des ESMs (Flato, 2011; Fisher and Koven, 2020; Blyth et al., 2021). Au cours d'années de développement, plusieurs processus ayant un impact sur les dynamiques des systèmes simulés par les TBMs ont été ajoutés aux modèles. Ainsi, les modèles ont évolué de leur conception originale, simulant seulement les flux entre la surface et l'atmosphère (Sellers et al., 1986), à leur version actuelle qui prend en considération l'humidité des sols, les processus hydrologiques de surface, le cycle de l'azote et son couplage avec le cycle du carbone, le changement de couverture du sol, les perturbations des écosystèmes et plusieurs autres processus (p. ex. Lawrence et al. (2019)). En plus de l'ajout de processus, la résolution des TBMs et des ESMs auxquels ils sont parfois couplés s'améliore grâce à l'augmentation de la capacité de calcul et à de nouvelles bases de données (Fisher and Koven, 2020). L'amélioration des TBMs par l'ajout de processus et par l'amélioration de la résolution apporte également des défis à surmonter.

La complexification des modèles entraîne l'augmentation du nombre de paramètres requis pour représenter les processus simulés (Fisher and Koven, 2020). Une paramétrisation idéale est un ensemble de paramètres qui, lorsqu'utilisé par le modèle, génère des simulations en accord avec les observations. Or, paramétrer les modèles s'avère difficile à cause du caractère hétérogène des mécanismes de la biosphère terrestre (Blyth et al., 2021). En effet, lorsque les TBMs effectuent des simulations, ils le font généralement sur une grille couvrant la surface terrestre (Bonan et al., 2019). Les modèles simulent chacune des cellules de cette grille individuellement. Bien que la résolution des TBMs ait augmenté, la taille de ces cellules est généralement de l'ordre de 1x1 degrés, soit environ 100 km x 100 km dans le cas des latitudes moyennes (Bonan et al., 2019). Les simulations se font de sorte que les interactions entre l'atmosphère et la surface terrestres sont considérées comme homogènes à l'échelle de la cellule. Or, les processus biogéochimiques simulés par les modèles opèrent généralement sur des échelles plus petites. Ainsi, il est difficile de trouver la paramétrisation qui permet de correctement simuler le comportement moyen de ces mécanismes, ce qui entraîne des incertitudes dans les simulations. La paramétrisation est donc en partie responsable des incertitudes dans les TBMs (Shi et al., 2018). Afin d'améliorer la paramétrisation des TBMs, des routines d'optimisation des paramètres sont implantées. L'optimisation consiste à comparer les simulations d'un modèle à des observations de terrain et à changer les paramètres du modèle jusqu'à ce qu'il y ait un accord avec les simulations et les observations. Bien que la procédure soit répandue, elle se heurte au problème d'équifinalité. L'équifinalité survient lorsque plusieurs valeurs de paramètres mènent à une simulation en accord avec les observations (Tang and Zhuang, 2008). Il est ensuite difficile d'identifier quel ensemble de paramètres représente fidèlement le mécanisme qui est simulé. Pour surmonter le problème de l'équifinalité, les paramètres peuvent être optimisés à l'aide de plusieurs types de données, ce qui permet de mieux contraindre les paramètres (MacBean et al., 2016).

1.4. Objectif de la recherche

Le réservoir de carbone de sol est un élément crucial du cycle du carbone global. Afin de comprendre comment le réservoir répondra aux changements à venir, des modèles de biosphère terrestre sont utilisés pour simuler ses dynamiques. Cependant, des lacunes dans les modèles entravent la précision de ces projections. La structure des modèles, ainsi que leur paramétrisation a été identifiée comme étant en cause. Dans l'amélioration de leur paramétrisation, les modèles font face au problème d'équifinalité.

Ce projet de recherche a pour but d'optimiser les paramètres du schéma de carbone de sol contenu dans le modèle de biosphère terrestre CLASSIC et d'améliorer sa représentation des dynamiques du carbone de sol. Pour parvenir à ces buts, deux types de données d'observations ont été utilisées pour contraindre les paramètres du modèle et surmonter le problème de l'équifinalité. De plus, une analyse de sensibilité a été effectuée afin de réduire la dimensionnalité du problème d'optimisation. L'article scientifique du chapitre 2 rapporte les résultats ayant été obtenus lors de la réalisation de ces objectifs. Cet article est en préparation pour être soumis au *Journal of Advances in Modeling Earth Systems*. Il présente les résultats obtenus à la suite de l'optimisation des paramètres de dynamique du carbone de sol de CLASSIC. Combinées, l'utilisation de l'analyse de sensibilité et de multiples types de données d'observation ont permis d'optimiser les paramètres du schéma de carbone de sol de CLASSIC et d'obtenir un ensemble de paramètres simulant des dynamique du carbone de sol plus près des observations que la paramétrisation par défaut du modèle CLASSIC.

Chapitre 2

Attempting to Address Equifinality in Soil Organic Carbon Simulations with a Terrestrial Biosphere Model

2.1. Avant-propos

L'article présenté dans ce chapitre est en préparation afin d'être soumis au *Journal of Advances in Modeling Earth Systems*. Il présente les résultats de l'analyse de sensibilité des paramètres du schéma de carbone de sol du modèle CLASSIC ainsi que leur optimisation. L'article contient également des discussions concernant l'équifinalité dans les modèles de biosphère terrestre. Quatre autres personnes ont contribué à l'élaboration de cet article, chacune à des degrés différents.

J'ai élaboré les objectifs de recherche ainsi que l'étude sous la supervision d'Oliver Sonnentag et de Joe Melton. J'ai créé la structure d'optimisation bayésienne utilisée dans l'étude et j'ai écrit tous les scripts informatiques du schéma de carbone de sol utilisés pour produire les résultats présentés dans cet article. Gesa Meyer a produit les fichiers de données nécessaires pour que le schéma de carbone de sol puisse effectuer les simulations et a fait les simulations historiques et futures du modèle CLASSIC complet qui utilisaient les paramètres optimisés obtenus par la structure d'optimisation bayésienne. Raj Deepak Suruli Nagarajan a contribué à l'élaboration de l'analyse de sensibilité en apportant des conseils et des réflexions. J'ai élaboré les analyses à l'aide des conseils de Joe Melton et d'Oliver Sonnentag. Tous les tableaux et les figures contenus dans l'article ont été produits par moi-même. J'ai écrit l'article sous la supervision d'Oliver Sonnentag et de Joe Melton.

2.2. Résumé

Les modèles de biosphère terrestre, tel le modèle de schéma canadien de surface terrestre incluant les cycles biogéochimiques (CLASSIC), peinent à simuler des stocks de carbone organique du sol (SOC) et des flux de respiration du sol (R_{sol}) similaires aux valeurs observées. Cette lacune des modèles est due en partie au manque de contraintes sur les paramètres et à l'équifinalité. Dans le cadre de cette recherche, nous avons essayé de surmonter ces deux défis et de contraindre les 16 paramètres du schéma de carbone du sol de CLASSIC. Tout d'abord, nous avons utilisé une analyse de sensibilité globale (Sobol') afin de développer 4 scénarios d'optimisation, chacun généré à l'aide de différents critères de sensibilité des paramètres. Ensuite, nous avons optimisé les paramètres de chaque scénario en utilisant deux fonctions coûts; une tentant exclusivement de reproduire la valeur moyenne des observations (MO) et l'autre prenant explicitement en compte les erreurs sur les observations (EO). Chaque fonction coût évaluait la performmance du schéma de carbone de sol à l'aide de 436 353 observations de SOC provenant du Word Soil Information Service (WoSIS) et 1172 estimations de la R_{sol} annuelle provenant de la Soil respiration Database (SRDB). Les paramètres optimisés générés par les fonction coût présentaient une différence relative moyenne de 41 %. Cette différence entre les paramètres générés par les fonctions coût a indiqué qu'elles ont un impact sur les valeurs optimales des paramètres. Enfin, nous avons sélectionné l'ensemble de paramètres optimal donné par la combinaison du meilleur scénario d'optimisation (8 paramètres) et de la meilleure fonction coût (MO) en comparant chaque ensembles de paramètres à des bases de données de SOC et R_{sol} de hautes latitude (>60°N), basées sur des observation. Nous avons également comparé les ensembles de paramètre à des estimés de la quantité de SOC global tirés de la littérature. Nous avons trouvé une sous-estimation constante des stocks de SOC de hautes latitudes tant pour les ensembles de paramètres optimisés que pour l'ensemble par défaut. Cette sous-estimation indique que les intrants du schéma de carbone de sol provenant des autres composantes de CLASSIC (p. ex. humidité ou température des sols, influx de carbone dans les sols) peuvent compenser l'influence du paramétrage du schéma de carbone de sol. L'ensemble de paramètres optimal a obtenu un meilleur score d'optimisation en comparaison aux bases de données WoSIS et SRDB, avait des totaux de SOC globaux plus près des estimations tirées de la littérature et avait un biais moindre lorsque comparé aux base de données de hautes latitudes que l'ensemble de paramètres par défaut (biais relatif de -0.3990 et -0.10 lorsque comparé au bases de données de SOC et R_{sol} respectivement, comparativement à -0.3991 et -0.23 pour les paramètres par défaut). Donc, notre structure d'optimisation s'est avérée capable de générer un ensemble de paramètres qui a amélioré la représentation des changements temporels et spatiaux du SOC dans le modèle CLASSIC.

2.3. Abstract

Terrestrial biosphere models such as the Canadian Land Surface Scheme Including biogeochemical Cycles (CLASSIC) struggle to reproduce observed soil organic carbon (SOC) stocks and respiration fluxes due, in part, to poorly constrained parameters and parameter equifinality. Here we use a Bayesian optimization approach to address these two challenges and constrain the 16 parameters of the soil carbon scheme of CLASSIC. First, we employed a global sensitivity analysis (Sobol') to develop four optimization scenarios, each generated with different thresholds of parameter sensitivity. Next, we optimized the parameters of each scenario using two different loss functions; one focused on reproducing the observational mean value (MO), and the other explicitly accounting for the observational uncertainty (EO). Each loss function evaluated the soil carbon scheme's performance against 436,353 coring-based estimates of SOC stock from the World Soil Information Service (WoSIS) and 1172 chamber-based estimates of annual total soil respiration (R_{soil}) from the Soil Respiration Database (SRDB). After the optimizations, the optimized parameters had an average relative difference of 41 % between optimizations using the two loss functions indicating that the choice of loss function impacts what parameter values are found to be optimal. We selected the best scenario (8 parameters) and loss function (MO) by comparing each simulation's loss scores and their performance against observation-based estimates of high-latitude (>60°N) SOC and R_{soil} and literature estimates of global SOC totals that were not used during the optimization. We found a consistent underestimation of high-latitude SOC stocks in our simulations using both the default and optimized parameter sets. The underestimation indicates that the inputs to the soil carbon scheme, calculated by other components of CLASSIC (e.g., soil moisture or temperature, detrital inputs) can compensate the influence of the soil carbon scheme's parameter values. The optimal parameter set obtained a better score against WoSIS and SRDB, had global SOC totals in line with literature estimates, and a smaller bias against high-latitude SOC and R_{soil} data sets than the model default value (relative bias of -0.3990 and -0.10 for the optimal parameter set for SOC and R_{soil} respectively against -0.3991 and -0.23 for the default parameter set). Therefore, our optimization framework produced a parameter set that improved CLASSIC's representation of the temporal and spatial changes in SOC stocks.

2.4. Introduction

Human activities and their associated emissions of potent greenhouse gases such as carbon dioxide (CO_2) have been driving the rapid increase in atmospheric CO_2 concentration since the start of the industrial era. The increased CO_2 concentration resulted in unprecedented climate warming, altered precipitation patterns and intensifying disturbance regimes (Gulev et al., 2021; Friedlingstein et al., 2022; Padrón et al., 2020). The soils of terrestrial ecosystems contain the most organic carbon; a meta-analysis of global soil organic carbon (SOC) estimates identified a median value of about 1460 Pg of global SOC (Scharlemann et al., 2014), more than three times the approximately 450 Pg C currently contained in aboveground biomass (Canadell et al., 2021). Protecting or restoring soils' capacity to store carbone has been identified as a potential global-scale climate change mitigation strategy (Bossio et al., 2020; Amelung et al., 2020). However, this mitigation strategy is potentially at risk due to elevated soil temperatures that are increasing soil respiration (R_{soil}) (García-Palacios et al., 2021). Considering the size of the SOC pool, increased respiratory CO_2 losses could cause the global SOC pool, currently considered a net sink, to become a net source which would reduce the size of the global SOC pool (Crowther et al., 2016; Wang et al., 2022).

Northern high latitudes are warming at more than two times the rate of the global average (Rantanen et al., 2022), causing the loss of perennially frozen ground (permafrost) (Van Everdingen et al., 1998; Biskaborn et al., 2019). The deepening and widening of the seasonally thawed active layer of permafrost allows previously frozen SOC to become available for aerobic decomposition and thus the respiratory loss of CO_2 to the atmosphere. Anaerobic decomposition resulting in production of methane can also occur and be later oxidized to CO_2 within the ground column. Thawing permafrost may lead to additional warming and permafrost thaw, i.e., a positive feedback loop (Schuur et al., 2022). A meta-analysis of ecosystem and earth system models (ESM) simulations of SOC stocks estimated that permafrost thaw could cause the release of up to 92 Pg C by 2100 under a business-as-usual climate warming scenario as described by the Representative Concentration Pathway 8.5 (Schuur et al., 2015). Therefore, due to both SOC's mitigation potential and its involvement in a potential positive feedback to climate warming, a better understanding of spatio-temporal distribution of the global SOC stock is of vital importance (Shukla et al., 2019).

Terrestrial biosphere models (TBM) such as the Canadian Land Surface Scheme Including biogeochemical Cycles (CLASSIC; Melton et al. (2020); Seiler et al. (2021)) are useful tools to improve our understanding of SOC dynamics. Some TBMs simulate terrestrial ecosystem processes often as part of ESMs. However, the potential of TBMs has been hampered by large uncertainties in both ESM and offline TBM simulations of SOC stocks (Todd-Brown et al., 2013; Tian et al., 2015; Varney et al., 2022). Using the Coupled Intercomparison Project Phase 5 ensemble (CMIP5, Taylor et al. (2012)), Todd-Brown et al. (2013) reported a mean SOC stock of 1520 Pg, but with a 2493 Pg spread across the eleven ESMs analyzed. Almost a decade later, Varney et al. (2022) reported a smaller mean SOC stock of 1206 Pg with a spread of 1294 Pg across eleven ESMs from the Coupled Intercomparison Project Phase 6 (CMIP6, Eyring et al. (2016)). The latitudinal distribution of SOC across the CMIP6 model ensemble also differs greatly, especially in high latitudes (Varney et al., 2022). Agreement between the CMIP6 ESMs and observation-based estimates from the Harmonized World Soil Database (HWSD, Nachtergaele et al. (2010)) and the World Inventory of Soil property Estimates (WISE30sec, Batjes (2016)) data sets is low in high latitudes (Ito et al., 2020). These difficulties in consistently reproducing SOC stocks and translate into future projections. The spread across model estimates of future changes to global SOC stock demonstrates disagreement across models, with some projecting an increase, and some a decrease, of future SOC stocks (Ito et al., 2020). Disagreement is also seen between the SOC data sets themselves. The HWSD and SoilGrids (Poggio et al., 2021) datasets report largely different value of global SOC stock of 2,400 and 3,400 Pg C respectively, a difference that is even larger in high latitudes (Tifafi et al., 2018). These large differences across SOC data sets are making TBMs evaluation more difficult.

Previous work has shown that differences in simulated global SOC stock among TBMs were partially caused by their parameterization of SOC dynamics, i.e. how soil carbon processes are represented in models via the use of different parameter values (Ogle et al., 2010; Shi et al., 2018; Sun and Mu, 2022). Terrestrial biosphere models represent large numbers of biogeochemical and physical processes requiring parameterization of processes not observable empirically (e.g., microbial processes), and thus require calibration. Parameter calibration is typically done by comparing model outputs to observations and iteratively adjusting parameter values to best reproduce observed quantities by using optimized parameters. Because TBMs can be computationally expensive to run, performing simulations needed for parameter optimization quickly becomes cost-prohibitive. Finding the correct parameter values also comes with challenges. Multiple parameters are needed to fully represent the range of processes simulated by TBMs. For example, the CLASSIC model used in this work contains over 200 parameters. As more processes have been added to TBMs to improve ecological realism (e.g., multiple layer soil carbon representation, permafrost-related processes, nitrogen cycle (Blyth et al., 2021)), each process representation has introduced additional parameters. The increase in the number of parameters can eventually lead to the problem of equifinality, i.e., with many different combinations of parameter values resulting in simulations with an equally good fit to observations (Tang and Zhuang, 2008). Global sensitivity methods can provide information on the influence of individual model parameters on simulated outputs, including identifying parameters that do not influence model outputs (Pappas et al., 2013; Hamby, 1994).

A recent study investigated the main sources of uncertainty and equifinality in TBM simulations of SOC by optimizing the parameters of three different soil carbon schemes using a Monte-Carlo Markov Chain method (Shi et al., 2018). The CENTURY-type model

(Parton, 1996) simulated SOC using three carbon pools without taking into account SOC depth within the ground column. The second scheme was a vertically-resolved model based on the Community Land Model 4.5 (CLM4.5, (Oleson et al., 2013)). The vertically-resolved model simulated SOC dynamics using three SOC pools and ten soil layers to account for depth. While the first two soil carbon schemes used first-order microbial implicit representations, the third scheme was a microbial model (MIcrobial-MIneral Carbon Stabilization, MIMICS, (Wieder et al., 2015)). MIMICS simulates SOC dynamics using two microbial carbon pools as well as three SOC pools to describe SOC uptake by microbes. Shi et al. (2018) used SOC observations from HWSD and the Northern Circumpolar Soil Carbon Database (NCSCD, (Hugelius et al., 2013)) and their Monte-Carlo Markov Chain algorithm to build posterior distributions of the parameters of each soil carbon scheme. Each soil carbon scheme had an increasing number of soil carbon parameters; 10 for the CENTURY-type scheme, 13 for the vertically-resolved scheme, and 22 for the microbial scheme. Parameters contained in the three scheme included, for example, respiration rates, transfer rates between the model's carbon pools as well as some parameters related to environmental conditions (e.g., temperature). Shi et al.'s results showed that while contemporary SOC stocks could be estimated accurately by all models after parameter optimization, the future behavior (2005 - 2100) varied greatly across the different soil carbon schemes. There was no agreement across the three soil carbon schemes on whether the global soc stock would lose or gain carbon over the 21^{st} century. Large variations also occurred within each soil carbon scheme using different parameter sets sampled from the posterior parameter distributions obtained from the Monte-Carlo Markov Chain method. The CENTURY-type model had a spread of 54 Pg in the reported change of the soil carbon pool over the 21^{st} century, the vertically-resolved model had a spread of 805 Pg, and the MIMICS model had a spread of 541 Pg. Shi et al. (2018) identified that model structure, poorly constrained parameters, and initial conditions were the causes of the uncertainties. They also identified that a lack of constraints on SOC parameters was a limiting factor in their optimization and that constraining the parameters with different types of data (e.g., R_{soil} data and isotopic data) could be helpful to overcome this limitation.

Inspired by Shi et al. (2018), we aimed to optimize the parameters of the soil carbon scheme of CLASSIC and improve the model's simulation of SOC dynamics. We addressed equifinality by using observational data sets of SOC stocks and R_{soil} to constrain the parameter of the soil carbon scheme. We performed historical and future simulations (2015-2100) using the optimized parameter sets of our framework. We compared the historical simulations to high-latitude observation-based data sets of SOC and R_{soil} and literature estimates of global SOC totals. We then identified our best-performing parameter set and asses its impact on CLASSIC's simulations of SOC dynamics.

2.5. Methods

2.5.1. The Canadian Land Surface Scheme Including biogeochemical Cycles

The Canadian Land Surface Scheme Including biogeochemical Cycles is the land surface component of the Canadian Earth System Model (Swart et al., 2019) and comprises two component models: the Canadian Land Surface Scheme (CLASS) simulates the physics (Verseghy, 2017) and the Canadian Terrestrial Ecosystem Model (CTEM) simulates the biogeochemistry (Melton and Arora, 2016). In brief, CLASSIC simulates fluxes of carbon, nitrogen, water, momentum, and energy between the land and the atmosphere. Running CLASSIC requires meteorological forcing and ancillary data to parameterize vegetation and soil characteristics. Usually, CLASSIC is run at a 30-minute timestep for the model physics (historically CLASS) and a one-day timestep for the model biogeochemistry (historically CTEM), ranging from site (e.g., (Meyer et al., 2021)) to global scales (e.g., (Kou-Giesbrecht and Arora, 2022)). Here, we used CLASSIC at T63 spatial resolution, corresponding to roughly 2.8° by 2.8°, and the nitrogen cycle module of CLASSIC was turned off. Vegetation in CLASSIC is represented through plant functional types (PFT), i.e., functional groupings of plant species with similar characteristics (Box, 1996). The version of CLASSIC used in this study considered nine PFTs : needleleaf evergreen trees, needleleaf deciduous trees, broadleaf evergreen trees, broadleaf cold deciduous trees, broadleaf drought/dry deciduous trees, C_3 crop, C_4 crop, C_3 grass and C_4 grass (Melton and Arora, 2016).

2.5.2. Soil Carbon Scheme

The soil carbon scheme of CLASSIC was used for the sensitivity analysis and the Bayesian optimization of parameters relevant to SOC dynamics (Arora, 2003; Melton et al., 2015). The soil carbon scheme is based on two SOC pools. A "fast-cycling" litter pool (detrital,D) and a "slow-cycling" soil carbon pool (humified, H), both of which are tracked within each layer of the ground column. The ground column comprises 20 layers reaching a maximum depth of 61.4 m. The first ten layers are each 10 cm thick while the deeper layers gradually increase in thickness with depth to a maximum thickness of 30 m. The soil permeable depth variable distinguishes the soil from the bedrock part of the ground column. In the former, the model tracks soil carbon, thermal and hydrological dynamics, whereas in the latter the model only tracks thermal changes. The detrital pool receives carbon through stem, leaf and root litter. Stem and leaf litter is added at the top layer of the litter pool while root litter is added to the litter following the root soil distribution (an exponential root distribution (Arora and Boer, 2003). Carbon is transferred from the detrital to the humified pool via humification. The change of the detrital and humified pool size, $\frac{dC_D}{dt}$ and $\frac{dC_H}{dt}$ (kg C m^{-2} yr^{-1}), are expressed at every soil layer and for each PFT as:

$$\frac{dC_D}{dt} = C_D - \left(R_D\left(1-\chi\right)\right) \tag{2.5.1}$$

$$\frac{dC_H}{dt} = R_D\chi - R_H \tag{2.5.2}$$

where C_D is the PFT-dependent stem, leaf and root litter carbon input (kg C m^{-2} yr^{-1}) calculated by the biogeochemistry component, and χ is the PFT-dependent humification transfer coefficient (unitless) which represents the fraction of carbon within a timestep that is humified and transferred from the detrital to the humified pool. R_D and R_H are the carbon respired from the detrital and humified pools due to heterotrophic respiration (R_{hetr}) (kg C m^{-2} yr^{-1}), respectively, expressed per PFT and per soil layer as:

$$R_j = \varsigma_j \times C_j \times E_j \text{ with j = D,H} \tag{2.5.3}$$

where ς_j is the PFT-dependent base respiration rate parameter of the pool (kg C(kg C yr)$^{-1}$, C_j is the mass of carbon of the pool at the current time step (kg C m^{-2}), and E_j is the environmental modifier of the pool at the current time step (unitless). The environmental modifier is a scalar dependent upon temperature, moisture and depth, tracked for each layer of the ground column, expressed as:

$$E_j = f_{15}\left(Q_{10_j}\right) f_j\left(\psi\right) f_j\left(z\right) \text{ with j = D,H} \tag{2.5.4}$$

The temperature function $f_{15}\left(Q_{10_j}\right)$ of the environmental modifier is expressed for every soil layer as:

$$f_{15}\left(Q_{10_j}\right) = \begin{cases} Q_{10}^{0.1(T_i-T_0-15))} & if \quad T_i - T_0 > T_{crit} \\ f_r Q_{10}^{0.1(T_i-T_0-15))} & if \quad T_i - T_0 \leq T_{crit} \end{cases} \text{ with j = D,H} \tag{2.5.5}$$

where T_0 is the freezing point of water (°C), T_i is the temperature of the i th soil layer (°C), and T_{crit} is the critical temperature (°C) under which R_{hetr} is reduced by a factor (f_r) similar to Koven et al. (2011). The Q_{10} function is expressed as:

$$Q_{10} = Q_a + Q_b \tanh\left[Q_c\left(Q_d - T_i\right)\right] \tag{2.5.6}$$

where T_i is the temperature of the i^{th} soil layer (°C), and Q_a, Q_b, Q_c, and Q_d are scalars that determine the shape of the Q_{10} function (Fig. S1, Melton et al. (2015)). The moisture function $f\left(\psi\right)$ of the environmental modifier depends on the soil matric potential (ψ in m) as described in Melton et al. (2015), representing different soil moisture conditions at every soil layer:

$\psi > \psi_a$:

$$f_{D,H}(\psi) = 0.2, \tag{2.5.7}$$

$\psi_a \geq \psi > \psi_b$:

$$f_{D,H}(\psi) = 1 - 0.8\frac{\log\psi - \log\psi_b}{\log\psi_a - \log\psi_b}, \tag{2.5.8}$$

$\psi_b \geq \psi \geq \psi_c$:

$$f_{D,H}(\psi) = 1, \tag{2.5.9}$$

$\psi_c > \psi \geq \psi_{sat}$:

$$f_H(\psi) = 1 - 0.5\frac{\log\psi_c - \log\psi}{\log\psi_c - \log\psi_{sat}}, \tag{2.5.10}$$

$$f_D(\psi) = 1, \tag{2.5.11}$$

where ψ_a, ψ_b and ψ_c are matric potential parameters, fixing the limits of the different moisture ranges and ψ_{sat} is the soil matric potential at saturation.

The depth function, $f(z_i)$ (Lawrence et al., 2015), can be expressed as:

$$f(z_i) = e^{-z_i/z_t} \tag{2.5.12}$$

where z_i is the depth of bottom of the i^{th} layer of the pool (m), and z_t is the depth factor parameter (m), which reduces respiration with increasing depth.

The soil carbon scheme also represents turbation, the process by which carbon moves vertically along the ground column. Turbation in CLASSIC is parameterized as a diffusive process that redistributes carbon within the mineral ground column following Koven et al. (2011). This redistribution can allow soil carbon to migrate deeper than where it is initially added, e.g., through root detrital contributions. Turbation is implemented using the Crank-Nicolson method (Crank and Nicolson, 1947). In CLASSIC, turbation uses the active layer depth, the portion of soil that either does not freeze or perennially thaws every year and that is therefore available for respiration. Two turbation mechanisms are simulated: bioturbation (Gabet et al., 2003), which is represented in CLASSIC in soils with an modeled active layer depth deeper than one meter. The second turbation mechanism is cryoturbation (Bockheim, 2007; Vandenberghe, 2013), which occurs through the freeze/thaw cycle in soils, and is represented in CLASSIC within soils with an active layer depth of one meter or less. The two types of turbation in CLASSIC are mutually exclusive and each has its own diffusion coefficient; D_b for bioturbation and D_c for cryoturbation, both in m^2d^{-1}. Beyond the active layer depth turbation follows a linear dependence on depth with a slope determined by the parameter k_{term}

In this work, CLASSIC simulated both SOC content, R_{hetr} and belowground autotrophic respiration (R_a). When required, R_a and R_{hetr} were combined to obtain R_{soil}. R_a is simulated by another component of CLASSIC and is given as an input variable to the soil carbon scheme. Because of this, only R_{hetr} was used in the sensitivity analysis because we wanted to assess the effect of parameters on the soil carbon scheme and therefore did not need R_a contributions from outside of the scheme. In the optimization however, R_{hetr} simulated by the soil carbon scheme was combined to R_a to obtain R_{soil}, which could then be compared to observations.

Table 2.1. Parameters of the soil carbon scheme of CLASSIC. An asterisk (*) indicates plant functional type (PFT)-dependent parameters. The needle leaf evergreen trees (NdlEvgTr) PFT values are listed in the table for those parameters. For all PFT-dependent parameters default value, see Table S1. S_p, S_1, S_2 and S_3 are the different optimization scenarios used in the Bayesian optimization framework (Section 2.5.2). A check mark indicates parameters used in the corresponding scenario. A I indicates one scaling factor for all PFTs, a P indicates one parameter value per PFT.

Short Name	Description	Units	Lower Bound	Upper Bound	Default Value	S_p	S_1	S_2	S_3
χ*	Humification transfer	-	0.336	0.504	0.42 [a]	I	P	P	P
ς_D*	Base respiration rate of detrital pool	$kgC(kgCm^2)^{-1}$	0.35624	0.53436	0.4453 [a]	I	P	P	P
ς_H*	Base respiration rate of humified pool	$kgC(kgCm^2)^{-1}$	0.0208	0.0312	0.0260 [a]	I	P	P	P
T_{crit}	Critical temperature	°C	-1.2	-0.8	-1 [b]				✓
f_r	Respiration reduction factor	-	0.08	0.12	0.1 [d]				
Q_a	Q_{10} function parameter a	-	1.152	1.728	1.44 [a]	✓	✓	✓	✓
Q_b	Q_{10} function parameter b	-	0.448	0.672	0.56 [a]			✓	✓
Q_c	Q_{10} function parameter c	-	0.06	0.09	0.075 [a]				✓
Q_d	Q_{10} function parameter d	°C	36.8	55.2	46 [a]			✓	✓
Ψ_a	Moisture parameter a	-	8000	12,000	10,000 [a]				
Ψ_b	Moisture parameter b	-	4.8	7.2	6 [a]				
Ψ_c	Moisture parameter c	-	3.2	4.8	4 [a]				✓
k_{term}	Cryoturbation depth constant	-	2.4	3.6	3 [a]				
D_b	Rate of bioturbation	$m^2\ d^{-1}$	2.191776×10^{-7}	3.287664×10^{-7}	2.73972×10^{-7} [b]			✓	✓
D_c	Rate of cryoturbation	$m^2\ d^{-1}$	1.096879×10^{-6}	1.64382×10^{-7}	1.36986×10^{-6} [b]			✓	✓
z_t	Depth factor	m	8	12	10 [c]				

[a](Melton and Arora, 2016), [b](Koven et al., 2011), [c](Lawrence et al., 2015), [d](Koven et al., 2009)

2.5.3. Optimization Workflow

The optimization workflow comprised four steps (Fig. 2.1). First, we determined the model parameters relevant to the soil carbon scheme. Three parameters were PFT-dependent (9 PFTs thus 3 parameters with 9 parameter values each, for a total of 21 parameter values), along with 13 parameters which related to the environmental modifier, resulting in 16 parameters corresponding to 34 parameter values (Section 2.5.2). Second, we performed a sensitivity analysis using the Sobol' method (Sobol', 2001) on the 16 SOC parameters (Section 2.5.4). Any non-influencial parameters were identified and excluded from the optimization framework to reduce the possibility of equifinality and also to lower the computational cost by reducing the dimensionality of the search space (Hamby, 1994). Third, based on the sensitivity analysis we developed optimization scenarios using subsets of the original SOC parameters and defined the prior values and potential search space of those parameters. Fourth, we ran the Bayesian optimization over each optimization scenario (Section 2.5.5). The optimization framework simulated SOC stocks and R_{soil} for comparisons with observational data sets (Section 2.5.6) and used a loss function to determine if changes to parameter values were producing model results closer to observations (Section 2.5.7). The optimized parameter sets were then used in historical and future simulations by the CLASSIC framework (Section 2.5.8).

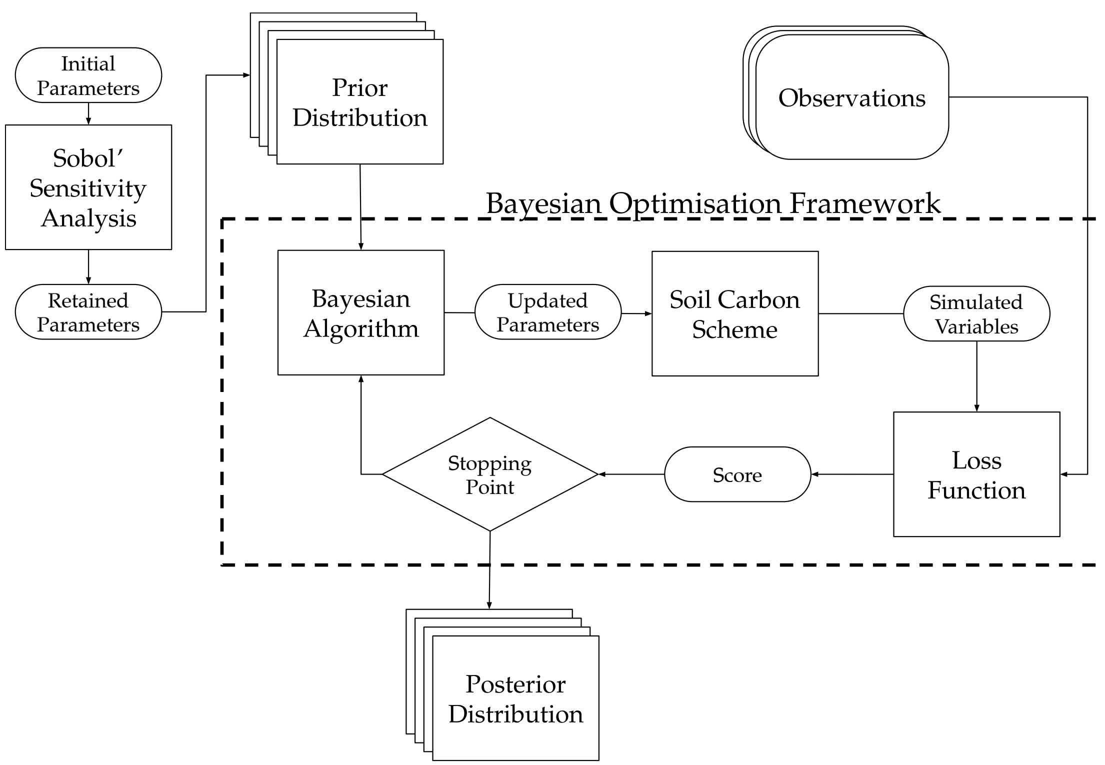

Fig. 2.1. Schematic representation of the optimization workflow

2.5.4. Sensitivity Analysis

Global sensitivity analysis is a common method used to quantify the impact of parameter values on model outputs (Saltelli et al., 2008). Sensitivity analysis with the Sobol' method (Sobol', 2001) is based on variance decomposition which computes a first-order and a total sensitivity index. Here, we used the Python SALib library version 1.4.5 (Herman and Usher, 2017; Iwanaga et al., 2022) to compute the sensitivity indices. The first-order index ($SI_{1,i}$) is expressed as the fraction of the total model variance attributed to a single parameter:

$$SI_{1,i} = \frac{V_i}{V[Y]} \tag{2.5.13}$$

where V_i is the variance of the conditional mean of the model output when parameter X_i is fixed within its range, and $V[Y]$ is the variance of the model output Y. The total sensitivity index ($S_{T,i}$) is the fraction of variance caused by a parameter and its interactions with other parameters. The total sensitivity index of the i^{th} parameter can be expressed as:

$$SI_{T,i} = \frac{V_{\sim i}}{V[Y]} \tag{2.5.14}$$

where $V_{\sim i}$ is the variance of the conditional mean of Y when all parameters except X_i are fixed. For each of the parameters, we fixed a range of ± 20 % of the default value (Table 2.1), based on literature (Ricciuto et al., 2021). For PFT-dependent parameters, we assumed that the relative differences between PFTs were appropriate and thereby used a single parameter to represent all PFTs which adjusted the parameter values up or down while leaving their relative differences unchanged (Pappas et al., 2013). This simplification reduced the number of parameters included in the Sobol' analysis from 34 to 16. We used a Saltelli sampling scheme (Saltelli, 2002) to generate the parameter sets needed for the Sobol' analysis. The Saltelli sampling scheme determines the number of experiments, N, such that $N = n(2p+2)$, where n is the number of simulations required to compute the Sobol' indices and p is the number of parameters included in the analysis. Each of the n simulations therefore requires $2p$+2 model simulations. Previous work showed that Sobol' sensitivity indices of 19 parameters stabilized after about 150,000 experiments (Jaxa-Rozen and Kwakkel, 2018). Based on our 16 parameters, we used $n = 4096$, resulting in $N = 139{,}264$. Fig. S2 demonstrates that stability was achieved with that n value. Given the large number of model simulations (N) required by the Sobol' method, performing global simulations was prohibitively computationally expensive. Thus, we ran the soil carbon scheme for three sites where the eddy covariance technique is used to quasi-continuously measure carbon dioxide, and latent and sensible heat fluxes at ecosystem-scale (Baldocchi, 2003). The three sites were selected to present a range of temperature, moisture and soil conditions (Table 2.2).

Table 2.2. Characteristics of the eddy-covariance sites used in the sensitivity anlaysis. MAAT: mean annual air temperature; MATP: mean annual total precipitation; Permafrost extent is defined following (Gruber, 2012) (absent: 0 %, continuous:90-100 %)

Site name (ID)	Latitude, longitude	MAAT (°C)	MATP (mm)	Permafrost extent	Years of data	Vegetation	Data source
Trail Valley Creek (CA-TVC)[1]	68.75° N, 133.50° W	-8.2	240.6	Continuous	2013-2020	Arctic tundra	[a]Ameriflux
Hyytiälä (FI-Hyy)[2]	61.85° N, 24.29° E	3.8	709	Absent	1996-2015	Evergreen needleleaf forest	[b]FLUXNET2015
Ankasa (GH-Ank)[3]	5.27° N, 2.69° W	26	1900	Absent	2011-2015	Evergreen broadleaf forest	FLUXNET2015

[1] (Sonnentag and Marsh, 2021), [2] (Keronen et al., 2004), [3] (Chiti et al., 2010), [a] (Pastorello et al., 2021), [b] Novick et al. (2018)

We calculated Sobol' indices using simulations of SOC content and R_{hetr} at each of the eddy covariance sites. The soil carbon scheme used climate variables provided by CLASSIC that were derived from eddy covariance data from each of the site. Soil organic carbon content was obtained by calculating the total (detrital and humified pools) SOC content summed across all soil layers and the mean across the respective eddy covariance observational period (Table 2.2). Heterotrophic respiration was obtained by computing the mean daily R_{hetr} (detrital and humified pools) over the same periods at each site. For each of the three sites, the soil carbon scheme was run for 80,000 days (ca. 220 years) prior to the sensitivity analysis by looping over the available observed meteorological forcing data (Table 2.2). This length was selected to allow the model to respond to the new parameter values while keeping the sensitivity analysis at a reasonable computational cost.

Guided by the sensitivity analysis, we generated four optimization scenarios: S_p, S_1, S_2 and S_3 (Table 2.1). The parameters that were selected for scenario S_p and S_1 were parameters that had a SI_1 higher than 0.1 for at least one site and one simulated variable i.e., SOC and/or R_{hetr}. Scenario S_p differed from S_1 by using a single scaling factor for each PFT-dependent parameters χ, ς_D and ς_H, following the same assumption used in the sensitivity analysis, i.e., a single value was optimized and that value was then translated to each PFT's parameter value while keeping their relative differences unchanged. Both S_1 and S_p scenarios did not include turbation parameters. Scenario S_2 expanded the number of parameters to include those that had a SI_1 above 0.02 for at least one site and one simulated variable, but also included the turbation parameters. Scenario S_3 included all parameters that had a first-order sensitivity index above zero and an error range that was not encompassing zero. Parameters that were not included in any scenario due to a demonstrated lack of sensitivity were set to their CLASSIC default value and used as such in the optimization (Table 2.1). The four scenarios thus had an increasing amount of parameter values (S_P: 4, S_1: 22, S_2: 26 and S_3: 29 parameters).

2.5.5. Bayesian Optimization Framework

Bayesian optimization approaches have proven valuable in the optimization of parameters within TBMs (Hararuk et al., 2014; Shi et al., 2018). The ability to use and update the knowledge of the parameter search space as the optimization progresses makes Bayesian optimization approaches suited for the large and complex parameter search space of TBMs (Shahriari et al., 2016; Williams et al., 2009).

Our Bayesian optimization framework used a Tree of Parzen Estimator (TPE) algorithm provided by the Python library hyperopt version 0.2.5 (Bergstra et al., 2013). The TPE algorithm is a sequential model-based optimization method (Hutter et al., 2011) that aims to create less computationally expensive probabilistic model surrogates for optimization, rather than using the model itself. The TPE algorithm first starts by randomly sampling the search space (in our framework, the defined range of each parameter) to initiate the optimization. It then gathers vectors of parameters that correspond to coordinates, or parameter sets, in the parameter space. For each sample vector, $\mathbf{x}$, the algorithm calculates the score, y, associated with the vector, $\mathbf{x}$ by using the loss function provided by the user. The sample points are then split in two groups. The first group is populated by the best performing sample points, i.e., the parameter sets that yield the best y-values, and the second group contains the remainder. The separation point between the two groups can be expressed by a variable y', a loss-value threshold that decides where the split occurs. The likelihood probability of being in each group is calculated as $p(\mathbf{x}|y) = l(\mathbf{x})$ for $y < y'$ and $p(\mathbf{x}|y) = g(\mathbf{x})$ for $y >= y'$, where $g(\mathbf{x})$ is the likelihood probability of being in the best performing group and $l(\mathbf{x})$ is the likelihood probability of being in the group that contains the remainder of the sample points. Those two probability densities are then modeled using Parzen estimators (Bergstra et al., 2011). Next, the probability $p(y)$ is calculated using $p(y < y') = \gamma$, which defines $p(y)$ in terms of the percentile split in the two categories. For example, if the best performing group is defined so that it uses the top quartile of parameter vectors, then γ is assigned the value 0.75. Using the densities of the two groups and the probability $p(y)$, the algorithm finds the next best point in the parameter search space using an approximation of the expected improvement expressed as a ratio of $l(\mathbf{x})/g(\mathbf{x})$ (Bergstra et al., 2011) which can be derived from Bayes theorem, i.e., $p(y|x) = p(x|y)p(y)/p(x)$. The next parameter vector used in the optimization is taken as the parameter vector **x'** that yields the maximum value of the ratio $l(\mathbf{x})/g(\mathbf{x})$. The surrogate model is then updated with this new parameter vector and the next optimization trial starts.

2.5.6. Global Observational Data Sets

We used two global observational data sets in the optimization framework to constrain simulated R_{soil} and SOC. Soil organic carbon data were extracted from the World Soil Information Service (WoSIS; (Batjes et al., 2020)). Here, we focused on organic carbon content in mineral soils, thus WoSIS observations containing more than a 5 % organic carbon content were excluded as they were most likely associated with non-mineral soils and processes that are not represented by the CLASSIC mineral soil carbon scheme, e.g., peatlands (Stockmann et al., 2015), Yedoma deposits (Elias et al., 2013; Strauss et al., 2013), and deltaic alluvial deposits (Hugelius et al., 2014). Also, the parameters of the C_3 and C_4 crop PFTs of CLASSIC were kept at their default values and not optimized as they are associated with anthropogenic land-use and land-use change, which are processes the soil carbon scheme itself does not explicitly simulate. The SOC content in WoSIS is given in g C kg^{-1}, which was converted to kg C m^{-2} using globally gridded bulk density (BD) values from the SoilGrids version 2.0 data set (Poggio et al., 2021) whose machine learning prediction models were fitted using WoSIS' soil profiles. We used SoilGrids' BD values because relatively few of the soil carbon observations in WoSIS also had concomitant BD values and using them would have significantly reduced the number of observations to compare the simulated SOC against. Out of the 438,036 WoSIS soil profiles passing our <5 % threshold, only 20,078 of them (ca. 4.6 %) had an associated BD value. Using SoilGrids' BD permitted the number of usable soil profiles to remain high at 436,353 (ca. 99.6 %). A small number of soil profiles (1,683) were located outside of the CLASSIC global grid and therefore were excluded. Annual R_{soil} data were extracted from the Soil Respiration Database version 5 (SRDB; (Jian et al., 2020)) and converted from g C m^{-2} yr^{-1} to kg C m^{-2} yr^{-1}. In total, 1172 annual R_{soil} estimates spanning a time period of 55 years (1960 - 2015) were extracted from the SRDB. Between the two data sets, WoSIS has a greater spatial coverage as well as more observations (Fig. 2.2). WoSIS has a sampling bias towards the United States where most of the measurements are located. A similar issue is present in SRDB with sites primarily located in the United States, Europe and China. Generally, the southern hemisphere as well as high latitudes are underrepresented in both data sets. In addition, WoSIS and SRDB are generally biased towards temperate ecosystems.

The WoSIS and SRDB data sets contain site-level observations, thus both data sets required additional aggregation to allow comparison against grid-level model outputs. For WoSIS, all observations made at the same soil depth within a model grid cell were averaged and their standard deviation was calculated. That mean value, termed a comparison point, was then used against the soil carbon scheme's simulated soil carbon content for that same grid cell at the same depth in the ground column by linear interpolation from the model ground layer discretization if required (Fig. 2.2(A), n = 74,309 comparisons). For SRDB, annual R_{soil} observations made within a model grid cell over the same time period were averaged and their standard deviation was calculated. The mean value, termed a comparison point, was then used against the soil carbon scheme's simulated R_{soil} (Fig. 2.2(B), n = 1120 comparisons).

2.5.7. Soil Carbon Scheme-Data Comparison Using Loss Functions

At each optimization trial, the soil carbon scheme was run until it reached equilibrium (defined in Section S1). Once equilibrium was reached, the total SOC mass (detrital and humified pools) in each soil layer as well as the total R_{soil} across all soil layers were outputted daily over the period 1961 to 2017, corresponding to the temporal coverage of

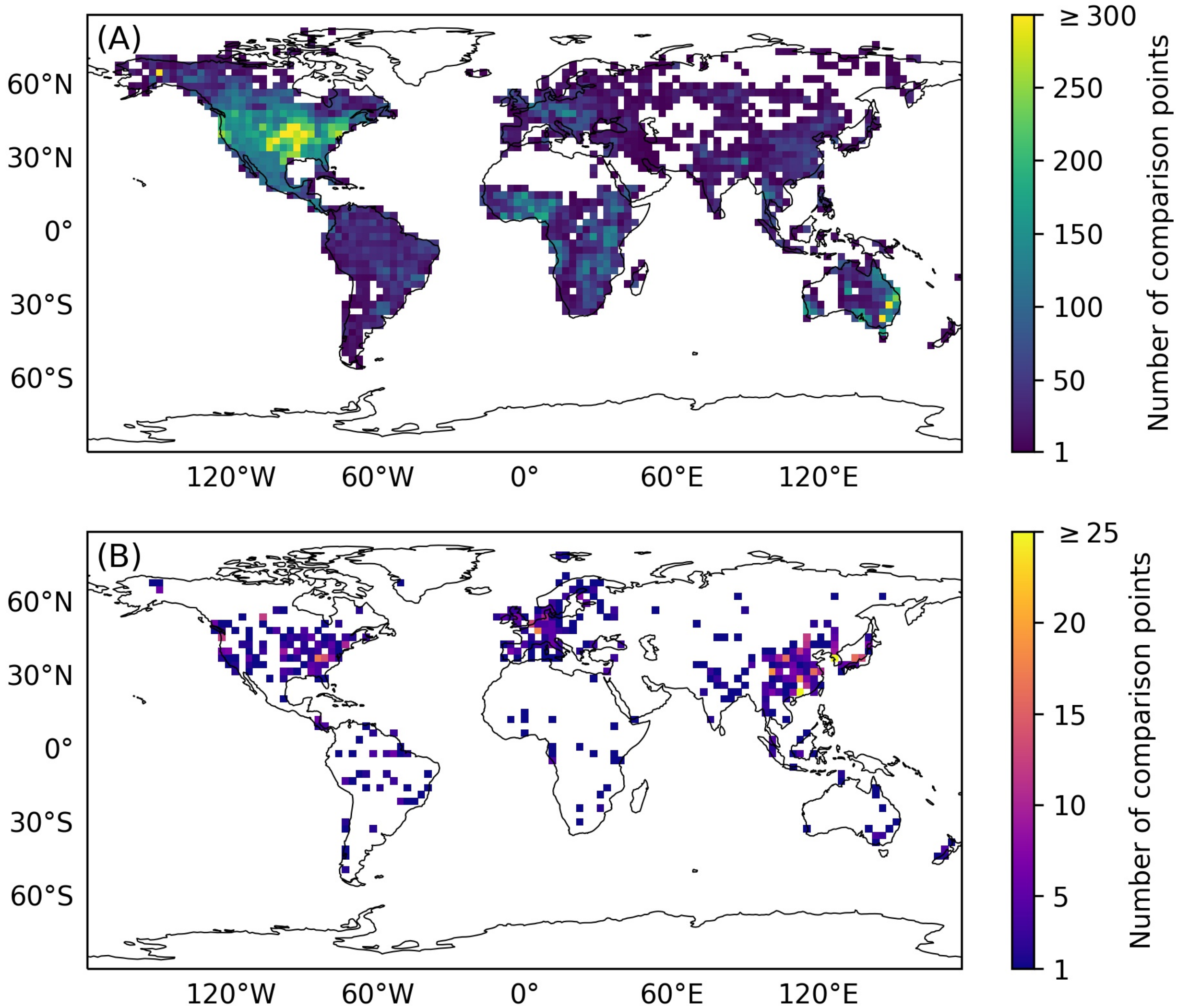

Fig. 2.2. Spatial distribution of the number of comparison points between the aggregated observations and the soil carbon scheme grid cells. (A) World Soil Information Service (WoSIS) data set (Batjes et al., 2020), n = 74,309 and (B) Soil Respiration Database version 5 (SRDB) (Jian et al., 2020), n = 1120. The color bar indicates the number of comparison points, contained within the bounds of a CLASSIC grid cell. All grid cells containing 300 or more WoSIS data points are the same color, All grid cells containing 25 or more SRDB data points are the same color ; white means that no observations are contained within the grid cell.

the SRDB and WoSIS.

To compare the WoSIS soil profiles to the simulated SOC content, we derived a typical observational error $\hat{\sigma}_T$. To do so, we first calculated the normalized standard deviation of each comparison point. We defined a comparison point $\bar{x}$ as the average value of all same-depth WoSIS observations within a grid cell:

$$\bar{x}_k = \frac{1}{N_k}\sum_{l=1}^{N_k} x_l \tag{2.5.15}$$

Where k is the index corresponding to the k^{th} depth value within the grid cell. We then calculated the standard deviation of the comparison point as well as its normalized standard deviation:

$$\sigma_k = \sqrt{\frac{1}{N_k}\sum_{l=1}^{N_k}\left(x_l - x_k\right)^2} \tag{2.5.16}$$

$$\hat{\sigma}_k = \frac{\sigma_k}{\bar{x}_k} \tag{2.5.17}$$

Where $\hat{\sigma}_k$ is the normalized standard deviation expressed as a fraction of the average observed value within a gridcell and soil layer. Therefore, since all normalized standard deviations were expressed as a fraction of their associated mean value, we were able to compare the $\hat{\sigma}_{j,k}$, where j is the index of the j^{th} grid cell, to understand what was the derived error. The derived error represented the uncertainty due to measurement error, our upscaling of the observational data sets to match CLASSIC's resolution and sub-grid heterogeneity. We then built a population of all the normalized standard deviations with their associated N for all the n comparison points; $P_n = \{(\hat{\sigma}_1,N_1), ...,(\hat{\sigma}_i,N_i), ..., (\hat{\sigma}_n,N_n)\}$. This gave us n pairs of normalized standard deviations and the number of observations that they were computed from. We then ordered population P by the value N of each comparison point: $P_{(n)} = \left\{(\hat{\sigma}_{(1)},N_{(1)}), ...,(\hat{\sigma}_{(i)},N_{(i)}), ..., (\hat{\sigma}_{(n)},N_{(n)})\right\}$. Then we built a new sample using the top quartile from P: $S = P_{(i)\geq Q3} = \left\{(\hat{\sigma}_{(i)\geq Q3}, N_{(i)\geq Q3)})\right\}$. Then we calculated the mean of all $\hat{\sigma}$ in S:

$$\hat{\sigma_T} = \frac{1}{M}\sum_{i\geq Q3}^{M}\left(\left\{\hat{\sigma}_{(i)\geq Q3}, ..., \hat{\sigma}_n\right\}\right) \tag{2.5.18}$$

Where $i \geq Q3$ indicates that the sum is over all elements of the top quartile and M is the number of $\hat{\sigma}_i$ contained in the top quartile. We chose to use the top quartile of P because most of the comparison points were computed from relatively few observations which would have led to an under-estimation of $\hat{\sigma}_T$ as all $\hat{\sigma}$ computed from one observation is 0. We estimated a $\hat{\sigma}_T$ of 0.7995 for the WoSIS data set. For SRDB, we assumed $\hat{\sigma}_T$ equaled 1 due to the smaller number of observations.

To compute the score resulting from the model-data comparison, we derived two different loss functions. The first, termed the error-oriented (EO) loss function, was defined as:

$$L_{EO} = \frac{1}{n}\sum_{i=1}^{n}\hat{\sigma_T}\left(\frac{1}{\nu_i}\left(x_i - \nu_i\right)\right)^4 \tag{2.5.19}$$

where n is the number of data points for comparison, $\hat{\sigma}_T$ is the derived observational error, ν_i is the observation value at a certain soil layer in a grid cell i for comparison (Section

2.5.6) and x_i is the modeled value. The formulation of L_{EO} assigned a lower (better) score to a simulated value that fell within the interval of $\pm\hat{\sigma}_T$. When the modeled value was outside this interval, L_{EO} assigned a higher (worse) score (Fig. S3). This weighting of the loss function favored parameter sets that resulted in the model outputs being within observation uncertainty instead of primarily trying to match the mean observed value. The second, termed the mean-oriented (MO) loss function, was defined as:

$$L_{MO} = \frac{1}{n}\sum_{i=1}^{n}\left[1 - e^{-\left|\frac{1}{\nu_i}(x_i - \nu_i)\right|}\right] \tag{2.5.20}$$

L_{MO} assigned a lower (better) score to simulated values closer to the observed value, without specifically accounting for observational error (Fig. S3). The L_{MO} was inspired by the bias score used in the benchmarking of CLASSIC (Seiler et al., 2021). Both loss functions yielded scores with an optimal value of 0. The maximum value (worst score possible) for L_{MO} was 1. The maximum value for L_{EO} was constrained to 100 to lessen the influence of outliers in the observations due to the exponent in equation 2.5.19.

At every optimization trial, the selected loss function calculated the score for each data set. Then, the average of the WoSIS and SRDB scores was taken, resulting in a single score that was passed to the TPE algorithm. Therefore, for every optimization trial, we obtained the parameter values and the score of the optimization trial, which we used to build the posterior parameter distributions. We ran the Bayesian optimization framework through 2000 optimization trials, for each loss function, and for each optimization scenario, resulting in eight optimization runs. The 2000 trials stopping point was chosen as all runs had not improved their best score past 1,400 trials. We identified the optimization runs as S_{XYY}, where X identified the optimization scenario used in the optimization run (P, 1, 2 or 3). YY identified the loss function used in the optimization run (EO or MO). For the optimization runs, we set the prior distribution of the parameters to be uniformly distributed on an $\pm$ 50% interval of the default value (Table 2.1, Table S1) except for parameters $\varsigma_{D,BdlDCoTr}$ and $\varsigma_{D,BdlDDrTr}$ which had an upper bound limited to 1 as a higher value would have led to non-physical representation of SOC dynamics (e.g., respiration of more carbon than contained in the pool).

2.5.8. Historical and Future Simulations with CLASSIC

To perform historical (1850 - 2014) and future (2015-2100) simulations, CLASSIC was run with the optimized parameter values from the optimal scenario calculated by each loss function as well as the default parameter values (S_{DEF}, Table S1). For each simulation, historical and future meteorological forcing came from the MPI-ESM1-2-HR ESM from the ISIMIP protocol (Reyer, 2022). The ISIMIP protocol provided historical and future

CO_2 concentrations (Büchner, 2021) and historical and future population density (History database of the Global Environment (HYDE version 3.2), (Klein Goldewijk et al., 2017; Jones and O'Neill, 2016). Historical and future land cover were prescribed using the European Space Agency Climate Change Initiative (ESA-CCI, Li et al. (2018)) land cover product translated to CLASSIC's nine PFTs and adjusted with CMIP6 crop area projections (Chini et al., 2021; Hurtt et al., 2017a,b,c) whenever ESA-CCI land cover was not available. CLASSIC was first spun-up using ISIMIP-provided pre-industrial meteorological forcing for 1601-2100. A constant-year 1851 atmospheric CO_2 concentration was used. CLASSIC's fire disturbance module was turned on, which meant impact of wildfires on ecosystems were simulated, but population density was kept constant at 1851 levels for the duration of the spinup. Land cover was kept constant at 1851 distributions during spinup and the CLASSIC nitrogen cycle module was turned off for all runs. CLASSIC looped on the meteorological forcing until it reached equilibrium which was defined by a global sum net biome productivity of < 0.05 Pg C yr^{-1} averaged over the last 500-year spinup loop.

Once CLASSIC reached its equilibrium state, the historical simulations were launched from the spinup model state and used the bias-corrected MPI-ESM1-2-HR historical meteorological forcing from ISIMIP for 1850-2014. During the historical simulation, atmospheric CO_2 concentration was allowed to evolve over the 1850 to 2014 period using the ISIMIP meteorological forcing data. Similarly, fire disturbance, population density and land cover were transient over the 1850-2014 time period.

The future simulations were started from the end of the historical simulations and used the ISIMIP-provided bias-corrected SSP370 ("regional rivalry") meteorological forcing from the MPI-ESM1-2-HR ESM for 2015-2100. Transient 2015-2100 atmospheric CO_2 concentrations, population density and land use change for SSP370 were used in the simulation.

To distinguish and identify which of the parameter set generated by the two loss functions simulated more reasonable SOC and R_{soil}, we used observation-based estimates that were not used in the optimization. To evaluate simulated SOC, the NCSCD observation-based data set was used. The NCSCD provides SOC stocks over the northern circumpolar permafrost region (>60° N). For R_{soil}, the Gridded Winter Soil CO2 Flux Estimates for pan-Arctic and Boreal Regions (henceforth GWSFE, (Watts et al., 2019)) from NASA's Arctic-Boreal Vulnerability Experiment was used. The GWSFE provided gridded estimates of R_{soil} for the pan-Arctic and Boreal permafrost regions (>49° N). For SOC comparisons, we converted the SOC stocks for the upper one meter of the NCSCD from hg C m^{-2} to kg C m^{-2} before regridding the data set from its native resolution of 1° to the CLASSIC T63 grid resolution (ca. 2.8°). All regridding was done with the xESMF regridder library version 0.6.3 in Python using the bi-linear algorithm (Da et al., 2002). The CLASSIC outputs were summed over the first meter of the ground column and were averaged over the 1950-2000 period of the historical simulation to allow comparison with the NCSCD processed data. For R_{soil} comparisons, we selected GWSFE R_{soil} data between 2003 and 2014 to be within the 1850-2014 time period of the historical simulation. We then converted the GWSFE R_{soil} values from g C m^{-2} d^{-1} to kg C m^{-2} s^{-1} and re-gridded the data from its native 25 km resolution to T63. CLASSIC's winter (September-April) R_{soil} during the 2003-2014 period was used to match the time period of the GWSFE R_{soil} estimates. We then calculated the mean R_{soil} for GWSFE and CLASSIC over that time period, obtaining a grid cell R_{soil} value for both CLASSIC and the regridded GWSFE data set.

An analysis of the model bias was performed by computing the difference (CLASSIC simulation - Observation-based reference dataset) in simulated SOC and R_{soil} at every grid cell of the data set domain between the default parameterization CLASSIC run and both NCSCD and GWSFE. Then, the spatial comparison between the default model parameterization (S_{DEF}) and the optimized parameter sets (S_{2EO} and S_{2MO}) was made by computing the difference (Default - Optimized) at every grid cell of the data domain; NCSCD for the SOC comparison, GWSFE for R_{soil} comparison. We also computed three global metrics including the root mean square difference (RMSD), bias and relative bias, defined as:

$$RMSD = \sqrt{\sum_{i}^{n} \frac{(x_i - y_i)^2}{n}} \tag{2.5.21}$$

$$bias = \sum_{i}^{n} \frac{x_i - y_i}{n} \tag{2.5.22}$$

$$bias_{rel} = \sum_{i}^{n} \frac{1}{n} \frac{x_i - y_i}{y_i} \tag{2.5.23}$$

Where x_i is the simulated value at the ith grid cell, y_i is the observation-based data set value at the ith grid cell and n is the number of grid cells being compared, where n=382 and n=316 for NCSCD and GWSFE respectively. The three metrics were calculated for the historical runs of the default and optimized parameters.

Soil organic carbon content from the first meter of the ground column was used in the computation of simulated global totals as it matched the depth of most estimates. Northern latitudes simulated totals were computed similarly using the SOC content from grid cells contained within a 60N to 90N latitude interval. For both global and northern-latitude totals, the SOC simulations were time-averaged over the 1950-2000 period.

2.6. Results & Discussion

2.6.1. Sensitivity Analysis

The sensitivity indices showed that certain parameters did not contribute appreciably to the soil carbon scheme's variance (Fig. 2.3). Parameters with a SI_1 of 0 or with an error range encompassing 0 across the three sites (CA-TVC, FI-Hyy, GH-Ank, Table 2.2) for both simulated variables (SOC and R_{hetr}) were assumed to not contribute to the soil carbon scheme's variance and were hence termed insensitive and thus not included in the optimization i.e., k_{term}, f_r, ψ_a, ψ_b, and z_t (Fig. 2.3, Table 2.1). An exception was the cryoturbation diffusion coefficient, D_c. Despite D_c being insensitive, it was included alongside the diffusion coefficient for bioturbation, D_b, in the optimization scenarios S_2 and S_3 because D_c and D_b are mutually exclusive. Only optimizing D_b would otherwise lead to the turbation parameterization being optimized at only certain grid cells.

We found the sensitivity of the parameters to vary depending both on the site examined and the output variable (SOC and R_{hetr}). For example, at CA-TVC the base respiration rate parameter for the humified pool, ς_h, had the second highest SI_1 when computed from SOC content (Fig. 2.3, (A)), which dropped when computed using R_{hetr} (Fig. 2.3, (D)). Another example is Q_a, which had a similar SI_1 for CA-TVC and GH-Ank (0.41 $\pm$ 0.03 and 0.37 $\pm$ 0.02 respectively) but had a significantly lower SI_1 for FI-Hyy (0.12 $\pm$ 0.01) (Fig. 2.3, (A-C)). The parameters most impacted by varying site conditions included the temperature parameters Q_b and Q_d, moisture parameter ψ_c, and base respiration rate parameters ς_D and ς_H.

The temperature parameter Q_a contributed the most variance to the simulated variables (SOC and R_{hetr}) in all cases except for the SOC content simulated at the FI-Hyy site where it had the third highest SI_1 (Fig. 2.3, (A)). Q_a is a parameter used in the computation of the temperature scalar that has a linear influence on the Q_{10} temperature function (eq 2.5.6). Thus, a variation in Q_a results in a change in $f_{15}(Q_{10})$ over the whole range of simulated soil temperature (Fig. S1). In contrast, other temperature parameters such as Q_d only had a significant SI_1 at GH-Ank (Fig. 2.3, (C,F)). Parameter Q_d affects the temperature function by shifting and increasing the peak temperature of the Q_{10} function, which had a default value of 46°C (Fig. S1). Therefore, a change in Q_d had little impact on the temperature scalar at the two sites with cold soils, i.e., CA-TVC and FI-Hyy, but the

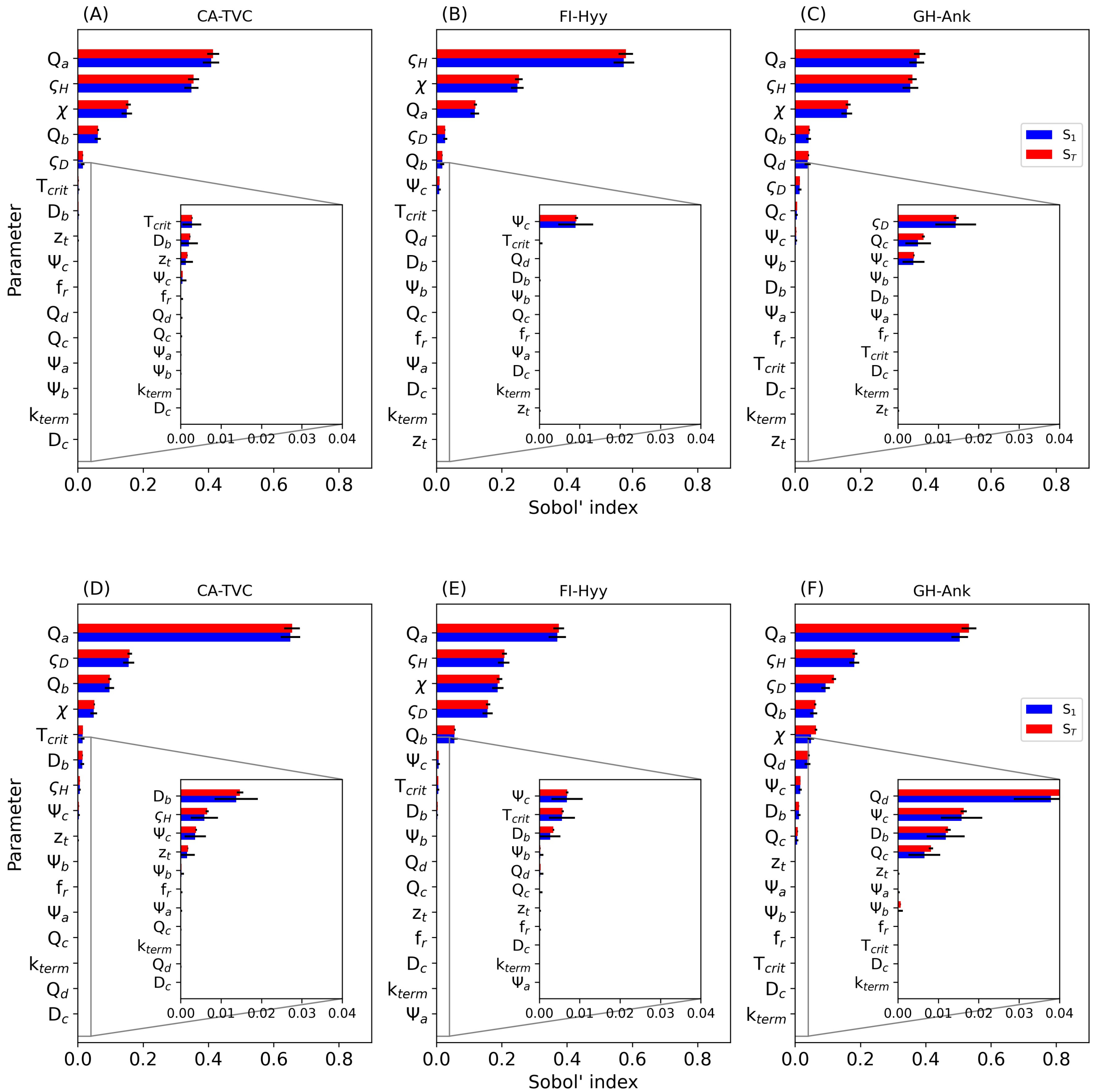

Fig. 2.3. First order (SI_1; in blue) and total (SI_T; in red) Sobol' sensitivity indices when simulating soil organic carbon (SOC) content (A-C) and heterotrophic respiration flux R_{hetr} (D-F) for each parameter of the soil carbon scheme of the Canadian Land Surface Scheme Including Biogeochemical Cycles(CLASSIC; Table 2.1). The indices are computed for three sites: CA-TVC, FI-Hyy and GH-Ank (Table 2.2). Inserts in the figures show parameters with sensitivity indices between 0 and 0.04. Error bars (in black) indicate the 95 % confidence interval.

change had more impact at the site where soils are warm, i.e., GH-Ank.

Other highly sensitive parameters were the base respiration rate parameters, ς_D and ς_H. Base respiration rate parameters always had the first or second highest SI_1 across all sites and simulated variables (Fig. 2.3) as they directly multiply the SOC content of the pool to determine R_{hetr} (eq. 2.5.3). ς_H generally had a higher SI_1 than ς_D, except for simulated R_{hetr} at CA-TVC.

Of the three moisture parameters (ψ_a, ψ_b and ψ_c), only ψ_c was sensitive (Fig. 2.3). In the moisture function (eq 2.5.7 - 2.5.11), ψ_c controls the optimum soil moisture range for R_{hetr}. The sensitivity index for ψ_c was generally higher at GH-Ank than at the other two sites. When simulating R_{hetr}, ψ_c contributed more to the variance of R_{hetr} in sites with higher precipitation, e.g., GH-Ank than sites with lower precipitation, e.g., CA-TVC.

Our sensitivity analysis demonstrated that the soil carbon scheme's parameter sensitivity was dependent upon environmental conditions and weither SOC or R_{hetr} was being simulated, highlighting the complexity of the soil carbon scheme and its parameterization. The observed differences between sites and output variables indicated that diverse climatic conditions and multiple model outputs had to be included to fully capture the model parameters' sensitivity.

2.6.2. Bayesian Parameter Optimization

All optimization runs had a better final score (see Section 2.5.7) than the default parameter set (S_{DEF}), indicating that the optimization framework was able to find parameter sets that improved upon the performance of the CLASSIC default parameters (Fig. 2.4). Scenario S_3 ranked last and second last among the scores of all the scenarios for loss functions L_{EO} and L_{MO}, respectively. S_3 is the scenario with the most parameters. Higher dimensionality is a well-known challenge of parameter optimization (Shan and Wang, 2010) and is difficult to overcome. It often leads to equifinality, where the high number of parameters inevitably leads to many parameter values simulating similar outputs (Fisher and Koven, 2020). Given the same number of optimization trials, scenario S_3 had worse scores because, for the same optimization length, the algorithm had a larger search space to cover and could not do so effectively. Scenario S_P had the third and second best score for L_{EO} and L_{MO}, respectively. Despite S_P having the smallest number of parameters, i.e., the smallest search space, it is possible that it was hampered by the fixed relationship between PFTs (Section 2.5.4). Scenario S_1 had the second best and worst score for L_{EO} and L_{MO}, respectively. For both the EO and MO loss functions, scenario S_2 yielded the best score (2.754 and 0.500 for S_{2EO} and S_{2MO}, respectively, Fig. 2.4). Thus, the remaining analysis was based on the two S_2 optimization runs.

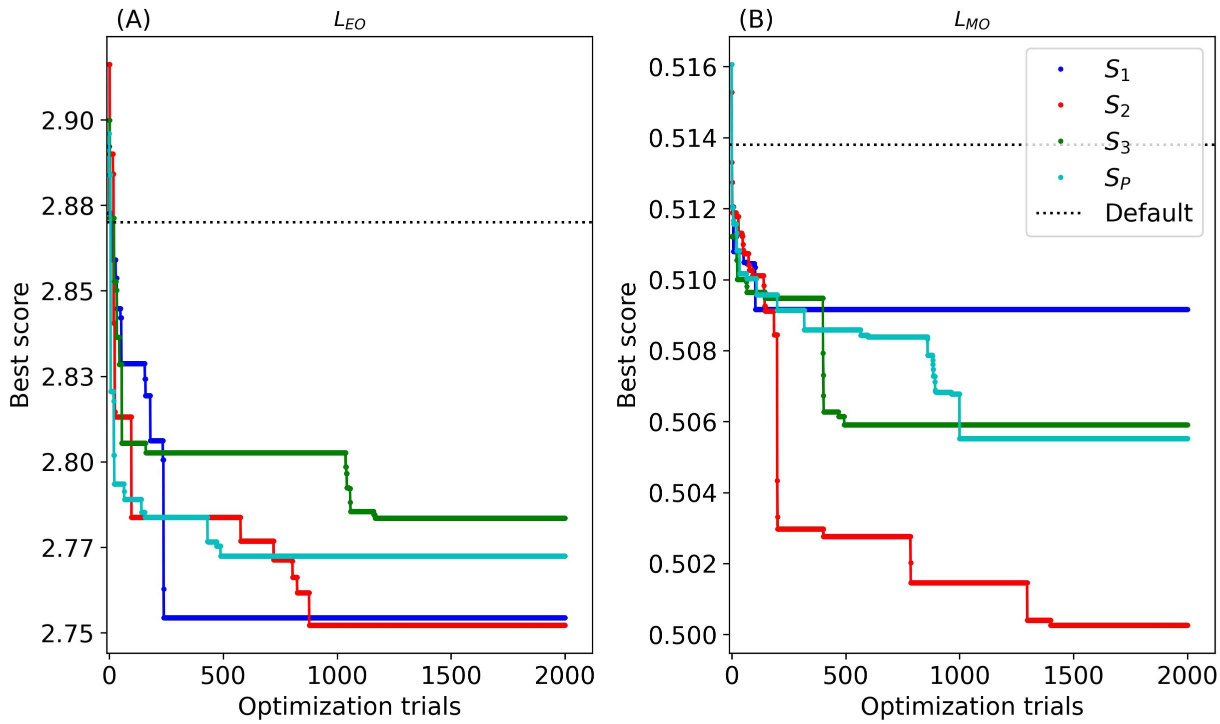

Fig. 2.4. Best score obtained during the optimization run for each optimization scenario (S_1, S_2, S_3 and S_p) and for each loss function ((A): L_{EO}; eq. 2.5.19, and (B): L_{MO}; eq. 2.5.20). Each line represents one optimization run using one scenario and one loss function. The score value (y-axis) at each optimization trial (x-axis) is the lowest (best) score obtained until that point. The dotted black line indicates the score yielded by using the default parameter set.

We generated the posterior parameter distributions for the two S_2 optimization runs using the last 600 out of 2000 optimization trials because at that point, all optimization run had not improved their score after the 1400^{th} optimization trial (Fig. S4, 2.5).

In the S_{2MO} run, the optimization framework constrained the parameter distributions reasonably well, apart from $\chi_{BdlEvgTr}$ which was the least constrained distribution. None of the parameter distributions in S_{2MO} had a bimodal shape with equally strong modes potentially indicating that the S_{2MO} optimization run provided better constrained posterior parameter distributions than the S_{2EO} run. Some distributions such as $\chi_{BdlDDrTr}$ and $\varsigma_{D,BdlDCoTr}$ did have two modes but in each case one of them was smaller. For both parameters, the search history (Fig. S5) indicated that most of the parameter values tried by the algorithm were centered around the best parameter value except for small clusters of values attempted away from the final best value. While the small clusters can indicate that the algorithm found a better value, the score did not improve, and therefore it is more likely that the second, smaller mode of the $\chi_{BdlDDrTr}$ and $\varsigma_{D,BdlDCoTr}$ parameter distributions was just a result of the algorithm exploring potential values within the search space.

In the S_{2EO} run, the optimization framework also produced posterior estimates with constrained distributions, e.g., Q_a, $\varsigma_{H,BdlDCoTr}$ and $\varsigma_{D,BdlDCoTr}$. However, some parameter distributions had a bimodal shape, e.g., Q_b, Q_d with similar modes. A closer look at the search history of the Q_b and Q_d parameters (Fig. S6) indicated that parameter values oscillated around two values, likely indicating equifinality since the two values did not lead to an improvement in the score.

In most cases, the best parameter value was contained within the main cluster of the distribution. One outlier is $\chi_{GrassC3}$ for the S_{2MO} run. In this case, the best parameter value is at the very end of the distribution, not at all near the cluster of the distribution. A closer look at the search history of the $\chi_{GrassC3}$ parameter (Fig. S5) showed that the best parameter value was obtained at the very start of the interval used to generate the posterior parameter distributions and that all subsequent parameter values were on the opposite side of the range from the best parameter value, which could indicate a failure of the algorithm to optimize this specific parameter.

For some parameters, the distribution and the best value were at the end of the allowed parameter range. Examples include $\varsigma_{GrassC4}$ and $\varsigma_{D,BdlDDrTr}$ in S_{2EO} (Fig. S4). This could indicate that the parameter was difficult to constrain. The Grass C4 and Broad leaf deciduous trees PFTs were PFTs that were poorly represented in the soil carbon scheme grid cells. The GrassC4 PFT was in 77 % of the grid cells used in the optimization and had an average coverage of 5 % within those grid cells. The BdlDDrTr PFT was in 51 % of the optimization grid cells and had average coverage of 13 % within those grid cells. For comparison, the most represented PFT, BdlEvgTr, was in 92% of the optimization grid cells and occupied an average of 15 % of the grid cell area. The least represented PFT, NdlDcdTr, was in 35 % of the optimized grid cells and occupied an average of 6 % of the grid cell area.

While some of the parameter distributions overlapped between S_{2EO} and S_{2MO}, there was no consistent agreement in the best parameter values between the two runs (Table S1). The closest best parameter values between S_{2EO} and S_{2MO} were those of parameter $\chi_{NdlDcdTr}$, the least represented PFT, with a relative difference of 1 % between the optimized parameter values. The relative difference between the best parameter values of the two best optimization runs was on average 42 % with a maximum relative value of 90 % between optimized parameter values of the $\varsigma_{D,BdlDDrTr}$ parameter. This low agreement between

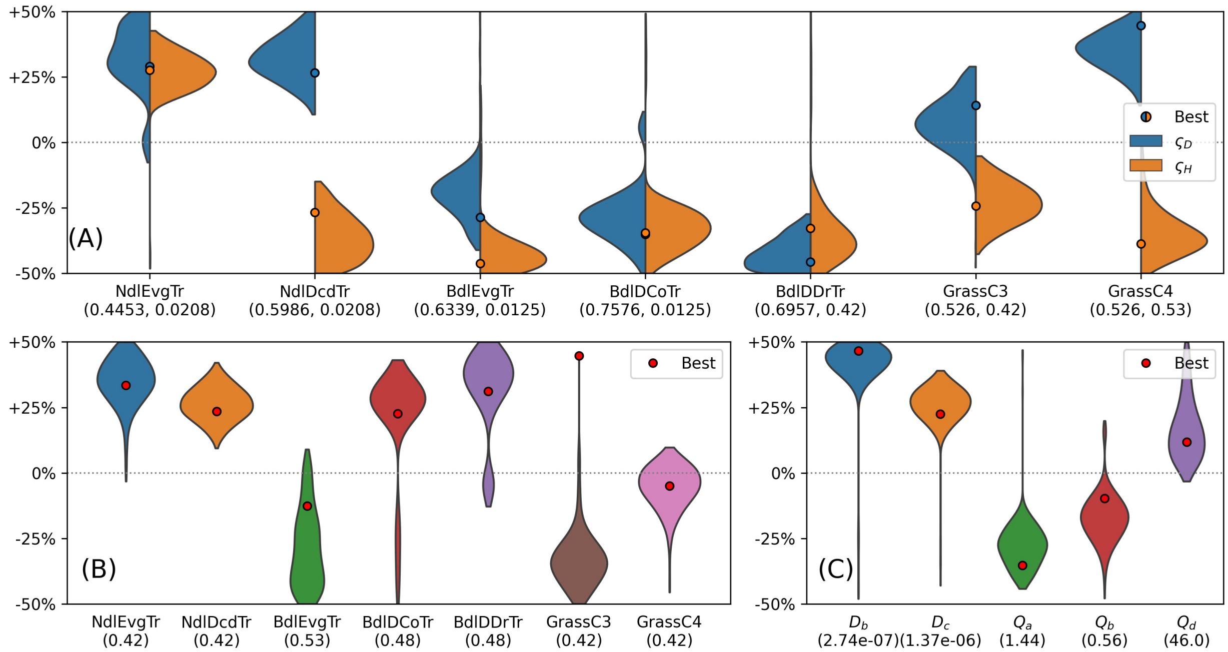

Fig. 2.5. Violin plots of the posterior parameter distributions for scenario S_2 and loss function L_{MO} obtained from 2000 optimization trials, using the first 1400 as burn-in. (A) Base respiration rate parameters for each of plant functional types (PFT) in CLASSIC; (ς_D in blue; ς_H in orange), (B) Humification transfer parameter χ. (C) Environmental parameters. The parameters are described in Table 2.1. For (A), (B) and (C), the marker in each distribution indicates the optimal parameter value (Table S1). For (A) and (B), CLASSIC PFTs are needleleaf evergreen trees (NdlEvgTr), needleleaf deciduous trees (NdlDcdTr), broadleaf evergreen trees (BdlEvgTr), broadleaf cold deciduous trees (BdlDCoTr), broadleaf drought/dry deciduous trees (BdlDDrTr), C_3 and C_4 grass (GrassC3, GrassC4). All distributions are normalized on a $\pm$ 50 % range around the initial value which is identified by the gray dashed line, the numbers in the parenthesis are the default parameter values (Table 2.1, Table S1). For (A), the numbers in the parenthesis are the default parameter values of ς_D and ς_H respectively.

the best values indicates that the choice of the loss function was highly influential to the optimization. Since the parameter sets S_{2MO} and S_{2EO} were selected by different loss functions, we could not identify which one was optimal solely based on their score. However, both parameter sets yielded low optimization scores in their respective loss function. Therefore to attempt to further distinguish between the two parameter sets, we used both of them to perform simulations with CLASSIC.

2.6.3. Identifying the Optimal Parameter Set

To find which loss function generated the optimal parameter set, we compared simulated SOC and R_{soil} by each optimized parameter set (S_{2MO} and S_{2EO}) to observation-based estimates. Both optimized parameter sets (S_{2EO} and S_{2MO}) and the default parameter set, (S_{DEF}), indicated consistent spatial biases across the three parameter sets compared to both reference data sets, NCSCD and GSWFE. All parameter set results showed a general underestimation of SOC content compared to NSCSD with some smaller regions, such as northwest Alaska, overestimated by CLASSIC (Fig. 2.6 (A)). For the R_{soil} comparisons, all parameter sets showed an overestimation in the south of the ABoVE domain (>49° N) and an underestimation in the north of the domain compared to GWSFE (Fig. 2.6 (B)). The differences between the three parameter sets were generally an order of magnitude lower than the differences with the observation-based data sets for SOC and R_{soil} (Fig. 2.6 (C-F)).

Table 2.3. Comparison metrics of the soil organic carbon (against NCSCD) and soil respiration simulations (against GWSFE). RMSD is the root mean square difference, which along bias is defined in section 2.5.8. A value in bold indicates that the parameter set has the best value out of the three parameter sets (lowest value for RMSD and lowest absolute value for bias). NCSCD comparison metrics used the simulated SOC over the 1950-2000 period. GWSFE comprison metrics used the simulated R_s over the 2003-2014 period.

	NCSCD			GWSFE		
	RMSD (kg C m^{-2})	Bias (kg C m^{-2})	Bias$_{rel}$	RMSD(kg C m^{-2}s^{-1})	Bias (kg C m^{-2}s^{-1})	Bias$_{rel}$
S_{2EO}	21.33	-17.36	-0.61	3.94e-9	8.32e-11	-0.11
S_{2MO}	**18.70**	**-14.28**	**-0.3990**	3.77e-9	**6.04e-11**	**-0.10**
S_{DEF}	19.05	-14.53	-0.3991	**3.37e-9**	-6.15e-10	-0.23

The similar patterns in spatial biases between the S_{2MO}, S_{2EO}, and S_{DEF} parameter sets despite their different parameter values likely indicates that the inputs coming from the rest of the CLASSIC model to the soil carbon scheme (e.g., carbon inputs and meteorological forcing), can have a greater influence on simulated SOC and R_{soil} than changes to parameter values themselves. Therefore, the consistent negative bias could indicate issues in the inputs to the soil carbon scheme. The meteorological forcing used to drive the model could have systematic biases as the high-latitude regions have relatively few observations that can be used to correct the meteorological forcing (Wu et al., 2017; Ahlström et al., 2017). Some of the underestimation of high-latitude SOC stocks and fluxes might be due to biases in the carbon inputs to the soil carbon scheme. CLASSIC's representation of vegetation dynamics as used here does not include vegetation types specific to northern ecosystems, such as shrubs or mosses, which are considered important to correctly capture ecosystem dynamics in these regions (Wullschleger et al., 2014). Productivity, i.e., the amount of carbon entering soils, and fractional coverage of PFTs in model grid cells of the simulations may not match observations, causing biases in these regions. Negative biases in high latitudes have been observed in the CLASSIC model before (Seiler et al., 2021). Underestimation of high-latitude SOC has also been reported in previous modeling efforts (Varney et al.,

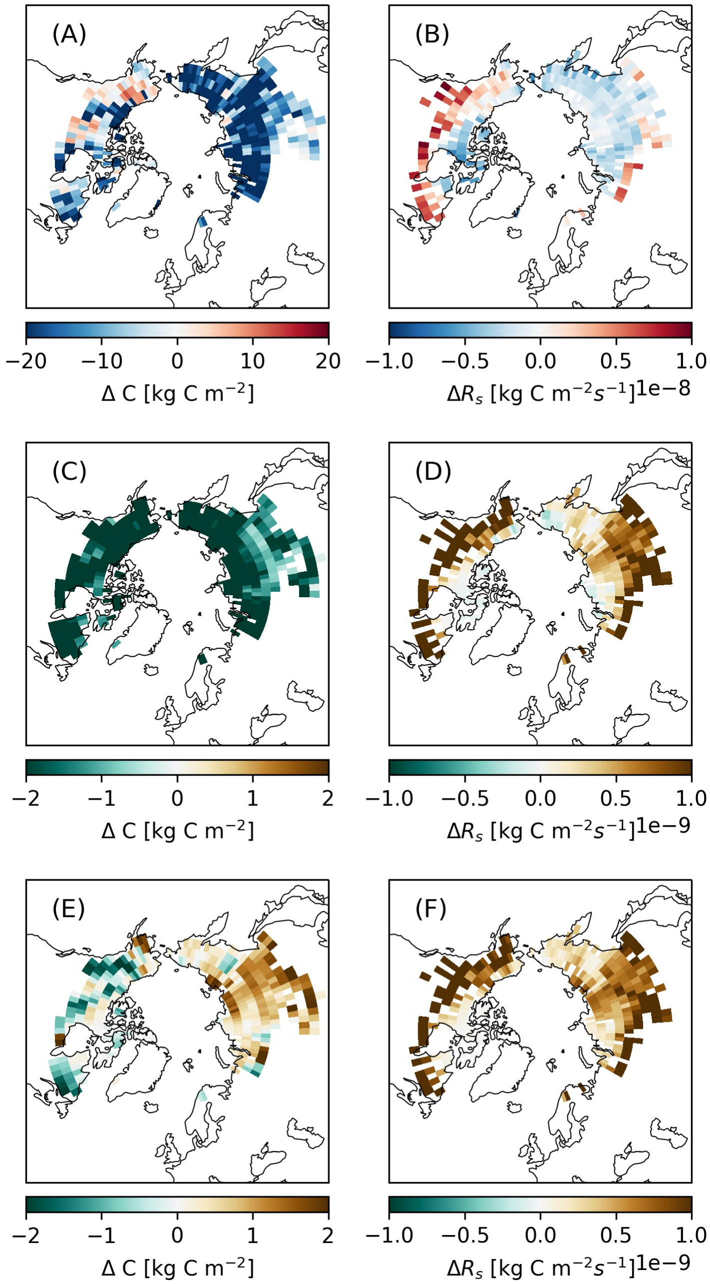

Fig. 2.6. (A) Difference between simulated soil organic carbon (SOC) with the CLASSIC default parameter set (S_{DEF}) and an observation-based reference data set from the Northern Circumpolar Soil Carbon Database (NCSCD) (Hugelius et al., 2013). (B) Difference between simulated soil respiration (R_{soil}) using S_{DEF} and the Gridded Winter Soil CO2 Flux Estimates for pan-Arctic and Boreal Regions, 2003-2100 from the Arctic-Boreal Vulnerability Experiment (GWSFE) (Watts et al., 2019). (C) Difference between simulated SOC using the S_{2EO} and S_{DEF} parameter sets. (D) Difference between simulated R_{soil} using S_{2EO} and S_{DEF} parameter sets. (E) Bias between simulated SOC using the S_{2MO} and S_{DEF} parameter sets. (F) Bias between simulated R_{soil} using the S_{2MO} and S_{DEF} parameter sets.

2022; Shi et al., 2018; Hararuk et al., 2014) and calls to improve the representation of permafrost-related processes in TBMs have been made (Schuur et al., 2015; Miner et al., 2022).

Despite the systemic biases compared to the observation-based reference datasets, the comparison metrics (Table 2.3) indicated that S_{2MO} had the lowest RMSD and the smallest bias of the parameter sets compared with NCSCD. It also had the smallest bias against GWSFE while S_{DEF} had the lowest RMSD (Table 2.3). S_{2EO} did not outperform S_{DEF} or S_{2MO} in any of the metrics across the NCSCD and GWSFE data sets (Table 2.3). The comparison metrics also reflected what is seen in the spatial comparison between the simulations and the data sets; the bias of all three parameter sets was uniformly negative when compared to NCSCD, reflecting the constant underestimation seen in the spatial distribution (Fig. 2.6 A, Table 2.3). For R_{soil}, the bias of the S_{DEF} parameter set was negative, while those of S_{2EO} and S_{2MO} were positive (Table 2.3) as can also be seen in Fig. 2.6 D, F.

While the NCSCD and GWSFE reference data sets can be used to evaluate the performance of the optimized parameter sets, these observation-based estimates should be considered cautiously. Both comparison data sets included observations within regions known to contain Yedoma deposits (Strauss et al., 2021). Yedoma is associated with high SOC concentrations and Yedoma formation processes are not represented by the CLASSIC mineral soil carbon scheme. Yedoma could have then contributed at least regionally (e.g., parts of Alaska and Siberia) to some of the underestimation of SOC and R_{soil} in high-latitude regions.

When compared to global SOC totals from empirical estimates and model ensembles (CMIP5 and CMIP6), all three parameter sets simulated high latitudes totals lower than estimates and model ensembles (Table 2.4). However, S_{2MO} simulated global SOC totals closer to empirical estimates (HWSD+NCSCD, WISE30sec, GSDE and KOCHY) than S_{2EO} and S_{DEF}, 1419 Pg C for S_{2MO} compared to 832 and 894 Pg C for S_{2EO} and S_{DEF} respectively (Table 2.4).

From the analysis of the parameter distributions, evaluation against the NCSCD and GWSFE observation-based estimates, and comparison with other literature estimates of global SOC totals, we found that the optimized parameter set S_{2MO} outperformed S_{2EO}. Furthermore, S_{2MO} outperformed S_{DEF} in almost all of the comparisons made with either independent observation-based estimates (NCSCD and GWSFE, Table 2.3) or literature estimates of global SOC totals (e.g., GSDE, WISE30sec and the combined HWSD+NCSCD,

Table 2.4. Comparison of global soil organic carbon totals simulated using the parameter sets S_{2EO}, S_{2MO} and S_{DEF} and other estimates including: the CMIP5 and CMIP6 model ensembles, the combined HWSD+NCSCD data set, WISE30sec, GSDE and KOCHY estimates. The high latitude total is the 60 - 90° N domain. All estimates are for the first meter of soil.

Source	Global SOC total (Pg C)	High latitude total (Pg C)	Reference
S_{2EO}	832	98	-
S_{2MO}	1419	155	-
S_{DEF}	894	151	-
CMIP6	1206 ± 445	266 ± 139	Varney et al. (2022)
CMIP5	1480 ± 810	318 ± 246	Varney et al. (2022)
HWSD + NCSCD	1412 ± 215	401 ± 83	Varney et al. (2022)
WISE30sec	1408 ± 154	-	Batjes (2016)
GSDE	1455	-	Shangguan et al. (2014)
KOCHY	1325	-	Köchy et al. (2015)

Table 2.4). S_{2MO}'s performance indicated that the optimization framework successfully improved the model simulation of SOC and R_{soil} fluxes. Of the two loss functions used, L_{MO} assigned better scores to parameter sets simulating SOC and R_{soil} closest to the observed values without consideration for the potential observational error. It may have been the case that our error-oriented loss function L_{EO} was too permissive, allowing good scores for estimates relatively far removed from the mean value. Our derived standard observational error of $\hat{\sigma}_T$ of roughly 80 % (Section 2.5.7) was much higher than what has been used by others when using the WoSIS data sets, e.g., 30 % (Tao et al., 2020). If the intervals given by the derived standard deviation $\hat{\sigma}_T$ of the WoSIS and SRDB data sets were too wide, then the optimization could have been too permissive, giving good scores to a large range of paraeter values and not well constraining the parameters. The large $\hat{\sigma}_T$ that we have estimated might have resulted from the large model grid cells. At a T63 resolution, the grid cells at the equator covered an area of 310 km x 310 km, likely increasing the derived observational error due to sub-grid heterogeneity (Fisher and Koven, 2020). We could potentially have decreased $\hat{\sigma}_T$ by increasing the horizontal model resolution. However, the coarse model resolution was needed to allow the computational cost to be reasonable given the many trials needed in the optimization.

2.6.4. Simulations of Future Soil Organic Carbon Dynamics

Since the S_{2MO} parameter set outperformed the other parameter sets, we assessed its impact on CLASSIC's simulation of SOC by comparing a future simulation against the default model parameter set. The future simulations were only made with the S_{2MO} and S_{DEF} parameter sets since our goal was to focus on the difference in model behavior caused by the optimized parameter set rather than project future SOC, which would require more than a single simulation to encapsulate CLASSIC's projections of future SOC. The S_{2MO} simulation had a global SOC total of 1,513 Pg C for the year 2100, an increase of 105 Pg C (7 %) compared to 2015. The S_{DEF} simulation estimated 936 Pg C, an increase of 50 Pg C (5 %) over the same period (Fig. 2.7). Both parameter sets projected that the global soil carbon stock would remain a net carbon sink over the next century. However, the spatial distribution of the change to the SOC pools indicated regional patterns such as losses of SOC from the major rainforests while the semi-arid regions accumulated SOC. Multiple regional losses of SOC were also identified in the high-latitudes (Fig. S7). While the default and optimized parameter sets simulated a similar change to the SOC pool over the 2015-2100 period, they simulated a different spatial distribution of the future SOC pool(Fig. 2.7). S_{2MO} simulated higher SOC content in tropical regions in 2100 than S_{DEF}, even as both parameter sets simulated carbon losses in these regions over the 2015-2100 period (Fig. S7). Simulated SOC content in high latitudes was generally similar between S_{2MO} and S_{DEF} with S_{2MO} simulating a 17 Pg C (10 %) increase between 2015 and 2100 and S_{DEF} simulating an 8 Pg C (5 %) increase over the same period. Overall, the optimized parameter set S_{2MO} simulated higher SOC stocks than S_{DEF} in both historical and future simulations. However, the simulated changes to SOC stocks over the 2015-2100 period by S_{2MO} were similar to those simulated by S_{DEF} (Fig. S7). This indicates that while the parameters of the soil carbon scheme do have an influence on simulated SOC and R_{soils}, the inputs to the scheme from the rest of the CLASSIC model still can override the soil carbon scheme for broader patterns, i.e., the similarity in simulated fluxes between S_{2MO} and S_{DEF} (Fig. S7). Furthermore, the sensitivity analysis and the optimization framework were designed to improve the simulation of the mean state of the soil carbon scheme, i.e, the size of the SOC stock and it's fluxes. In that sense, our study was not aimed at improving the simulation of the SOC pool to perturbations in climate. Parameters responsible for the mean state and those responsible for determining the mean state's response to perturbation are not necessarily the same, hence the default and optimized parameter sets producing similar changes to SOC stocks over the 2015-2100 period.

2.6.5. Limitations of the Study

The data sets used in the optimization framework (WoSIS and SRDB, section 2.5.6) had sparse data coverage in high-latitude regions, which are an important area for global SOC dynamics (Schuur et al., 2022; Canadell et al., 2021). Under-representation of those regions in our optimization could have led to poorly constrained high-latitude specific parameters and thereby contributed to an underestimation of high-latitude SOC stocks (Fig. 2.6). Other limitations of the optimization framework included the ± 50 % range used to define

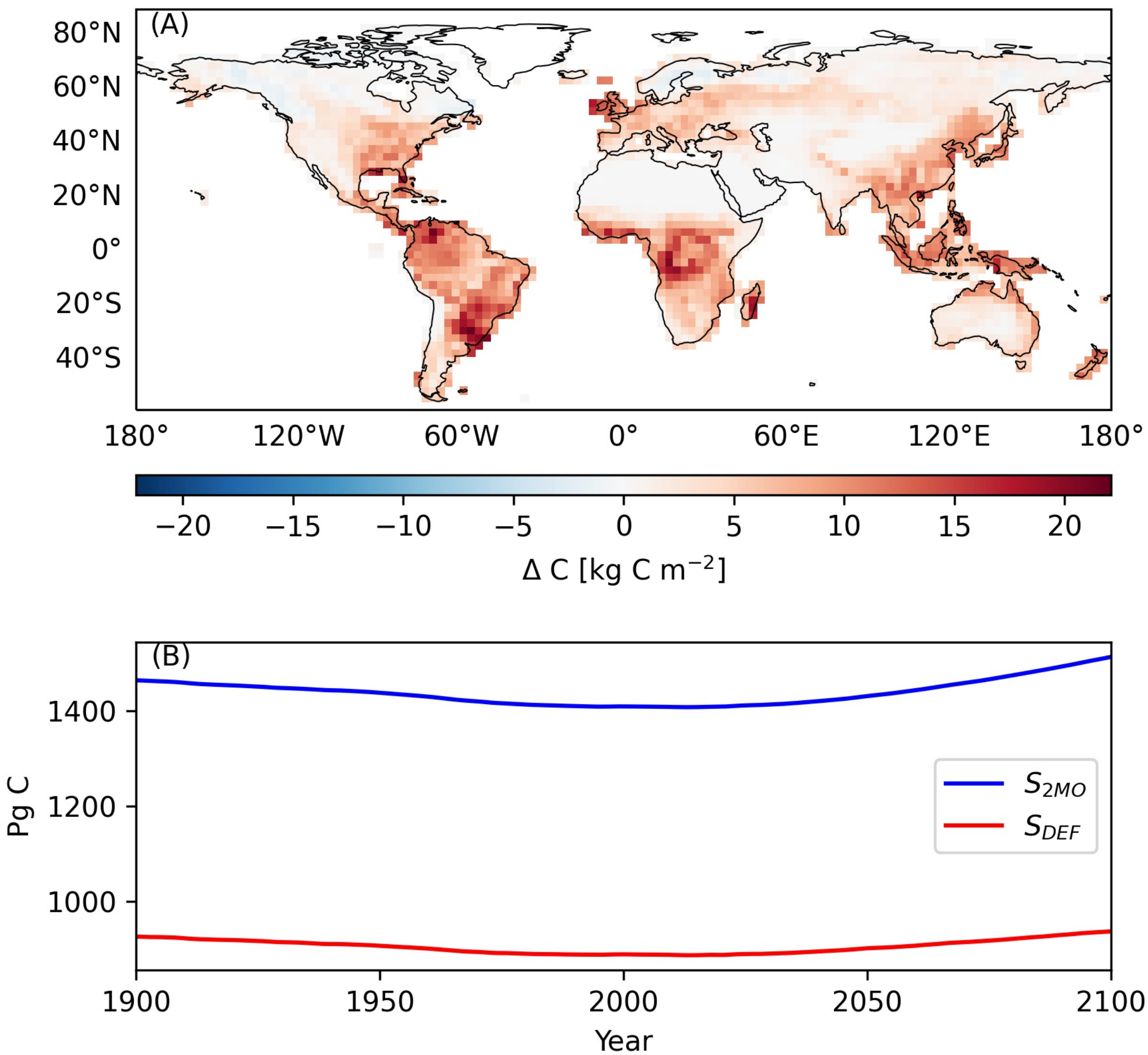

Fig. 2.7. (A) Difference in simulated 2100 SOC stock of the first meter of soil between the S_{DEF} and S_{2MO} parameter sets (S_{DEF} - S_{2MO}) in kg C m^{-2}. (B) Global total SOC of the first meter of soil, simulated over the 1900-2100 time period using the S_{2MO} (Blue) parameter set and the S_{DEF} (Red) parameter set.

the parameter search space, which we selected, in part, due to computational limitations. It is possible that for any given parameter, a more optimal value might have laid outside of the $\pm$ 50 % range. Also, we limited the optimization runs to 2000 trials. Although the best scores in each optimization run were unchanged for more than a quarter of the optimization at that limit, it is possible that longer optimization runs could have eventually led to better scores and, therefore, better-optimized parameters.

Another way of improving the parameter optimization and our results would have been to use more observational constraints. Isotopic carbon data shows great potential to additionally constrain SOC parameters (Koven et al., 2013; He et al., 2016; Shi et al., 2018). While SOC content observations constrained the size of the SOC pool, and R_{soil} observations constrained SOC fluxes, isotopic carbon data can constrain carbon residency time and the movement of carbon down the ground column. Isotopic carbon data can be used to identify sources of inputs to a soil carbon scheme (Singh et al., 2014), which can then improve the representation of carbon inputs to the soil in TBMs. Isotopic carbon data has also been used to constrain transfer parameters similar to the χ parameter in our soil carbon scheme (He et al., 2016; Feng et al., 2016), which was identified as one the parameters that contributed the most to the variance of simulated SOC and R_{soil} by the sensitivity analysis (Section 2.6.1.

Other limitations could have come from how we used site-level observations to determine the performance of the optimization. We used site-level observational data in the optimization to avoid the ambiguity of gridded products with no uncertainty bound and their own associated biases. Upscaling site-level data to the spatial scale of a global model grid cell was challenging due to errors induced by the upscaling scheme (Shi et al., 2018). To convert from point-scale observations to the level of a grid cell, as was needed to compare to the model simulations, all observations within a grid cell were simply averaged, effectively disregarding sub-grid heterogeneity, which is important nonetheless (Fisher and Koven, 2020). However, by using the EO loss function, we did try to account for observationnal error. We could have reduced the grid cell sizes to minimize the influence of the averaging required, but that would have severely limited the number of trials we could perform in the optimizations due to increased computational cost.

2.7. Conclusion

This study aimed to optimize the parameters of the soil carbon scheme of CLASSIC with a Bayesian optimization framework to improve CLASSIC's representation of SOC dynamics. Using a sensitivity analysis, our study revealed that parameter sensitivity depended on the variable investigated (SOC and R_{hetr}) and climatic conditions at the site where we performed the analysis. We also found that the loss function used in the optimization framework impacted what parameter values were chosen as optimal. We observed through the consistent biases in our comparison with observation-based estimates that the model inputs to the soil carbon scheme can have more impact than the optimized parameters on simulated SOC and

R_{soil}, as shown by the default and optimized simulations having similar spatial biases against observation-based estimates and similar future simulations of SOC. We identified that more constraints on the soil carbon scheme, such as isotopic data, are likely needed to adequately overcome equifinality and better constrain parameters. Additional uncertainty generated by the up-scaling of site-level observations to global gridded model resolution was also difficult to avoid without the loss of information on the point scale data. Still, we generated an optimized parameter set that simulated SOC dynamics closer to measurments of SOC and R_{soil}, high-latitude specific datasets, as well as global literature estimates while also having a better optimization score than the default parameter set, indicating the selected optimized parameter set improved CLASSIC's representation of SOC dynamics.

S1. Soil Carbon Scheme Equilibrium

For every optimization trial, the soil carbon scheme was run globally, cycling on reanalysis climate data from 1900 to 1920 until equilibrium was reached. We checked for equilibrium every 20 years. We first calculated the total SOC mass, summed over all soil layers, contained in the humified pool as this pool took longest to stabilize and was, therefore, a good indication of the state of the model. We then compared the present pool size with the value from the last loop. Once the change in the humified pool size between two loops fell under 0.05 %, we considered the model to be at equilibrium.

S2. Temperature parameter influence on the temperature function

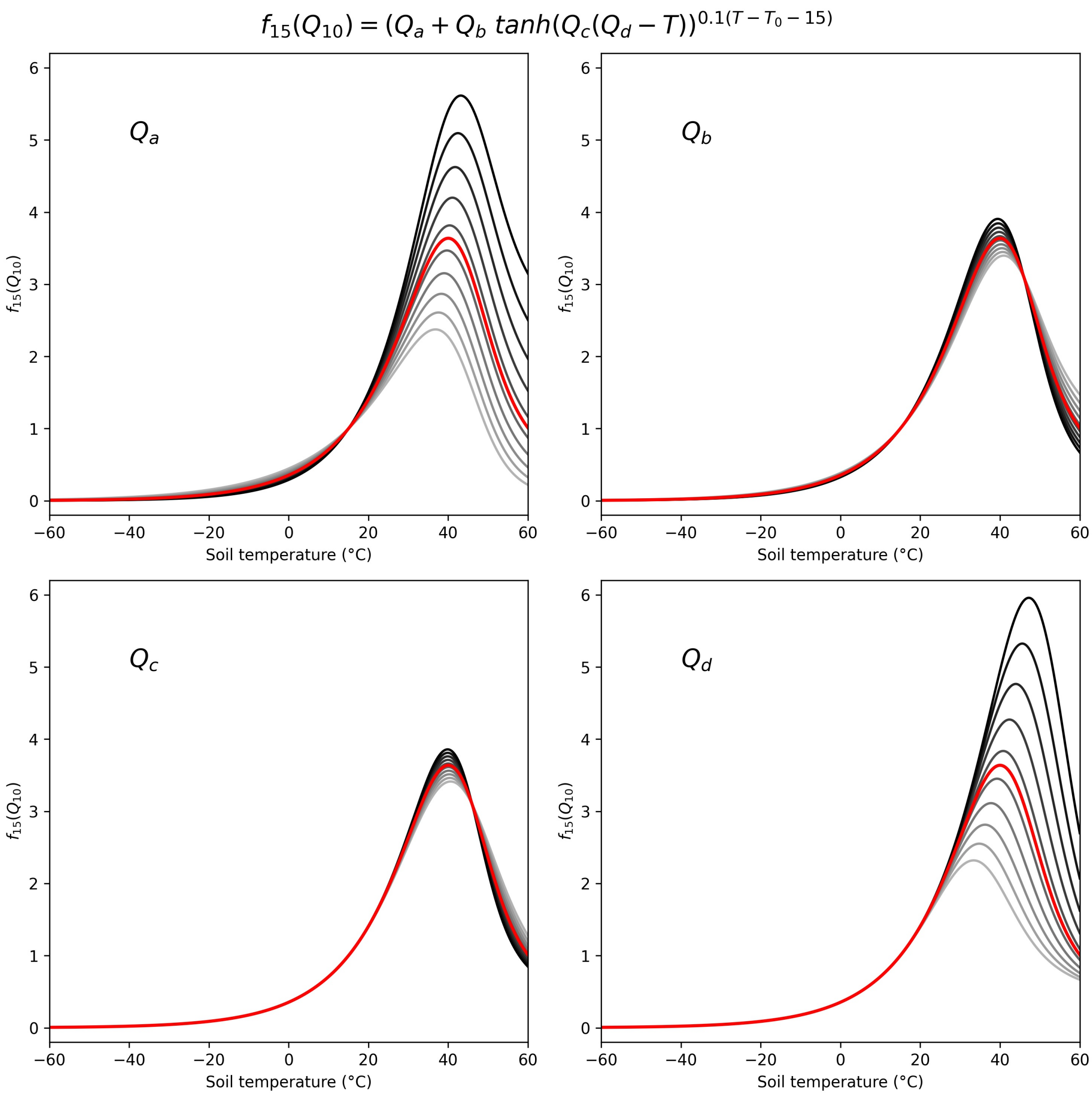

Fig. S1. Impact of temperature parameter variation on the $f_{15}(Q_{10})$ function. In each subfigure, 3 of the four parameters are fixed while the remaining one varies on an interval of [-20 %, 20 %] of its default value. This interval is reflected by the curve color following the [-20 %,20 %] values from light to dark. The parameter that varies is identified in the top-left corner of each subfigure. The red curve indicates the default configuration of the $f_{15}(Q_{10})$ function.

S3. Convergence of the sensitivity analysis

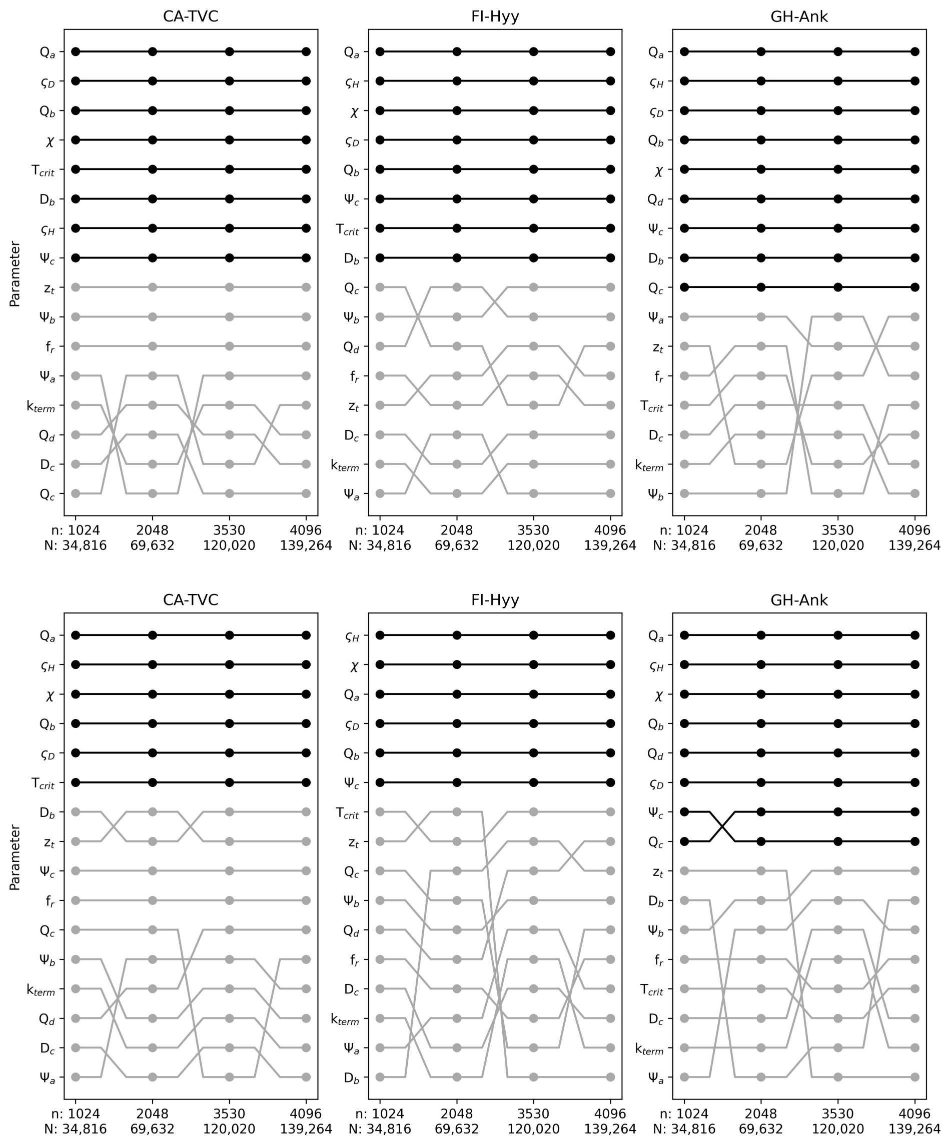

Fig. S2. Convergence of Sobol' 1^{st} order index for simulated SOC (top row) and simulated R_{hetr} (bottom row) for different number of simulations, n and experiment N (Section 2.5.4, at each of the three eddy covariance tower sites (Section 2.6.1, Table 2.2). The position of the parameter along the Y-axis indicates its ranking in sensitivity with the most sensitive being listed at the top of the diagram. A light gray color indicates an insensitive parameter according to the criteria detailed in Section 2.6.1

S4. Loss functions and scores

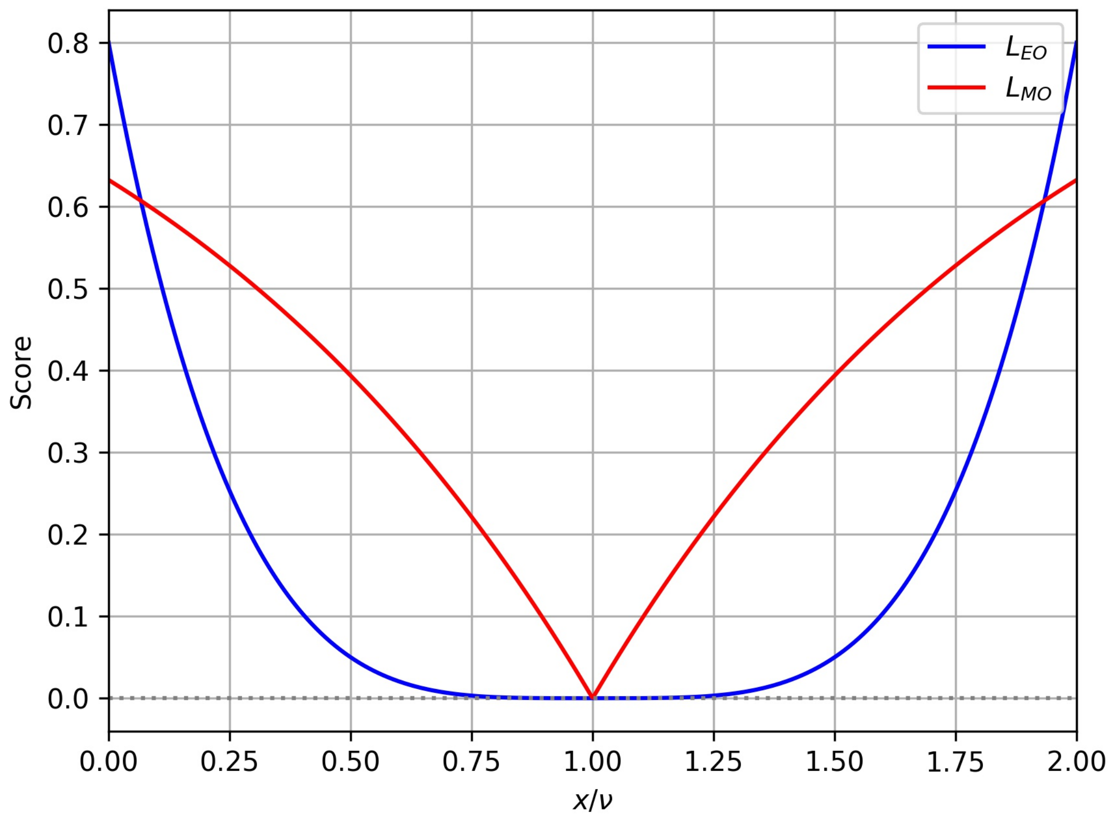

Fig. S3. Score yielded by the loss functions, L_{EO} in blue, L_{MO} in red, in relation to the simulated value x normalized by the observed value ν. A value of 1 on the x-axis indicates that the simulated value is equal to the observed value. Smaller scores are better.

S5. Posterior Parameter Distributions

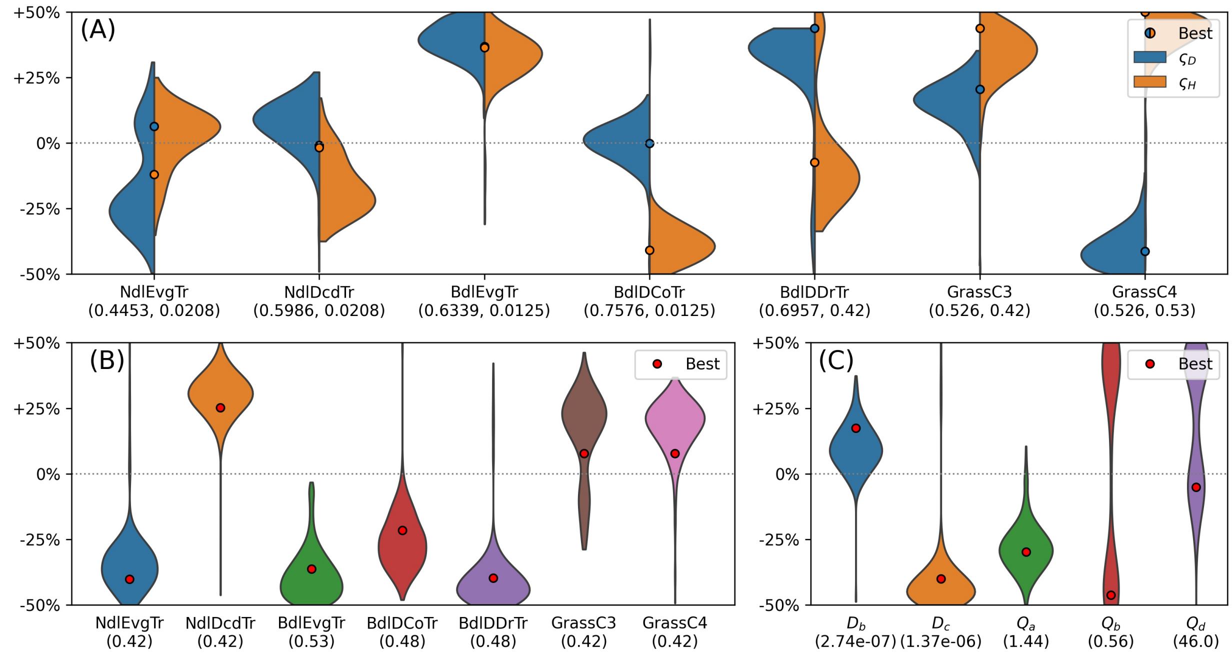

Fig. S4. Violin plots of the posterior parameter distributions for scenario S_2 and loss function L_{EO} obtained from 2000 optimization trials, using the first 1400 as burn-in. (A) Base respiration rate parameters for each of plant functional types (PFT) in CLASSIC; (ς_D in blue; ς_H in orange), (B) Humification transfer parameter χ. (C) Environmental parameters. The parameters are described in Table 2.1. For (A), (B) and (C), the marker in each distribution indicates the optimal parameter value (Table S1). For (A) and (B), CLASSIC PFTs are needleleaf evergreen trees (NdlEvgTr), needleleaf deciduous trees (NdlDcdTr), broadleaf evergreen trees (BdlEvgTr), broadleaf cold deciduous trees (BdlDCoTr), broadleaf drought/dry deciduous trees (BdlDDrTr), C_3 and C_4 grass (GrassC3, GrassC4). All distributions are normalized on a $\pm$ 50 % range around the initial value which is identified by the gray dashed line, the numbers in the parenthesis are the default parameter values (Table 2.1, Table S1). For parameters $\varsigma_{D,BdlDDrTr}$, its higher bound was set to 1 to avoid non-physical representation of respiration rates, corresponding to a value of +44 % of their default value. For (A), the numbers in the parenthesis are the default parameter values of ς_D and ς_H respectively.

S6. Optimized Parameter Values

Table S1. Optimized and default parameter values of the parameters from the S_{2EO}, S_{2MO} and S_{DEF} parameter sets. For description of parameters, see Table 2.1

Name	PFT	S_{2EO}	S_{2MO}	S_{DEF}
ς_D	NdlEvgTr	0.4732	0.5747	0.4453
	NdlDcdTr	0.5930	0.7576	0.5986
	BdEvgTr	0.8668	0.4525	0.6339
	BdlDCoTr	0.7563	0.4918	0.7576
	BdlDDrTr	0.9994	0.3776	0.6957
	GrassC3	0.6335	0.6001	0.5260
	GrassC4	0.3087	0.7604	0.5260
ς_H	NdlEvgTr	0.0299	0.0331	0.0260
	NdlDcdTr	0.0256	0.0191	0.0260
	BdEvgTr	0.0284	0.0112	0.0208
	BdlDCoTr	0.0123	0.0136	0.0208
	BdlDDrTr	0.0193	0.0140	0.0208
	GrassC3	0.0180	0.0095	0.0125
	GrassC4	0.0187	0.0077	0.0125
χ	NdlEvgTr	0.25	0.56	0.42
	NdlDcdTr	0.53	0.52	0.42
	BdlEvgTr	0.34	0.46	0.53
	BdlDCoTr	0.38	0.59	0.48
	BdlDDrTr	0.29	0.63	0.48
	GrassC3	0.45	0.61	0.10
	GrassC4	0.45	0.40	0.10
D_b	-	3.21802e-7	4.01792e-7	2.73972e-7
D_c	-	0.82204e-6	1.67724e-6	1.36986e-6
Q_a	-	1.01	0.93	1.44
Q_b	-	0.30	0.51	0.56
Q_d	-	43.7	51.4	46.0

S7. Search History

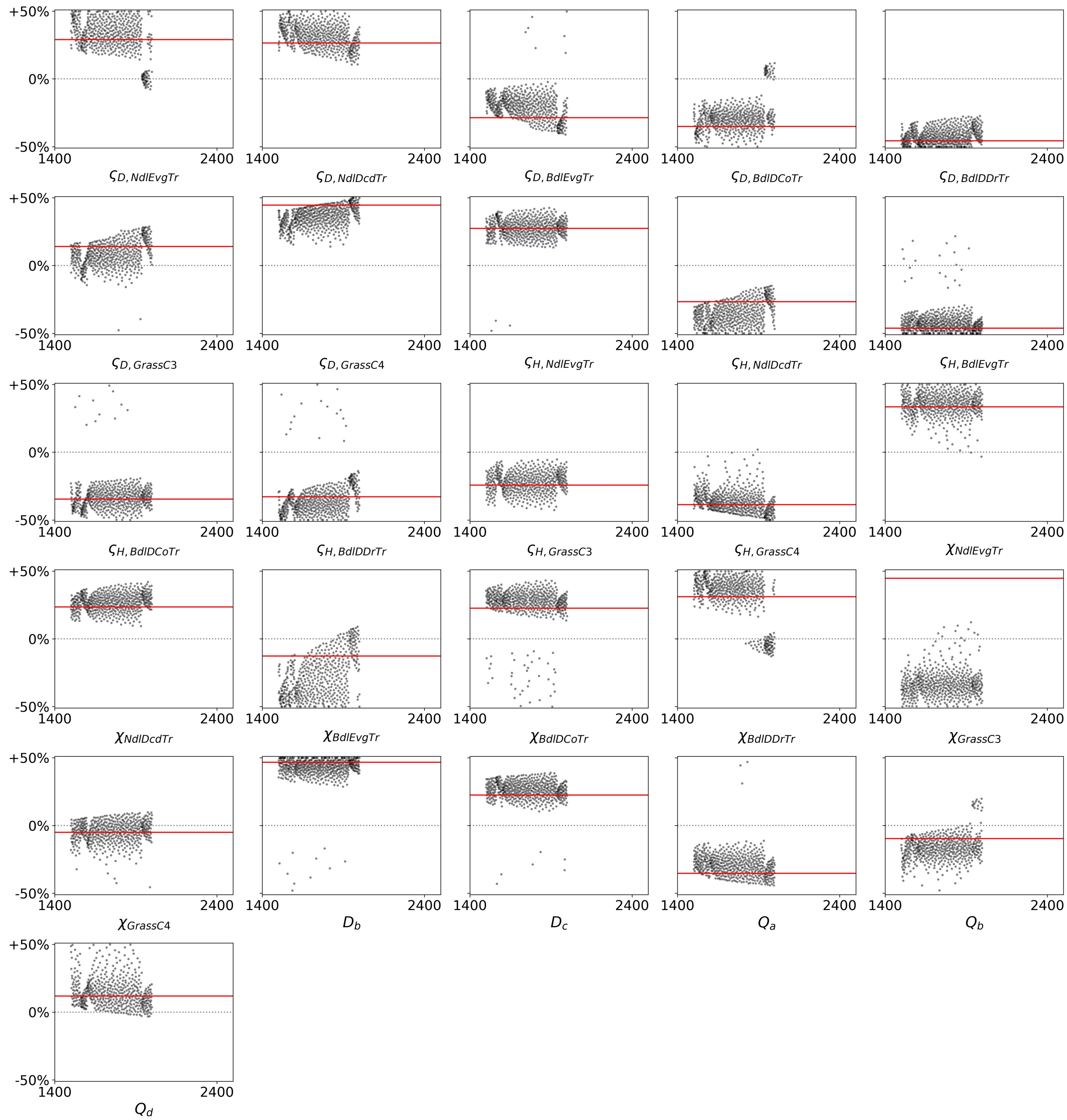

Fig. S5. Search history of the S_{2MO} optimization during the last 600 optimization steps (x-axis) used to generate the posterior parameter distributions. The red line indicates the parameter value that yielded the best score (Table S1). The gray dashed line indicates the initial parameter value. Each subplots shows the search history of the parameter indicated below. Every marker in the figure corresponds to a parameter value used by the algorithm of the Bayesian optimization framework (Section 2.5.5) during the optimization trial.

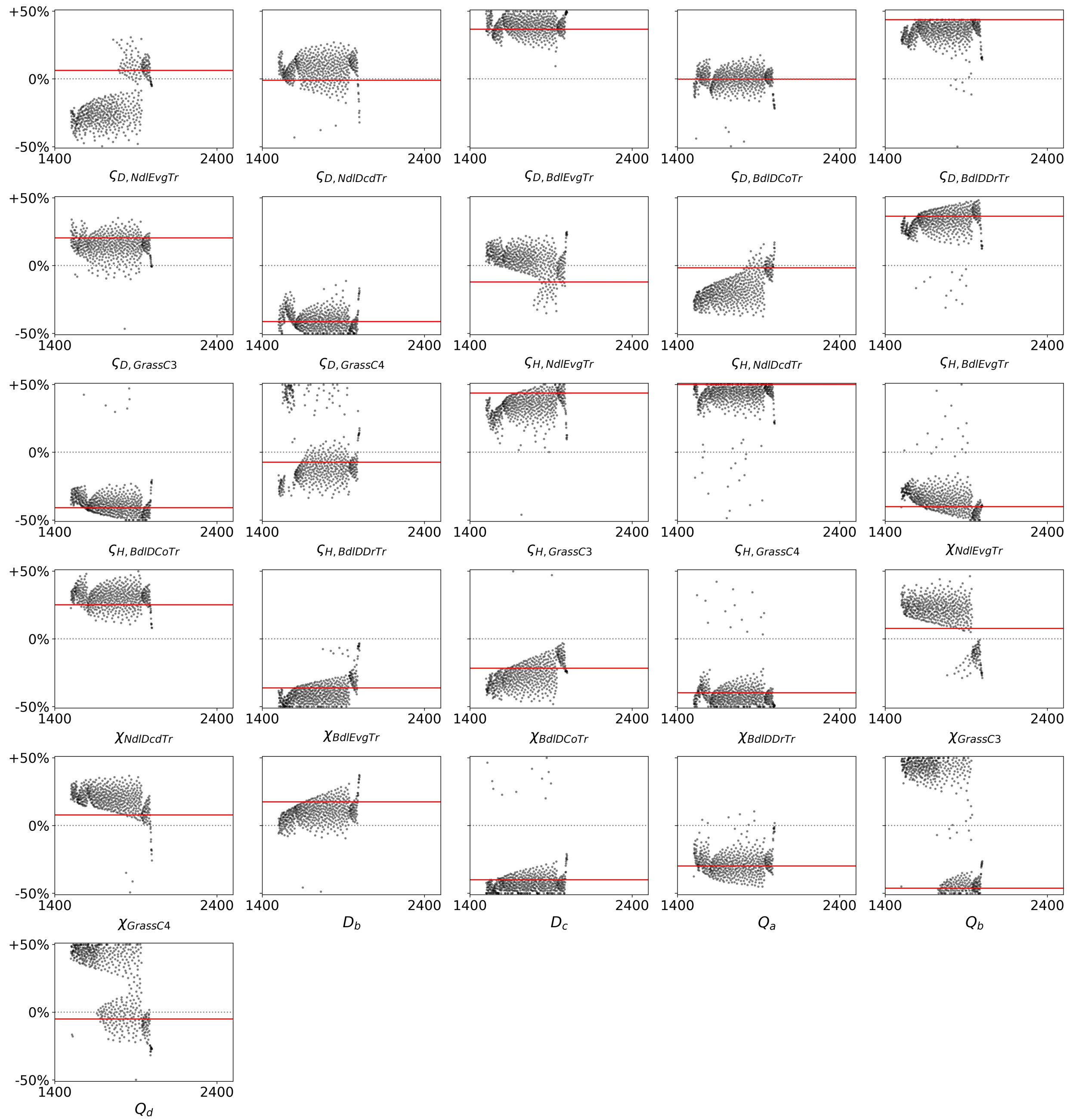

Fig. S6. Search history of the S_{2EO} optimization during the last 600 optimization steps (x-axis) used to generate the posterior parameter distributions. The red line indicates the parameter value that yielded the best score (Table S1). The gray dashed line indicates the initial parameter value. Each subplots shows the search history of the parameter indicated below. Every marker in the figure corresponds to a parameter value used by the algorithm of the Bayesian optimization framework (Section 2.5.5) during the optimization trial.

S8. Spatial Distribution of Future SOC Change

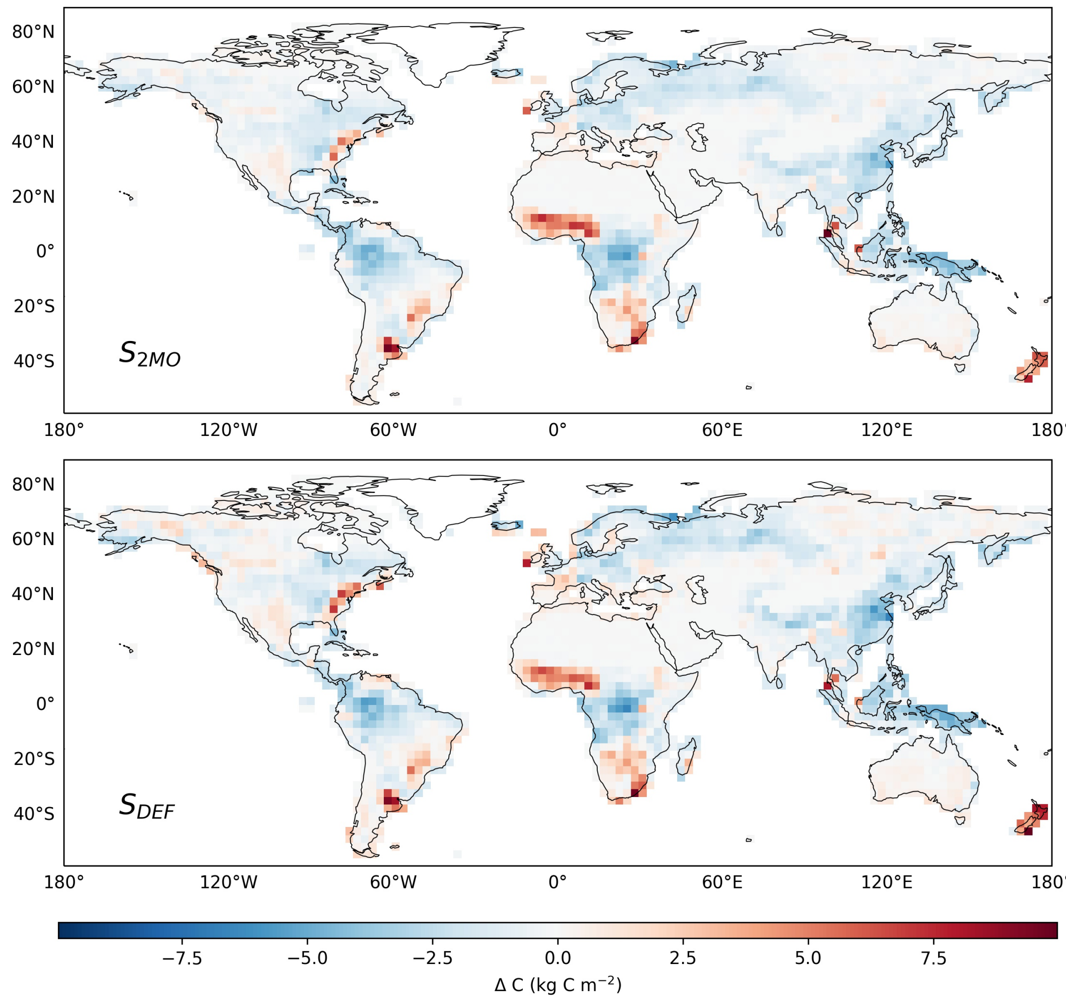

Fig. S7. Spatial difference between 2015 and 2100 SOC stocks of the first meter of soil in kg C m^{-2}, simulated by the S_{2MO} (Top) and S_{DEF} (Bottom) parameter sets. Red indicates an increase of SOC between 2015 and 2100 and blue indicates a decrease.

Chapitre 3

Conclusion

Dans cette étude, les paramètres du schéma de carbone de sol de CLASSIC ont été optimisés. Tout d'abord, la contribution des paramètres à la variance du SOC et de la R_{sol} simulés par le schéma de carbone de sol a été identifiée à l'aide d'une analyse de sensibilité Sobol' qui a révélé que la sensibilité des paramètres était contextuelle et dépendait des différents climats simulés et variables climatiques simulées (SOC et R_{soil}), c'est-à-dire la teneur en carbone organique du sol et la respiration hétérotrophe du sol. L'analyse de sensibilité a également montré que certains paramètres du schéma de carbone de sol ne contribuaient pas à la variance du SOC et de la R_{hetr} simulés.

Ensuite, sur la base des résultats de l'analyse de sensibilité, quatre scénarios d'optimisation ont été utilisés pour optimiser les paramètres du schéma de carbone du sol. Pour chaque scénario, deux fonctions coût ont été utilisées pour optimiser les paramètres, ce qui a donné lieu à huit séquences d'optimisation. Les résultats de l'optimisation ont montré que le choix de la fonction coût utilisée affectait les valeurs de paramètres optimisées qui étaient considérées optimales. Les paramètres optimisés de la meilleure séquence d'optimisation de chaque fonction coût ont ensuite été identifiés et utilisés dans le modèle CLASSIC pour faire des simulations historiques et futures du SOC et de la R_{sol}. Les valeurs simulées du SOC et de la R_{sol} obtenues des simulations historiques ont été comparées à une simulation par défaut (S_{DEF}), utilisant les valeurs par défaut des paramètres contenus dans CLASSIC. Les deux ensembles de paramètres optimisés (S_{2EO} et S_{2MO}) et S_{DEF} du modèle CLASSIC ont ensuite été comparés à deux ensembles de données basés sur des observations (NCSCD et GWSFE). Une sous-estimation générale de la quantité de SOC en hautes latitudes par rapport aux ensembles de données NCSCD et GWSFE a été constatée. Cette sous-estimation indiquait que les intrants du schéma de carbone de sol semblent avoir une influence plus importante que les paramètres eux-mêmes sur la simulation des dynamiques du SOC, puisque les mêmes biais ont été observés tant pour S_{DEF} que pour les ensembles de paramètres optimisés. Les simulations historiques réalisées avec les paramètres optimisés ont également été utilisées pour calculer et comparer les totaux mondiaux de SOC aux estimations existantes dans la littérature. Une sous-estimation des hautes latitudes a de nouveau été constatée.

Des deux ensembles de paramètres optimisés, les totaux globaux simulés par l'ensemble de paramètres S_{2MO} étaient plus proches des estimations trouvées dans la littérature. Également, la quantité globale de SOC issue de S_{2MO} étaient plus proches des estimations que la quantité globale simulée par S_{DEF} , ce qui indique que l'optimisation a permis de générer un ensemble de paramètres permettant des simulations plus proches des estimations empiriques. Les simulations futures ont ensuite été utilisées pour évaluer l'impact de l'ensemble de paramètres optimisés S_{2MO} sur les prédictions de CLASSIC. Il a été constaté que S_{2MO} et S_{DEF} prévoyaient que le réservoir de SOC global demeurerait un puits de carbone net au cours du 21e siècle. Bien que la taille du réservoir de SOC simulé par les deux ensembles de paramètres (S_{2MO} et S_{DEF}) ait été différente, les deux ensembles de paramètres ont prédit une augmentation similaire du SOC par rapport à la taille initiale du réservoir en 2015. L'ensemble de paramètres optimisés a simulé plus de SOC dans les régions tropicales, tandis que les régions de hautes latitudes étaient similaires aux simulations réalisées avec S_{DEF}.

Bien que l'ensemble de paramètres optimisés S_{2MO} soit plus performant que S_{DEF} et qu'il soit donc susceptible d'améliorer les prévisions du modèle CLASSIC, notre étude présente certaines limitations qui méritent d'être énoncées. Tout d'abord, les ensembles de données utilisés dans la structure d'optimisation (WoSIS et SRDB, section 2.5.6) avaient une couverture spatiale éparse dans les régions de hautes latitudes, qui sont néanmoins une zone importante pour la dynamique globale du SOC (Schuur et al., 2022; Canadell et al., 2021). La sous-représentation de ces régions dans notre optimisation aurait pu conduire à des paramètres spécifiques aux hautes latitudes à être moins bien optimisés et contribuer ainsi à une sous-estimation des stocks de SOC en hautes latitudes, telle qu'observée lors de la comparaison avec des estimations empiriques. Une autre limite de la structure d'optimisation est l'intervalle de ± 50 % utilisé pour définir l'espace de recherche des paramètres. Cet intervalle a été choisi, en partie, en raison de limites computationnelles. Il est cependant possible que pour un paramètre donné, une valeur plus optimale ait été en dehors de l'intervalle de 50 %. Nous avons également limité les séquences d'optimisation à 2000 itérations. Bien que les meilleurs scores de chaque séquence d'optimisation soient restés inchangés pendant plus d'un quart de l'optimisation à cette limite, il est possible que des séquences d'optimisation plus longues aient mené à de meilleurs scores et, par conséquent, à des paramètres plus optimisés.

Une autre façon d'améliorer l'optimisation des paramètres et nos résultats aurait été d'utiliser davantage de contraintes sur les paramètres. Des données d'isotopes de carbone contenu dans le sol présentent un grand potentiel pour contraindre davantage les paramètres du SOC (Koven et al., 2013; He et al., 2016; Shi et al., 2018). Alors que les observations de la quantité de SOC contenue dans les sols offrent une contrainte sur la taille du réservoir de SOC et sur sa distribution en profondeur et que les observations de R_{sol} offrent une contrainte sur les flux du réservoir de SOC, les données d'isotopes de carbone offrent une contrainte sur le temps de résidence du carbone et sur le mouvement du carbone vers le bas de la colonne de sol. Les données d'isotopes de carbone peuvent être utilisées pour identifier les sources d'intrants à un schéma de carbone de sol, c'est-à-dire, d'où vient le carbone qui entre dans les sols (Singh et al., 2014). Cette capacité à identifier les sources de carbone peut ensuite améliorer la représentation des dynamiques du SOC dans les TBMs. Les données d'isotopes de carbone ont également été utilisées pour contraindre des paramètres de transfert similaires au paramètre χ dans notre schéma de carbone de sol (He et al., 2016; Feng et al., 2016). Comme le paramètre de transfert χ a été identifié comme l'un des paramètres ayant le plus contribué à la variance du SOC et du R_{sol} simulés par l'analyse de sensibilité, de meilleures contraintes sur ce paramètre auraient potentiellement un grand impact sur le succès de l'optimisation. Ainsi, les données d'isotopes de carbone offrent une avenue potentielle pour améliorer les résultats présentés dans cette étude.

D'autres limitations auraient pu provenir de la manière dont nous avons utilisé les observations de terrain pour évaluer la performance de l'optimisation. Nous avons utilisé des données d'observation de terrain dans l'optimisation afin d'éviter l'ambiguïté des produits de données sur grille qui ne comportent pas de limites d'incertitude et qui ont leurs propres biais. Cependant, le changement d'échelle entre des données de terrains et la grille d'un modèle globale, telle la résolution T63, utilisées par CLASSIC dans cette étude, peut également s'avérer difficile en raison des erreurs induites par la procédure de changement d'échelle (Shi et al., 2018). Pour convertir les observations ponctuelles vers la résolution de la grille globale de CLASSIC, nous avons calculé la moyenne de toutes les observations à l'intérieur d'une cellule de la grille globale, sans tenir compte de l'hétérogénéité de la cellule, qui est néanmoins importante (Fisher and Koven, 2020). Il aurait été possible de réduire la taille des cellules de la grille pour minimiser l'influence de la procédure de changement d'échelle, mais cela aurait fortement limité le nombre possible d'itérations d'optimisation en raison de l'augmentation des coûts calculatoire.

Malgré les limitations qui ont été rencontrées, cette recherche a permis de mettre en lumière plusieurs points clés de l'optimisation des paramètres d'un schéma de carbone de sol, qui ont des implications pour de futures études. Tout d'abord, la sensibilité des paramètres qui s'est avéré dépendante des conditions environnementales du site et des variables qui sont simulées est importante puisqu'elle montre l'importance d'inclure la totalité du domaine de conditions climatiques du modèle avec lequel est effectuée l'analyse de sensibilité. Autrement, certains paramètres pourraient apparaître insensibles et être retirés d'une optimisation alors qu'ils contribuent à la variation des variables simulées sous certaines conditions climatiques. Ensuite, l'analyse de sensibilité a également révélé que certains paramètres ne contribuaient pas à la variance des variables climatiques simulées. Cette particularité est importante puisqu'elle montre qu'une analyse de sensibilité préalable à une optimisation permet de retirer certains paramètres et donc de réduire la dimensionnalité de l'espace des paramètres. Ainsi, pour un même coût computationnel, l'optimisation devient plus efficace, ce qui peut mener à de meilleurs résultats.

L'optimisation des paramètres a également révélé que la fonction coût choisie influence quels paramètres seront considérés comme optimaux. Ce résultat soulève d'importantes questions méthodologiques puisque peu de considération est généralement accordée à la sélection de la fonction coût lors de l'élaboration d'une routine d'optimisation. Ensuite, l'étude a démontré que les intrants du schéma de carbone de sol, c'est-à-dire, la quantité entrante de carbone et la météorologie fournie par le reste du modèle CLASSIC semblent avoir une plus grande influence sur les variables climatiques simulées qu'un changement des valeurs de paramètres. Ce résultat, démontré par des biais spatiaux similaires tant pour les ensembles de paramètres optimisés que pour S_{DEF} lors de la comparaison avec l'ensemble de données NCSCD, a des implications importantes pour l'amélioration future des TBMs. Il indique qu'en plus de l'optimisation des paramètres de carbone de sol, une amélioration des autres composantes du modèle est potentiellement requise afin de fournir une meilleure représentation des dynamiques du carbone de sol.

Tout de même, la structure d'optimisation utilisée dans cette étude a produit un ensemble de paramètres qui généraient des valeurs de SOC et de R_{sol} qui étaient plus semblables aux estimés empiriques que l'ensemble de paramètres par défaut, indiquant une amélioration de la représentation des dynamiques du carbone de sol dans le modèle CLASSIC. Ainsi, les résultats découlant de l'étude fournissent à la communauté de modélisation des écosystèmes terrestres un outil plus précis pour simuler les dynamiques du réservoir de carbone de sol et comment celui-ci affectera le cycle du carbone global dans un contexte d'accélération des changements climatiques

Références bibliographiques

Ahlström, A., Schurgers, G., and Smith, B. (2017). The large influence of climate model bias on terrestrial carbon cycle simulations. *Environ. Res. Lett.*, 12(1):014004.

Amelung, W., Bossio, D., de Vries, W., Kögel-Knabner, I., Lehmann, J., Amundson, R., Bol, R., Collins, C., Lal, R., Leifeld, J., Minasny, B., Pan, G., Paustian, K., Rumpel, C., Sanderman, J., van Groenigen, J. W., Mooney, S., van Wesemael, B., Wander, M., and Chabbi, A. (2020). Towards a global-scale soil climate mitigation strategy. *Nat. Commun.*, 11(1):5427.

Arora, V. K. (2003). Simulating energy and carbon fluxes over winter wheat using coupled land surface and terrestrial ecosystem models. *Agric. For. Meteorol.*, 118(1):21–47.

Arora, V. K. and Boer, G. J. (2003). A representation of variable root distribution in dynamic vegetation models. *Earth Interact.*, 7(6):1–19.

Baldocchi, D. D. (2003). Assessing the eddy covariance technique for evaluating carbon dioxide exchange rates of ecosystems: past, present and future. *Glob. Chang. Biol.*, 9(4):479–492.

Batjes, N. H. (2016). Harmonized soil property values for broad-scale modelling (WISE30sec) with estimates of global soil carbon stocks. *Geoderma*, 269:61–68.

Batjes, N. H., Ribeiro, E., and van Oostrum, A. (2020). Standardised soil profile data to support global mapping and modelling (WoSIS snapshot 2019). *Earth Syst. Sci. Data*, 12(1):299–320.

Behrenfeld, M. J., O'Malley, R. T., Siegel, D. A., McClain, C. R., Sarmiento, J. L., Feldman, G. C., Milligan, A. J., Falkowski, P. G., Letelier, R. M., and Boss, E. S. (2006). Climate-driven trends in contemporary ocean productivity. *Nature*, 444(7120):752–755.

Bergstra, J., Bardenet, R., Bengio, Y., and Kégl, B. (2011). Algorithms for hyper-parameter optimization. In *25th annual conference on neural information processing systems (NIPS 2011)*, volume 24. hal.inria.fr.

Bergstra, J., Yamins, D., and Cox, D. (2013). Making a science of model search: Hyper-parameter optimization in hundreds of dimensions for vision architectures. In Dasgupta, S. and McAllester, D., editors, *Proceedings of the 30th International Conference on Machine Learning*, volume 28 of *Proceedings of Machine Learning Research*, pages 115–123, Atlanta, Georgia, USA. PMLR.

Berner, R. A. (2003). The long-term carbon cycle, fossil fuels and atmospheric composition. *Nature*, 426(6964):323–326.

Biskaborn, B. K., Smith, S. L., Noetzli, J., Matthes, H., Vieira, G., Streletskiy, D. A., Schoeneich, P., Romanovsky, V. E., Lewkowicz, A. G., Abramov, A., Allard, M., Boike, J., Cable, W. L., Christiansen, H. H., Delaloye, R., Diekmann, B., Drozdov, D., Etzelmüller, B., Grosse, G., Guglielmin, M., Ingeman-Nielsen, T., Isaksen, K., Ishikawa, M., Johansson, M., Johannsson, H., Joo, A., Kaverin, D., Kholodov, A., Konstantinov, P., Kröger, T., Lambiel, C., Lanckman, J.-P., Luo, D., Malkova, G., Meiklejohn, I., Moskalenko, N., Oliva, M., Phillips, M., Ramos, M., Sannel, A. B. K., Sergeev, D., Seybold, C., Skryabin, P., Vasiliev, A., Wu, Q., Yoshikawa, K., Zheleznyak, M., and Lantuit, H. (2019). Permafrost is warming at a global scale. *Nat. Commun.*, 10(1):264.

Blyth, E. M., Arora, V. K., Clark, D. B., Dadson, S. J., De Kauwe, M. G., Lawrence, D. M., Melton, J. R., Pongratz, J., Turton, R. H., Yoshimura, K., and Yuan, H. (2021). Advances in land surface modelling. *Current Climate Change Reports*, 7(2):45–71.

Bockheim, J. G. (2007). Importance of cryoturbation in redistributing organic carbon in Permafrost-Affected soils. *Soil Science Society of America Journal*, 71(4):1335–1342.

Bonan, G. B. (2008). Forests and climate change: forcings, feedbacks, and the climate benefits of forests. *Science*, 320(5882):1444–1449.

Bonan, G. B., Lombardozzi, D. L., Wieder, W. R., Oleson, K. W., Lawrence, D. M., Hoffman, F. M., and Collier, N. (2019). Model structure and climate data uncertainty in historical simulations of the terrestrial carbon cycle (1850–2014). *Global Biogeochem. Cycles*, 33(10):1310–1326.

Bossio, D. A., Cook-Patton, S. C., Ellis, P. W., Fargione, J., Sanderman, J., Smith, P., Wood, S., Zomer, R. J., von Unger, M., Emmer, I. M., and Griscom, B. W. (2020). The role of soil carbon in natural climate solutions. *Nature Sustainability*, 3(5):391–398.

Box, E. O. (1996). Plant functional types and climate at the global scale. *J. Veg. Sci.*, 7(3):309–320.

Büchner, S. L. A. (2021). ISIMIP3b bias-adjusted atmospheric climate input data.

Canadell, J. G., Monteiro, P. M. S., Costa, M. H., Cotrim da Cunha, L., Cox, P. M., Eliseev, A. V., Henson, S., Ishii, M., Jaccard, S., Koven, C., Lohila, A., Patra, P. K., Piao, S., Rogelj, J., Syampungani, S., Zaehle, S., and Zickfeld, K. (2021). Global carbon and other biogeochemical cycles and feedbacks. In Masson-Delmotte, V., Zhai, P., Pirani, A., Connors, S. L., Péan, C., Berger, S., Caud, N., Chen, Y., Goldfarb, L., Gomis, M. I., Huang, M., Leitzell, K., Lonnoy, E., Matthews, J. B. R., Maycock, T. K., Waterfield, T., Yelekçi, O., Yu, R., and Zhou, B., editors, *Climate Change 2021: The Physical Science Basis. Contribution of Working Group I to the Sixth Assessment Report of the Intergovernmental Panel on Climate Change*, pages 673–816. Cambridge University Press, Cambridge, United Kingdom and New York, NY, USA.

Chini, L., Hurtt, G., Sahajpal, R., Frolking, S., Klein Goldewijk, K., Sitch, S., Ganzenmüller, R., Ma, L., Ott, L., Pongratz, J., and Poulter, B. (2021). Land-use harmonization datasets for annual global carbon budgets. *Earth Syst. Sci. Data*, 13(8):4175–4189.

Chiti, T., Certini, G., Grieco, E., and Valentini, R. (2010). The role of soil in storing carbon in tropical rainforests: the case of ankasa park, ghana. *Plant Soil*, 331(1):453–461.

Crank, J. and Nicolson, P. (1947). A practical method for numerical evaluation of solutions of partial differential equations of the heat-conduction type. *Math. Proc. Cambridge Philos. Soc.*, 43(1):50–67.

Crowther, T. W., Todd-Brown, K. E. O., Rowe, C. W., Wieder, W. R., Carey, J. C., Machmuller, M. B., Snoek, B. L., Fang, S., Zhou, G., Allison, S. D., Blair, J. M., Bridgham, S. D., Burton, A. J., Carrillo, Y., Reich, P. B., Clark, J. S., Classen, A. T., Dijkstra, F. A., Elberling, B., Emmett, B. A., Estiarte, M., Frey, S. D., Guo, J., Harte, J., Jiang, L., Johnson, B. R., Kröel-Dulay, G., Larsen, K. S., Laudon, H., Lavallee, J. M., Luo, Y., Lupascu, M., Ma, L. N., Marhan, S., Michelsen, A., Mohan, J., Niu, S., Pendall, E., Peñuelas, J., Pfeifer-Meister, L., Poll, C., Reinsch, S., Reynolds, L. L., Schmidt, I. K., Sistla, S., Sokol, N. W., Templer, P. H., Treseder, K. K., Welker, J. M., and Bradford, M. A. (2016). Quantifying global soil carbon losses in response to warming. *Nature*, 540(7631):104–108.

Crutzen, P. J. (2016). Geology of mankind. In Crutzen, P. J. and Brauch, H. G., editors, *Paul J. Crutzen: A Pioneer on Atmospheric Chemistry and Climate Change in the Anthropocene*, pages 211–215. Springer International Publishing, Cham.

Da, A., Deluca, C., Balaji, V., Hill, C., and Zaslavsky, L. (2002). The earth system modeling framework.

Elias, S. A., Mock, C. J., and Murton, J. (2013). Yedoma: Late pleistocene ice-rich syngenetic permafrost of beringia. In Elias, S. A., Mock, C. J., and Murton, J., editors, *Encyclopedia of Quaternary Science. 2nd edition*, page 11. Elsevier, Amsterdam.

Eyring, V., Bony, S., Meehl, G. A., Senior, C. A., Stevens, B., Stouffer, R. J., and Taylor, K. E. (2016). Overview of the coupled model intercomparison project phase 6 (CMIP6) experimental design and organization. *Geosci. Model Dev.*, 9(5):1937–1958.

Feng, W., Shi, Z., Jiang, J., Xia, J., Liang, J., Zhou, J., and Luo, Y. (2016). Methodological uncertainty in estimating carbon turnover times of soil fractions. *Soil Biol. Biochem.*, 100:118–124.

Fisher, R. A. and Koven, C. D. (2020). Perspectives on the future of land surface models and the challenges of representing complex terrestrial systems. *J. Adv. Model. Earth Syst.*, 12(4).

Flato, G. M. (2011). Earth system models: an overview. *WIREs Clim Change*, 2(6):783–800.

Friedlingstein, P., Jones, M. W., O'Sullivan, M., Andrew, R. M., Bakker, D. C. E., Hauck, J., Le Quéré, C., Peters, G. P., Peters, W., Pongratz, J., and Others (2022). Global carbon budget 2021. *Earth System Science Data*, 14(4):1917–2005.

Fry, E. L., De Long, J. R., and Bardgett, R. D. (2018). Chapter 2 - plant communities as modulators of soil carbon storage. In Singh, B. K., editor, *Soil Carbon Storage*, pages 29–71. Academic Press.

Gabet, E. J., Reichman, O. J., and Seabloom, E. W. (2003). THE EFFECTS OF BIOTURBATION ON SOIL PROCESSES AND SEDIMENT TRANSPORT. *Annu. Rev. Earth Planet. Sci.*, 31(1):249–273.

García-Palacios, P., Crowther, T. W., Dacal, M., Hartley, I. P., Reinsch, S., Rinnan, R., Rousk, J., van den Hoogen, J., Ye, J.-S., and Bradford, M. A. (2021). Evidence for large microbial-mediated losses of soil carbon under anthropogenic warming. *Nature Reviews Earth & Environment*, 2(7):507–517.

Gruber, S. (2012). Derivation and analysis of a high-resolution estimate of global permafrost zonation. *cryosphere*, 6(1):221–233.

Gulev, S. K., Thorne, P. W., Ahn, J., Dentener, F. J., Domingues, C. M., Gerland, S., Gong, D., Kaufman, D. S., Nnamchi, H. C., Quaas, J., Rivera, J. A., Sathyendranath, S., Smith, S. L., Trewin, B., von Schuckmann, K., and Vose, R. S. (2021). Changing state of the climate system. In Masson-Delmotte, V., Zhai, P., Pirani, A., Connors, S. L., Péan, C., Berger, S., Caud, N., Chen, Y., Goldfarb, L., Gomis, M. I., Huang, M., Leitzell, K., Lonnoy, E., Matthews, J. B. R., Maycock, T. K., Waterfield, T., Yelekçi, O., Yu, R., and Zhou, B., editors, *Climate Change 2021: The Physical Science Basis. Contribution of Working Group I to the Sixth Assessment Report of the Intergovernmental Panel on Climate Change*, pages 287–422. Cambridge University Press, Cambridge, United Kingdom and New York, NY, USA.

Guo, L. B. and Gifford, R. M. (2002). Soil carbon stocks and land use change: a meta analysis. *Glob. Chang. Biol.*, 8(4):345–360.

Hamby, D. M. (1994). A review of techniques for parameter sensitivity analysis of environmental models. *Environ. Monit. Assess.*, 32(2):135–154.

Hararuk, O., Xia, J., and Luo, Y. (2014). Evaluation and improvement of a global land model against soil carbon data using a bayesian markov chain monte carlo method: Calibration of a carbon cycle model. *J. Geophys. Res. Biogeosci.*, 119(3):403–417.

He, Y., Trumbore, S. E., Torn, M. S., Harden, J. W., Vaughn, L. J. S., Allison, S. D., and Randerson, J. T. (2016). Radiocarbon constraints imply reduced carbon uptake by soils during the 21st century. *Science*, 353(6306):1419–1424.

Held, I. M. and Soden, B. J. (2000). Water vapor feedback and global warming. *Annu. Rev. Energy Environ.*, 25(1):441–475.

Herman, J. and Usher, W. (2017). SALib: An open-source python library for sensitivity analysis. *J. Open Source Softw.*, 2(9):97.

Hugelius, G., Strauss, J., Zubrzycki, S., Harden, J. W., Schuur, E. A. G., Ping, C.-L., Schirrmeister, L., Grosse, G., Michaelson, G. J., Koven, C. D., O'Donnell, J. A., Elberling, B., Mishra, U., Camill, P., Yu, Z., Palmtag, J., and Kuhry, P. (2014). Estimated stocks of circumpolar permafrost carbon with quantified uncertainty ranges and identified data gaps. *Biogeosciences*, 11(23):6573–6593.

Hugelius, G., Tarnocai, C., Broll, G., Canadell, J. G., Kuhry, P., and Swanson, D. K. (2013). The northern circumpolar soil carbon database: spatially distributed datasets of soil coverage and soil carbon storage in the northern permafrost regions. *Earth Syst. Sci. Data*, 5(1):3–13.

Hurtt, G., Chini, L., Sahajpal, R., Frolking, S., Bodirsky, B. L., Calvin, K., Doelman, J., Fisk, J., Fujimori, S., Goldewijk, K. K., Hasegawa, T., Havlik, P., Heinimann, A., Humpenöder, F., Jungclaus, J., Kaplan, J., Krisztin, T., Lawrence, D., Lawrence, P., Mertz, O., Pongratz, J., Popp, A., Riahi, K., Shevliakova, E., Stehfest, E., Thornton, P., van Vuuren, D., and Zhang, X. (2017a). Harmonization of global land use scenarios (LUH2): SSP126 v2.1f 2015 - 2100.

Hurtt, G., Chini, L., Sahajpal, R., Frolking, S., Bodirsky, B. L., Calvin, K., Doelman, J., Fisk, J., Fujimori, S., Goldewijk, K. K., Hasegawa, T., Havlik, P., Heinimann, A., Humpenöder, F., Jungclaus, J., Kaplan, J., Krisztin, T., Lawrence, D., Lawrence, P., Mertz, O., Pongratz, J., Popp, A., Riahi, K., Shevliakova, E., Stehfest, E., Thornton, P., van Vuuren, D., and Zhang, X. (2017b). Harmonization of global land use scenarios (LUH2): SSP370 v2.1f 2015 - 2100.

Hurtt, G., Chini, L., Sahajpal, R., Frolking, S., Bodirsky, B. L., Calvin, K., Doelman, J., Fisk, J., Fujimori, S., Goldewijk, K. K., Hasegawa, T., Havlik, P., Heinimann, A., Humpenöder, F., Jungclaus, J., Kaplan, J., Krisztin, T., Lawrence, D., Lawrence, P., Mertz, O., Pongratz, J., Popp, A., Riahi, K., Shevliakova, E., Stehfest, E., Thornton, P., van Vuuren, D., and Zhang, X. (2017c). Harmonization of global land use scenarios (LUH2): SSP585 v2.1f 2015 - 2100.

Hutter, F., Hoos, H. H., and Leyton-Brown, K. (2011). Sequential Model-Based optimization for general algorithm configuration. In *Learning and Intelligent Optimization*, pages 507–523. Springer Berlin Heidelberg.

Ito, A., Hajima, T., Lawrence, D. M., Brovkin, V., Delire, C., Guenet, B., Jones, C. D., Malyshev, S., Materia, S., McDermid, S. P., Peano, D., Pongratz, J., Robertson, E., Shevliakova, E., Vuichard, N., Wårlind, D., Wiltshire, A., and Ziehn, T. (2020). Soil carbon sequestration simulated in CMIP6-LUMIP models: implications for climatic mitigation. *Environ. Res. Lett.*, 15(12):124061.

Iwanaga, T., Usher, W., and Herman, J. (2022). Toward SALib 2.0: Advancing the accessibility and interpretability of global sensitivity analyses. *Socio-Environmental Systems Modelling*, 4:18155.

Jaxa-Rozen, M. and Kwakkel, J. (2018). Tree-based ensemble methods for sensitivity analysis of environmental models: A performance comparison with sobol and morris techniques. *Environmental Modelling & Software*, 107:245–266.

Jian, J., Vargas, R., Anderson-Teixeira, K., Stell, E., Herrmann, V., Horn, M., Kholod, N., Manzon, J., Marchesi, R., Paredes, D., and Bond-Lamberty, B. (2020). A restructured and updated global soil respiration database (SRDB-V5).

Jones, B. and O'Neill, B. C. (2016). Spatially explicit global population scenarios consistent with the shared socioeconomic pathways. *Environ. Res. Lett.*, 11(8):084003.

Keenan, T. F. and Williams, C. A. (2018). The terrestrial carbon sink. *Annu. Rev. Environ. Resour.*, 43(1):219–243.

Keronen, P., Rannik, Ü., Reissell, A., Altimir, N., Hiltunen, V., Vesala, T. V., Kulmala, M., Pohja, T., Siivola, E., and Hari, P. (2004). Long-term measurerments of surface fluxes of ozone above a scots pine forest with eddy covariance and flux-gradient techniques : deposition to forest and differencies between the methods. In *Research unit on physics, chemistry and biology of atmospheric composition and climate change*, pages 104–107.

Klein Goldewijk, K., Beusen, A., Doelman, J., and Stehfest, E. (2017). Anthropogenic land use estimates for the holocene – HYDE 3.2. *Earth Syst. Sci. Data*, 9(2):927–953.

Köchy, M., Hiederer, R., and Freibauer, A. (2015). Global distribution of soil organic carbon – part 1: Masses and frequency distributions of SOC stocks for the tropics, permafrost regions, wetlands, and the world. *SOIL*, 1(1):351–365.

Kou-Giesbrecht, S. and Arora, V. K. (2022). Representing the dynamic response of vegetation to nitrogen limitation via biological nitrogen fixation in the CLASSIC land model. *Global Biogeochem. Cycles*, 36(6).

Koven, C., Friedlingstein, P., Ciais, P., Khvorostyanov, D., Krinner, G., and Tarnocai, C. (2009). On the formation of high-latitude soil carbon stocks: Effects of cryoturbation and insulation by organic matter in a land surface model. *Geophys. Res. Lett.*, 36(21).

Koven, C. D., Riley, W. J., Subin, Z. M., Tang, J. Y., Torn, M. S., Collins, W. D., Bonan, G. B., Lawrence, D. M., and Swenson, S. C. (2013). The effect of vertically resolved soil biogeochemistry and alternate soil C and N models on C dynamics of CLM4. *Biogeosciences*, 10(11):7109–7131.

Koven, C. D., Ringeval, B., Friedlingstein, P., Ciais, P., Cadule, P., Khvorostyanov, D., Krinner, G., and Tarnocai, C. (2011). Permafrost carbon-climate feedbacks accelerate global warming. *Proceedings of the National Academy of Sciences*, 108(36):14769–14774.

Kutsch, W. L., Bahn, M., and Heinemeyer, A. (2009). *Soil Carbon Dynamics: An Integrated Methodology*. Cambridge University Press.

Lajtha, K., Bailey, V., Mcfarlane, K., Paustian, K., Bachelet, D., Abramoff, R., Angers, D., Billings, S., Cerkowniak, D., Dialynas, Y., Finzi, A., French, N., Frey, S., Gurwick, P., Harden, J., Johnson, J., Lehmann, J., Liu, S., Mcconkey, B. G., and Wickland, K. (2018).

Chapter 12: Soils. In Second State of the Carbon Cycle Report (SOCCR2): A Sustained Assessment Report.

Lawrence, D. M., Fisher, R. A., Koven, C. D., Oleson, K. W., Swenson, S. C., Bonan, G., Collier, N., Ghimire, B., van Kampenhout, L., Kennedy, D., Kluzek, E., Lawrence, P. J., Li, F., Li, H., Lombardozzi, D., Riley, W. J., Sacks, W. J., Shi, M., Vertenstein, M., Wieder, W. R., Xu, C., Ali, A. A., Badger, A. M., Bisht, G., van den Broeke, M., Brunke, M. A., Burns, S. P., Buzan, J., Clark, M., Craig, A., Dahlin, K., Drewniak, B., Fisher, J. B., Flanner, M., Fox, A. M., Gentine, P., Hoffman, F., Keppel-Aleks, G., Knox, R., Kumar, S., Lenaerts, J., Leung, L. R., Lipscomb, W. H., Lu, Y., Pandey, A., Pelletier, J. D., Perket, J., Randerson, J. T., Ricciuto, D. M., Sanderson, B. M., Slater, A., Subin, Z. M., Tang, J., Thomas, R. Q., Val Martin, M., and Zeng, X. (2019). The community land model version 5: Description of new features, benchmarking, and impact of forcing uncertainty. *J. Adv. Model. Earth Syst.*, 11(12):4245–4287.

Lawrence, D. M., Koven, C. D., Swenson, S. C., Riley, W. J., and Slater, A. G. (2015). Permafrost thaw and resulting soil moisture changes regulate projected high-latitude CO2 and CH4 emissions. *Environ. Res. Lett.*, 10(9):094011.

Li, W., MacBean, N., Ciais, P., Defourny, P., Lamarche, C., Bontemps, S., Houghton, R. A., and Peng, S. (2018). Gross and net land cover changes in the main plant functional types derived from the annual ESA CCI land cover maps (1992–2015). *Earth Syst. Sci. Data*, 10(1):219–234.

MacBean, N., Peylin, P., Chevallier, F., Scholze, M., and Schürmann, G. (2016). Consistent assimilation of multiple data streams in a carbon cycle data assimilation system. *Geosci. Model Dev.*, 9(10):3569–3588.

Mahowald, N. M., Randerson, J. T., Lindsay, K., Munoz, E., Doney, S. C., Lawrence, P., Schlunegger, S., Ward, D. S., Lawrence, D., and Hoffman, F. M. (2017). Interactions between land use change and carbon cycle feedbacks. *Global Biogeochem. Cycles*, 31(1):96–113.

Melton, J. R. and Arora, V. K. (2016). Competition between plant functional types in the canadian terrestrial ecosystem model (CTEM) v. 2.0.

Melton, J. R., Arora, V. K., Wisernig-Cojoc, E., Seiler, C., Fortier, M., Chan, E., and Teckentrup, L. (2020). CLASSIC v1.0: the open-source community successor to the canadian land surface scheme (CLASS) and the canadian terrestrial ecosystem model (CTEM) – part 1: Model framework and site-level performance. *Geoscientific Model Development*, 13:2825–2850.

Melton, J. R., Shrestha, R. K., and Arora, V. K. (2015). The influence of soils on heterotrophic respiration exerts a strong control on net ecosystem productivity in seasonally dry amazonian forests. *Biogeosciences*, 12(4):1151–1168.

Meyer, G., Humphreys, E. R., Melton, J. R., Cannon, A. J., and Lafleur, P. M. (2021). Simulating shrubs and their energy and carbon dioxide fluxes in canada's low arctic with the canadian land surface scheme including biogeochemical cycles (CLASSIC). *Biogeosciences*, 18(11):3263–3283.

Miner, K. R., Turetsky, M. R., Malina, E., Bartsch, A., Tamminen, J., McGuire, A. D., Fix, A., Sweeney, C., Elder, C. D., and Miller, C. E. (2022). Permafrost carbon emissions in a changing arctic. *Nature Reviews Earth & Environment*, 3(1):55–67.

Nachtergaele, F., van Velthuizen, H., Verelst, L., Batjes, N. H., Dijkshoorn, K., van Engelen, V. W. P., Fischer, G., Jones, A., and Montanarela, L. (2010). The harmonized world soil database. In *Proceedings of the 19th World Congress of Soil Science, Soil Solutions for a Changing World, Brisbane, Australia, 1-6 August 2010*, pages 34–37. library.wur.nl.

Novick, K. A., Biederman, J. A., Desai, A. R., Litvak, M. E., Moore, D. J. P., Scott, R. L., and Torn, M. S. (2018). The AmeriFlux network: A coalition of the willing. *Agric. For. Meteorol.*, 249:444–456.

Ogle, S. M., Breidt, F. J., Easter, M., Williams, S., Killian, K., and Paustian, K. (2010). Scale and uncertainty in modeled soil organic carbon stock changes for US croplands using a process-based model. *Glob. Chang. Biol.*, 16(2):810–822.

Oleson, K. W., Lawrence, D. M., Bonan, G. B., Drewniak, B., and Yang, Z.-L. (2013). *Technical description of version 4.5 of the Community Land Model (CLM)*. NCAR.

Padrón, R. S., Gudmundsson, L., Decharme, B., Ducharne, A., Lawrence, D. M., Mao, J., Peano, D., Krinner, G., Kim, H., and Seneviratne, S. I. (2020). Observed changes in dry-season water availability attributed to human-induced climate change. *Nat. Geosci.*, 13(7):477–481.

Pappas, C., Fatichi, S., Leuzinger, S., Wolf, A., and Burlando, P. (2013). Sensitivity analysis of a process-based ecosystem model: Pinpointing parameterization and structural issues. *J. Geophys. Res. Biogeosci.*, 118(2):505–528.

Parton, W. J. (1996). The CENTURY model. In *Evaluation of Soil Organic Matter Models*, pages 283–291. Springer Berlin Heidelberg.

Pastorello, G., Trotta, C., Canfora, E., Chu, H., Christianson, D., Cheah, Y.-W., Poindexter, C., Chen, J., Elbashandy, A., Humphrey, M., Isaac, P., Polidori, D., Reichstein, M., Ribeca, A., van Ingen, C., Vuichard, N., Zhang, L., Amiro, B., Ammann, C., Arain, M. A., Ardö, J., Arkebauer, T., Arndt, S. K., Arriga, N., Aubinet, M., Aurela, M., Baldocchi, D., Barr, A., Beamesderfer, E., Marchesini, L. B., Bergeron, O., Beringer, J., Bernhofer, C., Berveiller, D., Billesbach, D., Black, T. A., Blanken, P. D., Bohrer, G., Boike, J., Bolstad, P. V., Bonal, D., Bonnefond, J.-M., Bowling, D. R., Bracho, R., Brodeur, J., Brümmer, C., Buchmann, N., Burban, B., Burns, S. P., Buysse, P., Cale, P., Cavagna, M., Cellier, P., Chen, S., Chini, I., Christensen, T. R., Cleverly, J., Collalti, A., Consalvo, C., Cook, B. D., Cook, D., Coursolle, C., Cremonese, E., Curtis, P. S., D'Andrea, E., da Rocha, H., Dai, X., Davis, K. J., De Cinti, B., de Grandcourt, A., De Ligne, A., De Oliveira, R. C., Delpierre, N., Desai, A. R., Di Bella, C. M., di Tommasi, P., Dolman, H., Domingo, F., Dong, G., Dore, S., Duce, P., Dufrêne, E., Dunn, A., Dušek, J., Eamus, D., Eichelmann, U., ElKhidir, H. A. M., Eugster, W., Ewenz, C. M., Ewers, B., Famulari, D., Fares, S., Feigenwinter, I., Feitz, A., Fensholt, R., Filippa, G., Fischer, M., Frank, J., Galvagno, M., Gharun, M., Gianelle, D., Gielen, B., Gioli, B., Gitelson, A., Goded, I., Goeckede, M., Goldstein, A. H., Gough, C. M., Goulden, M. L., Graf, A., Griebel, A., Gruening, C., Grünwald, T., Hammerle, A., Han, S., Han, X., Hansen, B. U., Hanson, C., Hatakka, J., He, Y., Hehn, M., Heinesch, B., Hinko-Najera, N., Hörtnagl, L., Hutley, L., Ibrom, A., Ikawa, H., Jackowicz-Korczynski, M., Janouš, D., Jans, W., Jassal, R., Jiang, S., Kato, T., Khomik, M., Klatt, J., Knohl, A., Knox, S., Kobayashi, H., Koerber, G., Kolle, O., Kosugi, Y., Kotani, A., Kowalski, A., Kruijt, B., Kurbatova, J., Kutsch, W. L., Kwon, H., Launiainen, S., Laurila, T., Law, B., Leuning, R., Li, Y., Liddell, M., Limousin, J.-M., Lion, M., Liska, A. J., Lohila, A., López-Ballesteros, A., López-Blanco, E., Loubet, B., Loustau, D., Lucas-Moffat, A., Lüers, J., Ma, S., Macfarlane, C., Magliulo, V., Maier, R., Mammarella, I., Manca, G., Marcolla, B., Margolis, H. A., Marras, S., Massman, W., Mastepanov, M., Matamala, R., Matthes, J. H., Mazzenga, F., McCaughey, H., McHugh, I., McMillan, A. M. S., Merbold, L., Meyer, W., Meyers, T., Miller, S. D., Minerbi, S., Moderow, U., Monson, R. K., Montagnani, L., Moore, C. E., Moors, E., Moreaux, V., Moureaux, C., Munger, J. W., Nakai, T., Neirynck, J., Nesic, Z., Nicolini, G., Noormets, A., Northwood, M., Nosetto, M., Nouvellon, Y., Novick, K., Oechel, W., Olesen, J. E., Ourcival, J.-M., Papuga, S. A., Parmentier, F.-J., Paul-Limoges, E., Pavelka, M., Peichl, M., Pendall, E., Phillips, R. P., Pilegaard, K., Pirk, N., Posse, G., Powell, T., Prasse, H., Prober, S. M., Rambal, S., Rannik, Ü., Raz-Yaseef, N., Rebmann, C., Reed, D., de Dios, V. R., Restrepo-Coupe, N., Reverter, B. R., Roland, M., Sabbatini, S., Sachs, T., Saleska, S. R., Sánchez-Cañete, E. P., Sanchez-Mejia, Z. M., Schmid, H. P., Schmidt, M., Schneider, K., Schrader, F., Schroder, I., Scott, R. L., Sedlák, P., Serrano-Ortíz, P., Shao, C., Shi, P., Shironya, I., Siebicke, L., Šigut, L., Silberstein, R., Sirca, C., Spano, D., Steinbrecher, R., Stevens, R. M., Sturtevant, C., Suyker, A., Tagesson, T., Takanashi, S., Tang, Y., Tapper, N., Thom, J., Tomassucci, M., Tuovinen, J.-P., Urbanski, S., Valentini, R., van der Molen, M., van Gorsel, E., van Huissteden, K., Varlagin, A., Verfaillie, J., Vesala, T., Vincke, C., Vitale, D., Vygodskaya, N., Walker, J. P., Walter-Shea, E., Wang, H., Weber, R., Westermann, S., Wille, C., Wofsy, S., Wohlfahrt, G., Wolf, S., Woodgate, W., Li, Y., Zampedri, R., Zhang, J., Zhou, G., Zona, D., Agarwal, D., Biraud, S., Torn, M., and Papale, D. (2021). Author correction: The FLUXNET2015 dataset and the ONEFlux processing pipeline for eddy covariance data. *Sci Data*, 8(1):72.

Poggio, L., de Sousa, L. M., Batjes, N. H., Heuvelink, G. B. M., Kempen, B., Ribeiro, E., and Rossiter, D. (2021). SoilGrids 2.0: producing soil information for the globe with quantified spatial uncertainty. *SOIL*, 7(1):217–240.

Rantanen, M., Karpechko, A. Y., Lipponen, A., Nordling, K., Hyvärinen, O., Ruosteenoja, K., Vihma, T., and Laaksonen, A. (2022). The arctic has warmed nearly four times faster than the globe since 1979. *Communications Earth & Environment*, 3(1):1–10.

Raupach, M. R. and Canadell, J. G. (2010). Carbon and the anthropocene. *Current Opinion in Environmental Sustainability*, 2(4):210–218.

Reyer, M. B. A. (2022). ISIMIP3b atmospheric composition input data.

Ricciuto, D. M., Xu, X., Shi, X., Wang, Y., Song, X., Schadt, C. W., Griffiths, N. A., Mao, J., Warren, J. M., Thornton, P. E., Chanton, J., Keller, J. K., Bridgham, S. D., Gutknecht, J., Sebestyen, S. D., Finzi, A., Kolka, R., and Hanson, P. J. (2021). An integrative model for soil biogeochemistry and methane processes: I. model structure and sensitivity analysis. *J. Geophys. Res. Biogeosci.*, 126(8).

Saltelli, A. (2002). Making best use of model evaluations to compute sensitivity indices. *Comput. Phys. Commun.*, 145(2):280–297.

Saltelli, A., Ratto, M., Andres, T., Campolongo, F., Cariboni, J., Gatelli, D., Saisana, M., and Tarantola, S. (2008). *Global Sensitivity Analysis: The Primer*. John Wiley & Sons.

Scharlemann, J. P. W., Tanner, E. V. J., Hiederer, R., and Kapos, V. (2014). Global soil carbon: understanding and managing the largest terrestrial carbon pool. *Carbon Management*, 5(1):81–91.

Schuur, E. A. G., Abbott, B. W., Commane, R., Ernakovich, J., Euskirchen, E., Hugelius, G., Grosse, G., Jones, M., Koven, C., Leshyk, V., Lawrence, D., Loranty, M. M., Mauritz, M., Olefeldt, D., Natali, S., Rodenhizer, H., Salmon, V., Schädel, C., Strauss, J., Treat, C., and Turetsky, M. (2022). Permafrost and climate change: Carbon cycle feedbacks from the warming arctic. *Annu. Rev. Environ. Resour.*, 47(1):343–371.

Schuur, E. A. G., McGuire, A. D., Schädel, C., Grosse, G., Harden, J. W., Hayes, D. J., Hugelius, G., Koven, C. D., Kuhry, P., Lawrence, D. M., Natali, S. M., Olefeldt, D., Romanovsky, V. E., Schaefer, K., Turetsky, M. R., Treat, C. C., and Vonk, J. E. (2015). Climate change and the permafrost carbon feedback. *Nature*, 520(7546):171–179.

Schuur, T., McGuire, A. D., Romanovsky, V. E., Schadel, C., and Mack, M. (2018). Arctic and boreal carbon. In *Review of the draft second state of the carbon cycle report (SOCCR2)*. The National Academies Press, Washington, D.C.

Seiler, Melton, Arora, and others (2021). ... community successor to the canadian land surface scheme (CLASS) and the canadian terrestrial ecosystem model (CTEM)–Part 2: Global benchmarking. *Geosci. Model Dev.*

Sellers, P. J., Mintz, Y., Sud, Y. C., and Dalcher, A. (1986). A simple biosphere model (SIB) for use within general circulation models. *J. Atmos. Sci.*, 43(6):505–531.

Sellers, P. J., Schimel, D. S., Moore, 3rd, B., Liu, J., and Eldering, A. (2018). Observing carbon cycle-climate feedbacks from space. *Proc. Natl. Acad. Sci. U. S. A.*, 115(31):7860–7868.

Shahriari, B., Swersky, K., Wang, Z., Adams, R. P., and de Freitas, N. (2016). Taking the human out of the loop: A review of bayesian optimization.

Shan, S. and Wang, G. G. (2010). Survey of modeling and optimization strategies to solve high-dimensional design problems with computationally-expensive black-box functions. *Struct. Multidiscip. Optim.*, 41(2):219–241.

Shangguan, W., Dai, Y., Duan, Q., Liu, B., and Yuan, H. (2014). A global soil data set for earth system modeling. *Journal of Advances in Modeling Earth Systems*, 6(1):249–263.

Shi, Z., Crowell, S., Luo, Y., and Moore, 3rd, B. (2018). Model structures amplify uncertainty in predicted soil carbon responses to climate change. *Nat. Commun.*, 9(1):2171.

Shukla, P. R., Skea, J., Calvo Buendia, E., Masson-Delmotte, V., Pörtner, H. O., Roberts, D. C., Zhai, P., Slade, R., Connors, S., Van Diemen, R., and Others (2019). IPCC, 2019: Climate change and land: an IPCC special report on climate change, desertification, land degradation, sustainable land management, food security, and greenhouse gas fluxes in terrestrial ecosystems.

Singh, N., Abiven, S., Maestrini, B., Bird, J. A., Torn, M. S., and Schmidt, M. W. I. (2014). Transformation and stabilization of pyrogenic organic matter in a temperate forest field experiment. *Glob. Chang. Biol.*, 20(5):1629–1642.

Sobol', I. M. (2001). Global sensitivity indices for nonlinear mathematical models and their monte carlo estimates. *Math. Comput. Simul.*, 55(1):271–280.

Sonnentag, O. and Marsh, P. (2021). AmeriFlux AmeriFlux CA-TVC trail valley creek.

Steffen, W., Rockström, J., Richardson, K., Lenton, T. M., Folke, C., Liverman, D., Summerhayes, C. P., Barnosky, A. D., Cornell, S. E., Crucifix, M., Donges, J. F., Fetzer, I., Lade, S. J., Scheffer, M., Winkelmann, R., and Schellnhuber, H. J. (2018). Trajectories of the earth system in the anthropocene. *Proc. Natl. Acad. Sci. U. S. A.*, 115(33):8252–8259.

Stockmann, U., Padarian, J., McBratney, A., Minasny, B., de Brogniez, D., Montanarella, L., Hong, S. Y., Rawlins, B. G., and Field, D. J. (2015). Global soil organic carbon assessment. *Global Food Security*, 6:9–16.

Strauss, J., Laboor, S., Schirrmeister, L., Fedorov, A. N., Fortier, D., Froese, D., Fuchs, M., Günther, F., Grigoriev, M., Harden, J., Hugelius, G., Jongejans, L. L., Kanevskiy, M., Kholodov, A., Kunitsky, V., Kraev, G., Lozhkin, A., Rivkina, E., Shur, Y., Siegert, C., Spektor, V., Streletskaya, I., Ulrich, M., Vartanyan, S., Veremeeva, A., Anthony, K. W., Wetterich, S., Zimov, N., and Grosse, G. (2021). Circum-Arctic map of the yedoma permafrost domain. *Front Earth Sci. Chin.*, 9.

Strauss, J., Schirrmeister, L., Grosse, G., Wetterich, S., Ulrich, M., Herzschuh, U., and Hubberten, H.-W. (2013). The deep permafrost carbon pool of the yedoma region in siberia and alaska. *Geophys. Res. Lett.*, 40(23):6165–6170.

Sun, G. and Mu, M. (2022). Role of hydrological parameters in the uncertainty in modeled soil organic carbon using a coupled water-carbon cycle model. *Ecol. Complex.*, 50:100986.

Swart, N. C., Cole, J., Kharin, S., Lazare, M., Scinocca, J., Gillett, N., Anstey, J., Arora, V., Christian, J., Hanna, S., Jiao, Y., Lee, W., Majaess, F., Saenko, O., Seiler, C., Seinen, C., Shao, A., Solheim, L., von Salzen, K., Yang, D., and Winter, B. (2019). The canadian earth system model (canesm) - v5.0.3.

Tang, J. and Zhuang, Q. (2008). Equifinality in parameterization of process-based biogeochemistry models: A significant uncertainty source to the estimation of regional carbon dynamics. *J. Geophys. Res.*, 113(G4).

Tang, X., Pei, X., Lei, N., Luo, X., Liu, L., Shi, L., Chen, G., and Liang, J. (2020). Global patterns of soil autotrophic respiration and its relation to climate, soil and vegetation characteristics. *Geoderma*, 369:114339.

Tao, F., Zhou, Z., Huang, Y., Li, Q., Lu, X., Ma, S., Huang, X., Liang, Y., Hugelius, G., Jiang, L., Doughty, R., Ren, Z., and Luo, Y. (2020). Deep learning optimizes Data-Driven representation of soil organic carbon in earth system model over the conterminous united states. *Front Big Data*, 3:17.

Taylor, K. E., Stouffer, R. J., and Meehl, G. A. (2012). An overview of CMIP5 and the experiment design. *Bull. Am. Meteorol. Soc.*, 93(4):485–498.

Tian, H., Lu, C., Yang, J., Banger, K., Huntzinger, D. N., Schwalm, C. R., Michalak, A. M., Cook, R., Ciais, P., Hayes, D., Huang, M., Ito, A., Jain, A. K., Lei, H., Mao, J., Pan, S., Post, W. M., Peng, S., Poulter, B., Ren, W., Ricciuto, D., Schaefer, K., Shi, X., Tao, B., Wang, W., Wei, Y., Yang, Q., Zhang, B., and Zeng, N. (2015). Global patterns and controls of soil organic carbon dynamics as simulated by multiple terrestrial biosphere models: Current status and future directions. *Global Biogeochem. Cycles*, 29(6):775–792.

Tifafi, M., Guenet, B., and Hatté, C. (2018). Large differences in global and regional total soil carbon stock estimates based on SoilGrids, HWSD, and NCSCD: Intercomparison and evaluation based on field data from USA, england, wales, and france. *Global Biogeochem. Cycles*, 32(1):42–56.

Todd-Brown, K. E. O., Randerson, J. T., Post, W. M., Hoffman, F. M., Tarnocai, C., Schuur, E. A. G., and Allison, S. D. (2013). Causes of variation in soil carbon simulations from CMIP5 earth system models and comparison with observations. *Biogeosciences*, 10(3):1717–1736.

Van Everdingen, R. O., Association, I. P., and Others (1998). *Multi-language glossary of permafrost and related ground-ice terms in chinese, english, french, german*. Arctic Inst. of North America University of Calgary.

Vandenberghe, J. (2013). Cryoturbation structures. *Encyclopedia of Quaternary Science*, 3:430–435.

Varney, R. M., Chadburn, S. E., Burke, E. J., and Cox, P. M. (2022). Evaluation of soil carbon simulation in CMIP6 earth system models. *Biogeosci. Discuss.*, pages 1–52.

Verseghy, D. (2017). CLASS–The canadian land surface scheme (v. 3.6. 2). *Climate Research Division, Science and Technology Branch, Environment Canada*, 35.

Wang, M., Guo, X., Zhang, S., Xiao, L., Mishra, U., Yang, Y., Zhu, B., Wang, G., Mao, X., Qian, T., Jiang, T., Shi, Z., and Luo, Z. (2022). Global soil profiles indicate depth-dependent soil carbon losses under a warmer climate. *Nat. Commun.*, 13(1):1–11.

Wang, S., Zhang, Y., Ju, W., Chen, J. M., Ciais, P., Cescatti, A., Sardans, J., Janssens, I. A., Wu, M., Berry, J. A., Campbell, E., Fernández-Martínez, M., Alkama, R., Sitch, S., Friedlingstein, P., Smith, W. K., Yuan, W., He, W., Lombardozzi, D., Kautz, M., Zhu, D., Lienert, S., Kato, E., Poulter, B., Sanders, T. G. M., Krüger, I., Wang, R., Zeng, N., Tian, H., Vuichard, N., Jain, A. K., Wiltshire, A., Haverd, V., Goll, D. S., and Peñuelas, J. (2020). Recent global decline of CO_2 fertilization effects on vegetation photosynthesis. *Science*, 370(6522):1295–1300.

Waters, C. N., Zalasiewicz, J., Summerhayes, C., Barnosky, A. D., Poirier, C., Gałuszka, A., Cearreta, A., Edgeworth, M., Ellis, E. C., Ellis, M., Jeandel, C., Leinfelder, R., McNeill, J. R., Richter, D. D., Steffen, W., Syvitski, J., Vidas, D., Wagreich, M., Williams, M., Zhisheng, A., Grinevald, J., Odada, E., Oreskes, N., and Wolfe, A. P. (2016). The anthropocene is functionally and stratigraphically distinct from the holocene. *Science*, 351(6269):aad2622.

Watts, J. D., Natali, S., Potter, S., and Rogers, B. M. (2019). Gridded winter soil CO2 flux estimates for pan-arctic and boreal regions, 2003-2100.

Wieder, W. R., Grandy, A. S., Kallenbach, C. M., Taylor, P. G., and Bonan, G. B. (2015). Representing life in the earth system with soil microbial functional traits in the MIMICS model. *Geosci. Model Dev.*, 8(6):1789–1808.

Williams, M., Richardson, A. D., Reichstein, M., Stoy, P. C., Peylin, P., Verbeeck, H., Carvalhais, N., Jung, M., Hollinger, D. Y., Kattge, J., Leuning, R., Luo, Y., Tomelleri, E., Trudinger, C. M., and Wang, Y.-P. (2009). Improving land surface models with FLUXNET data. *Biogeosciences*, 6(7):1341–1359.

Wu, Z., Ahlström, A., Smith, B., Ardö, J., Eklundh, L., Fensholt, R., and Lehsten, V. (2017). Climate data induced uncertainty in model-based estimations of terrestrial primary productivity. *Environ. Res. Lett.*, 12(6):064013.

Wullschleger, S. D., Epstein, H. E., Box, E. O., Euskirchen, E. S., Goswami, S., Iversen, C. M., Kattge, J., Norby, R. J., van Bodegom, P. M., and Xu, X. (2014). Plant functional types in earth system models: past experiences and future directions for application of dynamic vegetation models in high-latitude ecosystems. *Ann. Bot.*, 114(1):1–16.